

Thomas Kösters

Derivation and Analysis of Scatter Correction Algorithms  
for Quantitative Positron Emission Tomography

2010







**Mathematik**

**Derivation and Analysis of Scatter Correction Algorithms  
for Quantitative Positron Emission Tomography**

Inaugural-Dissertation  
zur Erlangung des Doktorgrades  
der Naturwissenschaften im Fachbereich  
Mathematik und Informatik  
der Mathematisch-Naturwissenschaftlichen Fakultät  
der Westfälischen Wilhelms-Universität Münster

vorgelegt von  
Thomas Kösters  
aus Steinfurt  
- 2010 -

Dekan:	Herr Prof. Dr. Christopher Deninger
Erster Gutachter:	Herr Prof. Dr. Dr. h.c. Frank Natterer
Zweiter Gutachter:	Herr Prof. Dr. Martin Burger
Tag der mündlichen Prüfung:	20.07.2010
Tag der Promotion:	20.07.2010

# Dedication

To my parents

# Acknowledgments

I am grateful to my supervisors, Prof. F. Natterer and Prof. M. Burger, whose encouragement, guidance and support enabled me to write this thesis. I would like to show my gratitude to Dr. F. Wübbeling and Dr. K. Schäfers for assistance and fruitful discussion. An honorable mention goes to J.F. Pietschmann, F. Gigengack, M. Fieseler and F. Büther for proof-reading this manuscript and proposals for improvements. Finally, I am indebted to many of my colleagues at the European Institute for Molecular Imaging (spokesman: Prof. M. Schäfers), the SFB 656 (spokesman: Prof. O. Schober) and the Institute for Computational and Applied Mathematics at the University of Münster for supporting me.

# Contents

<b>Abstract</b>	<b>11</b>
<b>Outline</b>	<b>14</b>
<b>1 Introduction</b>	<b>15</b>
1.1 Computed Tomography . . . . .	15
1.2 Single Photon Emission Computerized Tomography . . . . .	16
1.3 Positron Emission Tomography . . . . .	18
<b>2 The Scatter Model for PET Based on the Boltzmann Equation</b>	<b>31</b>
2.1 The Stationary Boltzmann Equation . . . . .	32
2.2 The Scatter Model . . . . .	35
<b>3 A Neumann Series Approach for Scatter Correction in PET</b>	<b>53</b>
3.1 Introducing the Neumann Series . . . . .	54
3.2 A Suitable Function Space . . . . .	61
3.3 The Single Scatter Approximation . . . . .	65
3.4 Multiple Scatter . . . . .	72
<b>4 Numerical Results</b>	<b>75</b>
4.1 PET in the case of weakly scattering media . . . . .	75
4.2 Scatter Correction in PET using Projection Volumes . . . . .	85
<b>5 Conclusion and Outlook</b>	<b>93</b>
<b>Bibliography</b>	<b>100</b>



# Abstract

Positron Emission Tomography (PET) plays an important role in medical imaging. In contrast to techniques like Computerized Tomography (CT) providing information about the anatomy of the patients body, PET can be used to study the metabolism of the patient. Often both, functional and morphological, devices are combined in a single system in order to benefit from both techniques.

Although PET is already used in daily routine, improvements in the underlying mathematical model are still possible. In general, the X-ray transform is used the analytical model for PET. The main drawback of this model in connection with PET is the fact that it is only suitable for particles that travel along straight rays. Scattered particles, which are a major problem in quantitative PET, are not considered by this model.

In order to use the straight line model the scatter fraction is usually estimated based on physical considerations and subtracted from the measured data. After this correction the X-ray transform can be assumed as the correct model for PET. Obviously, this data correction leads to reduced statistics and strictly speaking the model is still somehow wrong for PET.

In this work a new model is presented that includes, in addition to the particles travelling along straight rays, all possible measurements resulting from scattered events. It is shown in particular that this mathematical model, which is based on the Boltzmann equation, fits exactly to the physical processes behind PET. A detailed analysis using a Neumann series approach leading to Sobolev space estimates is performed in order to show that the new model can be seen as a perturbation of the X-ray transform. Additionally, this approach allows to recover the unknown activity distribution using the inversion formulas for the X-ray transform.

The scatter estimate of the new model can be used as input for standard scatter correction methods. Next the the classical approaches it is possible to modify existing reconstruction algorithms by projecting along volumes resulting from the scatter distribution. This reconstruction technique contains a precise but time-consuming preprocessing step where all projection volumes for all possible lines of responses are precalculated. An evaluation of this approach on simulated 2D data proofed its superiority in case of low statistics.



# Outline

In the first chapter the basic principles of Computerized Tomography (CT), Single Photon Emission Computerized Tomography (SPECT) and of course Positron Emission Tomography (PET) are introduced. Further, the mathematical relation between those three techniques is presented. Additionally, several problems inherent in quantitative PET like attenuation of photons or random and scattered coincidences are discussed in detail. For each problem the corresponding correction strategies are reviewed. The main focus is put on the different scatter correction techniques. At this point the physical relation between PET and CT arises. It will become obvious to the reader that scatter is one of the major problems in quantitative PET and in addition one of the hardest problems to correct for. In the second chapter a new analytical model for describing the process of PET data acquisition based on the stationary Boltzmann equation is presented. Contrary to the X-ray transform, which is the current analytical PET model, it includes scattered coincidences and energy dependency of photons. It is shown that the new model exactly characterizes the physical properties of PET whereas the X-ray transform requires a scatter-free dataset as input. The special cases of single scatter and no scatter are analyzed in detail. In general the amount of scatter in the measured data can be controlled by a threshold that defines the energy window of the system. In this context it will become apparent that the new model is closely related to the X-ray transform.

Chapter three deals with the inverse problem for the new PET model in order to derive the unknown activity distribution. Obviously the inversion formula for the X-ray transform cannot directly be applied to the new model without a detailed analysis of the impact of scattered photons. Therefore the new model is treated as a perturbation of the X-ray transform. This approach leads to a Neumann series whose convergence is proofed under a simple restriction on the attenuation map in combination with the energy window.

In the fourth chapter numerical experiments are discussed. Firstly, reconstructions of Monte Carlo simulated mouse PET data are studied. The impact of scatter and attenuation is analyzed as a function of object size, i.e. the mouse used as input for the simulation is systematically increased. Secondly the direct implementation of the new PET model is studied. The corresponding reconstruction algorithm using projections along volumes is compared to standard reconstructions using the straight line model.

The last chapter contains the conclusions and an outlook for possible future research.



# Chapter 1

## Introduction

Medical imaging covers a broad range of techniques used to create images of the patients body. Since this work is mainly focused on Positron Emission Tomography (PET) we will only present three different techniques that are related by using similar integral transforms. We give a short introduction to Computed Tomography (CT) and Single Photon Emission Computerized Tomography (SPECT) followed by a detailed presentation of PET.

### 1.1 Computed Tomography

*Computed Tomography* (CT) is a medical imaging method used to visualize the body's anatomical structures by sending X-rays through the patient. Since X-rays are attenuated while passing matter the measured energy on the other side of the body is lower than the incident energy. Hence in case of a linear attenuation coefficient the change of the incident X-ray intensity  $I_0$  along the straight line  $L$  to the measured intensity  $I_1$  can be described as

$$\log \left( \frac{I_0}{I_1} \right) = \int_L f(x) dx, \quad (1.1)$$

where we denote  $f$  as the linear attenuation coefficient of the patient's body (see figure 1.1). The challenge now is to compute the attenuation coefficient  $f$  from (1.1) known for several lines  $L$ . Therefore the X-ray source rotates around the patient to collect data from all directions. In order to speed up the measuring process the X-ray tube emits a fan-shaped beam or even a cone beam of X-rays. Depending on the scanner, the source may not only move circular but in axial directions, too. Thus the data is collected along a helical or similar - like the circle and line - source trajectory. For a detailed study of the different trajectories we refer to Katsevich [Kat02, Kat04]. If we rewrite equation (1.1) using the notation  $x \cdot \Theta = s$  with  $\Theta \in S^1$  and  $s \in \mathbb{R}^1$  as

$$Rf(\Theta, s) = \int_{x \cdot \Theta = s} f(x) dx, \quad (1.2)$$

the operator  $R$  is called the Radon transform. In order to derive  $f$  out of the measurements  $g$  we have to invert the  $R$ . A solution to this problem was given in 1917 by the austrian



Figure 1.1: The attenuation of the incident intensity  $I_0$  along the path  $\overline{AB}$  must be equal to the attenuation along  $\overline{AC}$  followed by the attenuation along  $\overline{CB}$ , i.e.  $I_1 = I_0 \cdot E(\overline{AB}) = I_0 \cdot E(\overline{AC} + \overline{CB}) = I_0 \cdot E(\overline{AC}) \cdot E(\overline{CB})$  if we denote  $E$  as the function describing the change of intensity from  $I_0$  to  $I_1$  along a given path. Only the exponential function satisfies this requirement. Thus the changing of the incident beam intensity  $I_0$  to  $I_1$  measured at  $B$  can be expressed by (1.1).

mathematician Radon [Rad17]. His inversion formula for  $R$  reads

$$f(x) = \frac{1}{4\pi^2} \int_{\mathbb{S}^1} \int_{\mathbb{R}^1} \frac{d}{ds} g(\Theta, s) \frac{ds}{x \cdot \Theta - s} d\Theta. \tag{1.3}$$

In real applications usually the filtered backprojection algorithm [PSV09] is used to derive  $f$  which can be viewed as a numerical implementation of the inversion formula (1.3). Current CT scanner have a resolution up to several  $\mu m$  and allow to analyze very small structures, but since they cannot show metabolism they are not ideal for detecting some tumors.

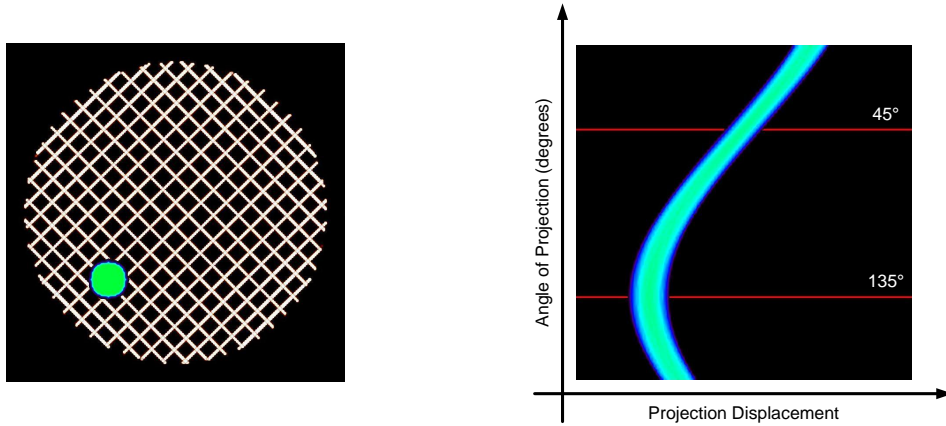
Hence CT is often combined with other devices like SPECT or PET which are able to show metabolism to benefit from advantages of both approaches, i.e. showing the anatomical information with very high resolution fused with an image of the actual metabolism inside the body.

Although we want to work on PET correction techniques we mention that CT is very important for us since we use the measured and derived respectively attenuation coefficient for attenuation and scatter correction in PET. Details will be given in the PET section.

## 1.2 Single Photon Emission Computerized Tomography

Next to CT where photons are send through the patient, there exists another class of imaging techniques called emission tomography that relies on measuring photons that are emitted inside the patient. These "internal sources" are given by molecules which are labelled with a radioactive marker and are injected prior to the measurement. In *Single Photon Emission Computed Tomography* (SPECT) these markers emit gamma photons. Depending on the choice of molecules we can predict where inside the body the radioactive marker must be located. Hence we are interested to reconstruct these internal sources, i.e. the tracer distribution and not the attenuation coefficient as in CT.

Since we cannot control the flying direction of the emitted particles we have to introduce collimators [MDDH86] in front of the detector, see figure 1.3. In combination with photons flying out of the ring the loss of particles is immense. Nevertheless we are now able to



(a) Example of parallel beam geometry: Parallel lines at  $45^\circ$  and  $135^\circ$  are sent through the object, whereas the shape of the object can be seen in the projections as in figure 1.2(b).

(b) The projections displayed in figure 1.2(a) are usually stored in a sinogram. The name sinogram results from the sinusoidal structure in the projections in case of a single object that is placed off-center.

Figure 1.2: Parallel projections of two different angles and the corresponding sinogram.

track photons flying on a straight line and obtain a similar line model as in the case of CT. Photons measured on line  $L$  are proportional to

$$I = \int_L f(x) e^{-\int_{L(x)} \mu(y) dy} dx, \quad (1.4)$$

where  $L(x)$  denotes the half-line of  $L$  with endpoint  $x$ . In contrast to the previous section  $f$  denotes the unknown tracer distribution while the attenuation coefficient which may be measured using a CT scanner is given by  $\mu$ . If no CT scanner is available there are other approaches to deal with the missing information like using approximations for  $\mu$  [WCNG97] or solving (1.4) alternating for  $f$  and  $\mu$  [GN02].

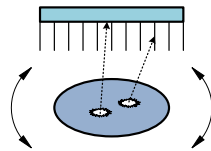


Figure 1.3: The collimated detector rotates around the patient to collect data from all directions. State of the art SPECT scanner use much more complicated collimator techniques as shown in this example [vdHVR<sup>+</sup>09].

Again we introduce the notation  $x \cdot \Theta = s$  with  $\Theta \in S^1$  and  $s \in \mathbb{R}^1$  to define the attenuated Radon transform  $R_\mu$

$$R_\mu f(\Theta, s) = \int_{x \cdot \Theta = s} f(x) e^{-D\mu(x, \Theta^\perp)} dx, \quad (1.5)$$

where  $D\mu$  is given by the cone beam transform

$$D\mu(x, \Theta) = \int_0^{\infty} f(x + t\Theta) dt.$$

Assuming the attenuation map  $\mu$  is given one is interested to have an exact inversion formula for (1.5) as in the case of the classical Radon transform. More than 80 years after Radon presented his inversion formula (1.3), Novikov [Nov00, Nov02] followed by Natterer [Nat00] and Kunyansky [Kun01] presented inversion formulas for (1.5).

### 1.3 Positron Emission Tomography

Analogous to SPECT the emission of radiation is the physical basis of *positron emission tomography* (PET). Here the beta<sup>+</sup> decay is used instead of the gamma decay. Although an electron neutrino  $\nu_e$  and a positron  $e^+$  are emitted during a beta<sup>+</sup> decay we still measure gamma particles: While travelling through tissue the emitted positron is slowed down and finally annihilates with an electron  $e^-$  resulting in two gamma photons  $\gamma$  at 511 keV that are emitted in opposite directions under an angle of 180°:

$$e^+ + e^- \rightarrow 2\gamma.$$

This leads to the main difference compared to SPECT: In PET we need two particles for one measurement. Due to the short transit time of photons crossing the body the two particles can be detected nearly simultaneously by the detectors. If a single photon arrives at a detector, a small time window, the so-called coincidence window of about some milliseconds, is opened. The next photon arriving at a different detector is assumed to originate from the same decay and the two photons are considered as a measurement (see figure 1.7) where the decay should have taken place on the line connecting these two detectors.

In most of the current PET scanners the detectors are arranged in a ring (see figure 4.1(c)) where several rings are stacked to increase both the sensitivity and the field of view (FOV). As an example the Siemens Biograph Sensation 16 used for numerical experiments in chapter 4 has 24 rings each containing 384 detectors leading to 9216 detectors in total. For a detailed description of the detection process, i.e. the conversion of photon energy to an electrical impulse we refer to [WA04].

Analogous to the integral equation (1.3) for SPECT, there is a corresponding equation for PET where we have to consider the two gammas instead of a single one in SPECT. This leads to

$$I = \int_L f(x) \exp\left(-\int_{L_+(x)} \mu(y) dy - \int_{L_-(x)} \mu(y) dy\right) dx, \quad (1.6)$$

where  $L_-(x), L_+(x)$  denote the two half-lines of  $L$  with endpoint  $x$ . The integrals along the half-lines can be merged and we obtain

$$I = \exp\left(-\int_L \mu(y) dy\right) \int_L f(x). \quad (1.7)$$

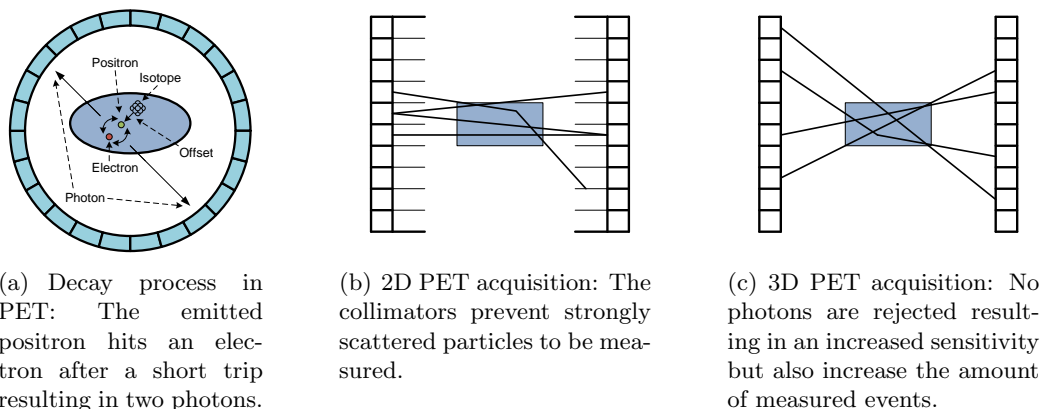


Figure 1.4: The first generation of PET scanners used 2D acquisitions, where only coincidences between different detectors of the same and adjacent rings were allowed. Collimators were used in order to reduce the amount of scattered events in the measurements as can be seen in b). Modern PET scanner allow 3D acquisitions that significantly increase the sensitivity of the system but also increase the amount of measured scattered events [CMH93]. Hence an exact scatter correction plays an important role in 3D PET.

Since (1.7) has the same form as the reconstruction problem described in the CT section we may use the already proposed methods to reconstruct  $f$ . In fact filtered back projection was the gold standard reconstruction algorithm in PET for a long time and is still quite common in clinical applications [Cas08].

Next to the analytical approaches, i.e. inverting the integral equation, there are stochastically based reconstruction algorithms to derive  $f$  from the measurements. For those discrete approaches we subdivide the reconstruction region into pixels (2D) or voxels (3D) and introduce the system matrix  $A = (A_{ij})$  containing the probability that a photon pair emitted in voxel  $j$  is measured on line  $i$ . The corresponding probabilities can be found by complex measurements or by regarding the scanner geometry. We may write for the expected number of events detected at line  $i$

$$\bar{m}_i := \sum_{j=1}^N A_{ij} f_j,$$

where  $f_j$  is the unknown activity represented by a grid of  $N$  voxels. The measurements  $g = (g_i)_{i=1, \dots, K}$  on line  $i$  are assumed to be poisson-distributed since the radioactive decay of atoms is usually modelled by poisson processes. In order to derive  $f$  given the measurements  $g$  the likelihood function

$$L(g|f) = \prod_{i=1}^K \frac{\bar{m}_i^{g_i} \exp(-\bar{m}_i)}{g_i!} \quad (1.8)$$

is introduced. An iterative reconstruction algorithm to solve (1.8) for  $f$  called *Expectation Maximization* (EM) was introduced by Shepp and Vardi [SV82, VSK85]

$$f^{k+1} = f^k \frac{1}{A^T \mathbf{1}} A^T \frac{g}{A f^k}. \quad (1.9)$$

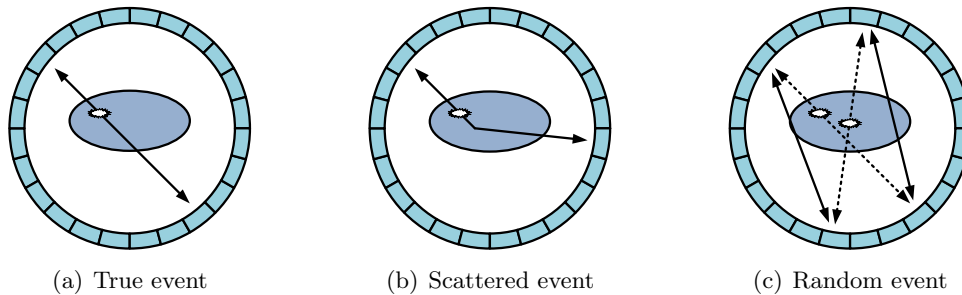


Figure 1.5: In the mathematically idealized PET model we only measure true events as in a). Since the particles may not only be absorbed but scattered as in b), the idealized model has to be extended. Also, due to the measurement process we may introduce another error source with the random events as in figure 1.5(c). Here the dotted lines are the true coincidences that should be measured but eventually the random coincidences represented by the solid lines are measured.

EM is widely used in real world application and there exists a plethora of modifications of the original version; we only mention the *Ordered Subset Expectation Maximization* (OSEM) developed by Hudson and Larkin [HL94] that reduces the reconstruction time by updating the image using only parts of the data. A detailed analysis of these algorithms can be found in [Kö06]. In contrast to the analytical models the system matrix  $A$  may be extended with any correction needed to imitate the PET measuring process. This is a nice feature since the presented algorithms of section 1.1 to derive  $f$  only work if the given data has the form (1.7). Unfortunately, there are several factors in PET disturbing the measurements and therefore the resulting  $f$ :

1. The positron may travel up to several mm before it annihilates with an electron. Therefore the assumption that the original decay took place on the line where the two gammas are measured is not really accurate. This effect is called positron range or positron offset [LH99]. Additionally the angle of the two photons is not always  $180^\circ$  but may vary up to 0.5% leading to wrong measurements especially in large detector rings. Usually these two effects are not corrected precisely.
2. The photons may not only get lost due to attenuation as modelled in (1.7) but get scattered on their way to the detectors - in some cases up to 60% [LK04]. Hence the photons are lost on the original line of response but they still may contribute to another measurement.
3. The measuring process that depends on the time resolution of the PET scanner may lead to problems if one accounts two photons of two different decays as a measurement. These events are called random events and can be up to 35% of all measured events [BKL<sup>+</sup>05].
4. The amount of activity in the scanner may lead to problems when comparing different acquisitions. Also, there may be more decays per second than the PET scanner can measure, which leads to the so-called dead time effect [MRH85].

Hence the line model itself can just be seen as a rough approximation of the real PET model. From here on we split the measurement  $M_{i,j}$  between two detectors  $d_i$  and  $d_j$  in

three components, true events ( $T_{i,j}$ ), random events ( $R_{i,j}$ ) and scattered events ( $S_{i,j}$ ):

$$M_{i,j} = T_{i,j} + R_{i,j} + S_{i,j}, \quad (1.10)$$

which are usually stored in a sinogram (see figure 1.2(b)) as in the case of CT or SPECT. The other effects usually only introduce a scaling of the data and not a different event type. Thus, we focus on scatter and randoms. So far we can only reconstruct  $f$  from  $M_{i,j}$  if  $R_{i,j}$  and  $S_{i,j}$  are zero. Otherwise the resulting  $f$  cannot be exact. Therefore one can think about two possible strategies to derive a quantitative image out of (1.10) given for a suitable number of detector combinations:

1. Estimate  $R_{i,j}$  and  $S_{i,j}$ , subtract the estimations from  $M_{i,j}$  and reconstruct  $f$  from  $T_{i,j}$  only,
2. Use the information still included in  $R_{i,j}$  and  $S_{i,j}$  to modify the PET model and reconstruct  $f$  directly from  $M_{i,j}$ .

As a next step we will give an overview of possible error sources in PET and corresponding correction techniques.

### 1.3.1 Decay correction

The radioactive labelled markers used in emission tomography decay over time depending on their half-life, i.e. on the time after which the amount of radioactivity is halved. In order to compare different measurements quantitatively the data has to be corrected for this decay. Assuming  $N_0$  is the activity at the beginning of the measurement. Then the activity at time  $t$  is given by

$$N(t) = N_0 \cdot 2^{-\frac{t}{T}},$$

where  $T$  denotes the half-life of the corresponding tracer. Thus the correction can be performed by multiplying  $N(t)$  with an adequate exponential factor.

Isotop	Element	Half-life
$^{124}I$	Iodine	4.176 days
$^{18}F$	Fluorine	109.77 min
$^{11}C$	Carbon	20.39 min
$^{13}N$	Nitrogen	9.965 min
$^{15}O$	Oxygen	2.04 min
$^{82}Rb$	Rubidium	1.273

Table 1.1: The tables [WA04] gives an overview of the half-life for commonly used PET tracer.

### 1.3.2 Deadtime correction

While converting photon energy to an electronical impulse the corresponding detector pair or even the complete scanner may be unable to detect new events for a while. This is not a problem if the activity inside the scanner is low because in that case the probability

is very low that another photon pair arrives at the same detector pair in this small time window.

To correct for this effect we have to multiply the number of measured events  $M$  by a factor  $> 1$  depending on the time window - called dead time - where no events can be measured, to obtain the correct number of events  $C$ . The correction factor depends on the way the scanner deals with events arriving in dead time state: do new events extend the dead time where no events can be measured or are new events dismissed while arriving during this time window? The former leads to a paralyzed system and the correction factor can be obtained from the relation

$$M = C \cdot e^{-C\tau},$$

where  $\tau$  denotes the system dead time. In case of a non-paralyzable system we have

$$C = M / (1 - M\tau).$$

For a detailed derivation of the corresponding formulas we refer to [SP87, Phe04].

### 1.3.3 Arc correction

For analytical reconstruction algorithms like the filtered backprojection we need equidistant sampled lines of responses. In real applications, this sampling usually does not exist due to the circular alignment of the detectors (see figure 1.6). Hence the measured coincidences have to be corrected for this misalignment [BBF<sup>+</sup>00]. As mentioned before, EM type algorithms can include a more detailed model of the different LORs and therefore use the exact detector positions. Thus we do not need to perform arc correction in that case.

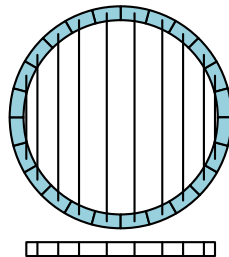


Figure 1.6: The LOR sampling changes due to the circular alignment of the detectors. The larger the distance to the center of the field of view is, the denser the different LORs become.

### 1.3.4 Random correction

Basically there are two different strategies to estimate the amount of random coincidences during a PET measurement. The first approach is based on the straight forward computation of the number of randoms from measured single coincidences. This is possible since each detector measures only single events, i.e. one of the two photons, and the underlying electronic creates the coincidences afterwards. Regarding two detectors  $d_i$  and  $d_j$ , the number of expected randoms between these two detectors is equal to

$$R_{i,j} = 2\tau s_i s_j$$

where  $s_i, s_j$  are the corresponding single rates and  $2\tau$  the coincidence window [LK04]. Due to the high number of single events the variance of this kind of random estimate is low provided all characteristics like system dead times are well known. If not, the calculated number of random events may be disturbed.

In contrast to the singles-based method the delayed window method does not calculate the number of randoms, but directly measure them. This is done by introducing a second coincidence window with a certain delay after the usual coincidence window.

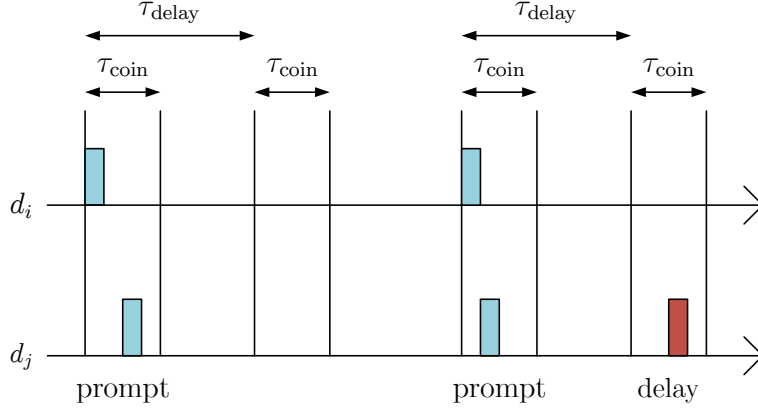


Figure 1.7: Estimation of random events by introducing a second coincidence window. The events measured in the first window may contain true, scatter as well as random events. None of the events measured in the second window can contribute to true coincidences since the maximum travel time of both photon is much shorter than the time delay  $\tau_{\text{delay}}$  so the measured events must be random, but may also be scattered on their way to the detectors.

With this delay one can assure that two measured singles in different time windows cannot originate from the same decay. This method is actually the gold standard [BKL<sup>+</sup>05] to estimate the random distribution, although it has some problems when applied to low statistic measurements. In this case the estimate may be very noisy. We mention that not all scanner support this technique, for example the quadHIDAC small animal PET scanner installed at the University Hospital at Münster [MMH<sup>+</sup>04], but most of the current scanners used in clinical applications do.

Recently a third approach was presented [Wat09] where both of the two approaches were combined in order to benefit from the advantages of each one.

The random coincidences do no longer contain any spatial information so there is no way to incorporate the randoms in the system model (1.7). Therefore we can only modify the data in order to correct for randoms.

Once the number of randoms  $R_{i,j}$  is calculated by one of these methods the correction can be performed as following:

$$\begin{aligned} M_{i,j} &= T_{i,j} + S_{i,j} + R_{i,j} \\ \Rightarrow M_{i,j} - R_{i,j} &= T_{i,j} + S_{i,j}, \end{aligned}$$

i.e. by simply subtracting the estimated number of randoms on each sinogram bin. Since one is mainly interested to reconstruct the image only from true coincidences there is still the need to estimate  $S_{i,j}$  or to get somehow else rid of the scattered coincidences.

### 1.3.5 Attenuation correction

As we can easily see from equation (1.7) we have to correct the measured data for the events that got lost due to attenuation. Since we are now interested in the reconstruction

of  $f$  only instead of in the reconstruction of  $\mu$  as in section 1.1 we use the attenuation coefficient  $\mu$  from an additional CT scan. Standalone PET scanners usually have a germanium (Ge68) source that rotates around the patient to perform a transmission scan prior or after to the emission scan in order to estimate  $\mu$  [ETC<sup>+</sup>02].

It is quite obvious that the attenuation correction with given  $\mu$  for a measurement  $M_{i,j}$  must have the following form

$$M_{i,j}^{AC} = M_{i,j} \cdot \exp\left(\int_{d_i}^{d_j} \mu ds\right), \quad (1.11)$$

but we are also interested in how the attenuation effects a photon and if it is really lost or just scattered to another direction. There are three ways for the interaction between the gamma energy- and material dependent linear attenuation coefficient  $\mu = \mu(E_\gamma, \text{material})$ , and photons:

1. Compton effect

The photon may interact with an electron by transferring some of its energy to the electron. This interaction results in a loss of photon energy on the one hand and in a change of the travelling direction of the photon on the other hand.

2. Photoelectric effect

If the photon transfers all its energy to the electron it ceases to exist and the photon is fully absorbed.

3. Electron-positron-pair production

This effect is only possible for gammas with energy of above 1.022 MeV, and therefore not in the case of PET.

Since the photoelectric effect has very small contributions to the total attenuation coefficient for soft tissue [MTJ<sup>+</sup>07] we will write  $\mu(E_\gamma, \text{material}) = \mu_{\text{Compton}}(E_\gamma, \text{material})$ . In the end we can say that attenuation in PET does not mean that we loose particles but that they are scattered and may therefore still be measured on a different coincidence line. A detailed description of the compton scattering process will be given in the scatter correction subsection.

### 1.3.6 Scatter correction

As we learned from the previous section nearly all attenuated particles are just scattered and not completely lost. Hence an accurate scatter correction is needed in order to obtain quantitative reconstructions.

Before we start to describe the different scatter correction techniques we will take a closer look at the Compton effect. If a photon with energy  $E_i$  interacts with an electron the energy after the scattering process is given by

$$E_s = P(E_i, \Theta) E_i, \quad (1.12)$$

$$P(E, \Theta) = \left(1 + \frac{E}{mc^2} (1 - \cos\Theta)\right)^{-1} \quad (1.13)$$

whereas the two constants  $m$  and  $c$  are the electron mass and the speed of light respectively [Wer01]. We can easily see the reduction of energy since the maximum of  $P(E, \Theta)$  in (1.13) is equal to 1 in the case  $\Theta = 0$ , and therefore  $E_s = E_i$ .

This equation only gives us information on how the energy changes during the scattering process but nothing about the angular distribution, i.e. which angle appears at which probability. This distribution is given by the Klein-Nishina cross section [Wer01]

$$\frac{d\sigma}{d\Omega} = \frac{r_e^2}{2} \left( P(E, \Theta) - P(E, \Theta)^2 \sin^2(\Theta) + P(E, \Theta)^3 \right) \quad (1.14)$$

i.e. the probability that a photon at energy  $E$  is scattered in direction  $\Theta$ . Here  $r_e$  is the classical electron radius. If we multiply the cross-section with the size of the solid angle we end up with the probability that a photon is scattered in this solid angle multiplied with the total cross section  $\sigma$  [Wer01], where  $\sigma$  is given by the integration of (1.14) over all possible solid angles, i.e.

$$\sigma(\alpha) = 2\pi r_e^2 \left\{ \frac{1 + \alpha}{\alpha^2} \left[ \frac{2 + 2\alpha}{1 + 2\alpha} - \frac{\ln(1 + 2\alpha)}{\alpha} \right] + \frac{\ln(1 + 2\alpha)}{2\alpha} - \frac{1 + 3\alpha}{(1 + 2\alpha)^2} \right\}, \quad (1.15)$$

where  $\alpha$  is the ratio of the current photon energy and the energy of an unscattered photon.

### Dual-energy window approaches

In the introduction of this subsection we described the energy loss of a photon that has interacted with an electron. The dual-energy window approach tries to take advantage of this effect by simply measuring events in different energy windows where all events with low energy must have undergone a scattering process. Unfortunately the detectors do not have a perfect energy resolution - otherwise one could use a threshold at 511 keV and neglect all photons with lower energy since they cannot be true events. Usually the two windows are set 380 to 850 keV for the higher and 200 to 380 keV for the lower window [GSS<sup>+</sup>96]. Due to measuring inefficiencies also true events might be assigned to the wrong energy level so that both windows contain scattered and unscattered events. The data in the large window is then corrected with knowledge from line source scans with and without scatter a medium. Finally the true events are estimated by subtracting the corrected scatter distribution of the lower energy window from the measurements

$$\begin{aligned} M_{i,j} &= T_{i,j} + S_{i,j} + R_{i,j} \\ \Rightarrow M_{i,j} - R_{i,j} - S_{i,j} &= T_{i,j}, \end{aligned}$$

where we assumed that an appropriate random correction was performed, too. This approach showed good results even in complex tests [Zai00] and may be improved with the development of PET detectors with a better energy resolution.

We mention that there are modifications of this approach by introducing more energy windows [SFK94].

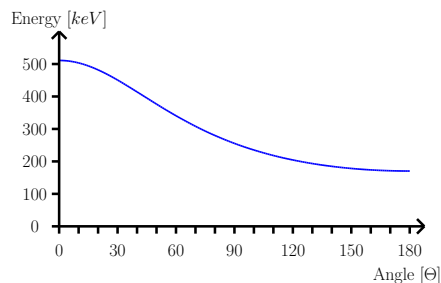


Figure 1.8: Starting with 511 KeV the energy distribution of single scattering is given by (1.12). As one can see the remaining energy even after scattering in 180° is still about 170 KeV.

### Analytical methods

Besides energy window approaches where the scattered events are directly measured it is possible to derive the amount of scatter from the measurements. We first present some simple analytical approaches. It is obvious that a measured coincidence line not intersecting the object must be a scattered event if we assume that the dataset is already random corrected. This knowledge can be used if we sort the measured lines of response into parallel projections and fit the background distribution with an exponential or gaussian function, where the area inside the object is interpolated. This method is legitimated by the fact that the scatter distribution is a low frequency function that will not vary that much from this estimate [CH95].

Another approach is the modelling using convolution or deconvolution techniques. Here we assume that the measured data  $g_m$  consists of two components, the unscattered  $g_u$  and the scattered events  $g_s$ :

$$g_m = g_u + g_s.$$

The scattered part  $g_s$  is approximately equal to the unscattered part convolved with a scatter kernel  $K$  and scaled by a constant  $k$  so that

$$g_m = g_u + g_s = g_u + k \cdot (g_u * K).$$

In order to derive  $g_u$  from  $g_m$  one may use the properties of the Fourier transform [JJGC85], i.e.

$$\begin{aligned} FT\{g_m\} &= FT\{g_u + k \cdot g_u * K\} \\ \Leftrightarrow FT\{g_m\} &= FT\{g_u\} + k \cdot FT\{g_u\} \cdot FT\{K\} \\ \Leftrightarrow \frac{FT\{g_m\}}{I + k \cdot FT\{K\}} &= FT\{g_u\} \\ \Leftrightarrow FT^{-1}\left\{\frac{FT\{g_m\}}{I + k \cdot FT\{K\}}\right\} &= g_u, \end{aligned}$$

or use more stable methods like an iterative algorithm [BM94]

$$\begin{aligned} g_u^n &= g_m - k \cdot (g_u^{n-1} * K), \\ g_u^1 &= g_m - k \cdot (g_m * K). \end{aligned}$$

For  $K$  usually a monoexponential function is used. A serious drawback is the fact that the scaling parameter  $k$  and the scatter kernel  $K$  have to be known prior to use this approach. Nevertheless the iterative approach shows good results if the necessary parameters are chosen carefully.

The next two correction methods will be presented in detail since they are very similar to the model we will derive in the next chapters.

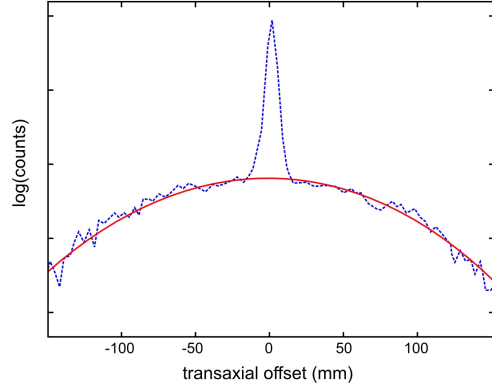


Figure 1.9: A Gaussian (red line) is fitted to the 3D PET projection data (blue line) in order to determine the scatter distribution.

### Modelbased Scatter Correction I: Single Scatter Simulation

The main idea of this approach is to estimate the amount of scatter in each coincidence line by the scatter contribution from a number of small volumes distributed all over the scanned object [Wat00]. If the number of volumes is high enough we should obtain a good estimation of the scatter distribution for each coincidence line. These kind of approaches can be viewed as simplifications of complex Monte Carlo methods, where the full physical process is modelled in detail. Let  $S$  be the center of a small volume  $dV$ . We are interested in the contribution of  $S$  to the measurements between the two detectors  $d_i$  and  $d_j$ , whereas  $S$  is not on the straight line between these detectors (see Figure 1.10). Again, let  $f$  be the sought-after activity distribution. According to (1.7) the number of ‘coincidences’ between  $d_i$  and  $S$  is proportional to

$$I_{d_i S} \approx \int_{d_i}^S f(x) dx \cdot e^{-\int_{d_i}^S \mu(E_0, x)}. \quad (1.16)$$

In addition to (1.7) we add the energy dependency of  $\mu$  in (1.16). At this point we only have unscattered events so the current energy must be equal to those of the emitted particles, i.e.  $E_0 = 511$  keV. As a next step we have to estimate the amount of particles that are scattered towards the second detector  $d_j$ . For the given scattering angle  $\Theta$  we will use the scatter kernel (1.14) which leads to

$$I_{d_i S} \approx \int_{d_i}^S f(x) dx \cdot e^{-\int_{d_i}^S \mu(E_0, x)} \frac{d\sigma(\Theta)}{d\Omega} \cdot e^{-\int_S^{d_j} \mu(E_S, x)}, \quad (1.17)$$

whereas the new energy level  $E_S$  is given by (1.12). As we learned from the dual-energy window approach the detectors have an upper and a lower bound to measure photons. Also, the detection efficiency depends on this energy level, the higher the energy the higher the detection efficiency [Wer01]. This energy dependency will be included in this model by the scaling factor  $\epsilon_{d_i}(E_0)$  and  $\epsilon_{d_j}(E_S)$ . Since the solid angle given by  $d_i$  and  $d_j$  differs depending on the position of  $S$  we introduce two additional coefficients, whereas  $\sigma_{d_i}, \sigma_{d_j}$  represent the cross section of  $d_i, d_j$  normal to  $\overline{d_i S}$  and  $\overline{S d_j}$ , and  $r_{d_i}, r_{d_j}$  the distance between  $S$  and the two detectors. Finally we have

$$I_{d_i S} \approx \int_{d_i}^S f(x) dx \cdot e^{-\int_{d_i}^S \mu(E_0, x)} \frac{d\sigma(\Theta)}{d\Omega} \cdot e^{-\int_S^{d_j} \mu(E_S, x)} \epsilon_{d_i}(E_0) \epsilon_{d_j}(E_S) \frac{\sigma_{d_i}}{r_{d_i}^2} \frac{\sigma_{d_j}}{r_{d_j}^2}. \quad (1.18)$$

Obviously (1.18) just considers the case where the scattering process takes place between the emission point and  $S$  towards  $d_j$ . To estimate the other possible case we may write

$$I_{d_j S} \approx \int_{d_j}^S f(x) dx \cdot e^{-\int_{d_j}^S \mu(E_0, x)} \frac{d\sigma(\Theta)}{d\Omega} \cdot e^{-\int_S^{d_i} \mu(E_S, x)} \epsilon_{d_j}(E_0) \epsilon_{d_i}(E_S) \frac{\sigma_{d_j}}{r_{d_j}^2} \frac{\sigma_{d_i}}{r_{d_i}^2}. \quad (1.19)$$

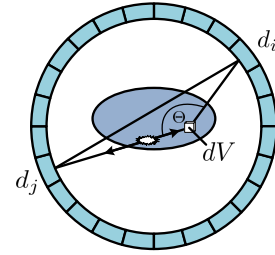


Figure 1.10: The amount of scatter in the measurements between  $d_i$  and  $d_j$  is estimated by the contribution of several volumes  $dV$  distributed all over the target object.

If we combine (1.18) and (1.19) we have the full estimate for the contribution of  $S$  to the measurements between  $d_i$  and  $d_j$ . In order to estimate the complete amount of scatter we have to integrate over all possible scattering volumes  $S_n$

$$I_{d_i d_j} = \sum_{n=1}^N (I_{d_i S_n} + I_{d_j S_n}). \quad (1.20)$$

For a given emitter distribution  $f$  and a given attenuation map  $\mu$  the contribution of each scatter volume to each line of response can now be calculated. This can be very time demanding on one hand - several million lines of responses - and due to the fact that an emission image  $f$  has to be known prior to this process the estimated scatter distribution may not necessary be exact on the other hand. To reduce the calculation time the scanner geometry is usually simplified and the missing data is interpolated afterwards. By incorporating the scatter estimation in the reconstruction algorithm the estimates should become better with each iteration step since each update is performed with a more precise estimation image  $f$  [WBD<sup>+</sup>02]. Regarding the classical EM algorithm presented in (1.9) the scatter estimated is added to the forward projection

$$f^{k+1} = f^k \frac{1}{A^T \mathbf{1}} A^T \frac{g}{A f^k + \lambda^k S^k(f^k, \mu)}, \quad (1.21)$$

where the scaling parameter  $\lambda^k$  has to be recalculated each iteration by fitting the scatter estimation to the measurements in the scatter-free regions, i.e. where no true measurement can be measured because the lines of responses do not intersect the object. Usually only a few updates of the scatter estimates are necessary before it converges. Afterwards one may iterate the image update only. This method is still the gold standard for scatter correction in PET since it has a good balance between complexity and accuracy.

### Modelbased Scatter Correction II: High accuracy multiple scatter modelling

A recent publication of Markiewicz [MTJ<sup>+</sup>07] can be seen as a refinement of the single scatter simulation. The main difference to the previously presented model is the fact that the scatter distribution is found for each voxel of the grid separately. Therefore the scatter distribution may be included in the forward model of the reconstruction algorithm as in [LBB<sup>+</sup>05]. We start with an emission location  $Z$  where photons are emitted pairwise in opposite directions. The amount of particles arriving unscattered at detector  $d_i$  are proportional to the solid angle  $\beta_{d_i}$  subtended at  $Z$  by the detector and has to be scaled by half the maximum possible solid angle since it is not important which of the two particles arrive at detector  $d_i$

$$\epsilon_i = \frac{\beta_{d_i}}{2\pi}.$$

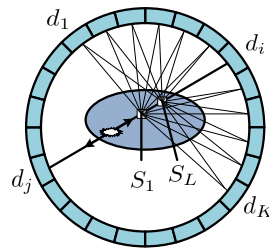


Figure 1.11: For each voxel the whole scatter system response is calculated leading to a scatter sinogram for each individual voxel.

Regarding a scattering segment  $S$  along the vector  $Z\vec{d}_i$  the probability of a photon pair emitted in  $Z$  arriving unscattered in  $S$  and  $d_j$  is equal to

$$P_i(Sd_iZ) = \epsilon_i \exp \left( - \int_{-r_{d_i}}^{r_s} \mu(l\hat{d}_i + z) dl \right),$$

where  $z$  denotes the position of  $Z$ , and  $r_s, r_{d_i}$  are constants equal to  $|Z\vec{S}|, |d_i\vec{S}|$ , and  $\hat{d}_i$  is a vector normal to the detector  $d_i$ . The probability that of two particles emitted in  $Z$  one is measured unscattered in  $d_i$  while the other is scattered in  $S$  is given by

$$P_S(Sd_iZ) = P_i(Sd_iZ) \left( 1 - \exp \left( - \int_{-l_s/2}^{l_s/2} \mu(l\hat{u} + s) dl \right) \right).$$

The solid angle subtended at  $S$  by the second detector is given by  $\Omega_j$ . As explained on the previous sections scattering of photons is combined with a loss of energy. The mumap has to be modified according to the different photon energies. Finally, by using the Klein-Nishina cross section we have the probability that a particle scattered in  $S$  by  $\Theta$  is measured at  $d_j$  while the other particles is measured unscattered at  $d_i$  is

$$P_S(d_j S d_i Z) = P_S(Sd_iZ) \frac{\Omega_j}{\sigma} \frac{d\sigma}{d\Omega} \exp \left( -c_{d_j} \int_0^{r_{d_j}} \mu(l\hat{u} + s) dl \right). \quad (1.22)$$

In order to obtain the full scatter sinogram for the emission point  $Z$  we have to sum up all possible detector combinations as well as all scattering segments

$$P_S(Dd_iZ) = \sum_{j=1}^D \sum_{l=1}^L P_S(d_j S_l d_i Z), \quad (1.23)$$

where  $D$  represents all detectors that received a scattered photon. The extension to scattering of multiple scatter is obvious. This new scatter distribution may now be included directly in the reconstruction algorithm as well as used analog to the single scatter simulation. In the latter case one expects a higher accuracy do to the finer sampling which comes along with a higher computation time. It was shown that the accuracy of this approach is comparable to Monte Carlo simulations.

The main difference between those two models is the way the scatter information is stored. While in the first model the amount of scatter for each line is stored, the second model needs much more data to be saved since the amount of scatter for all combinations of voxels and lines of response are used. Later we will see that our model is very similar to the second one although we use a different way to derive the model.

Before we step to the next chapter where we present our new model, we like to mention that there are other factors degrading the acquisition of the data and the reconstruction respectively, like motion of the patient. We refer to Wernick and Aarsvold [WA04] for a detailed overview of all possible factors.



## Chapter 2

# The Scatter Model for PET Based on the Boltzmann Equation

As explained in chapter 1, there are many different scatter correction techniques for PET. Most of them can be divided into two parts:

1. estimate the amount of scatter in the measured data,
2. subtract the estimated scatter distribution from the measured data.

In some methods, e.g. in the convolution-subtraction method of Bailey and Meikle or the single scatter simulation of Watson, both steps are combined into an iterative algorithm to improve the estimation process. All these methods lead to reduced statistics due to the subtraction of scattered events. More than 35%, in some cases up to 60%, of the measured data may undergo a scattering process [LK04] so neglecting all this information may lead to bad results especially in the case of low statistic measurements.

Instead of dropping scattered events one may try to still use the information contained in those events and reconstruct from all data using a more complex system model. This strategy has been successfully applied to SPECT [FT93] and there are also some approaches for PET like Monte Carlo reconstructions [RA07] where the full decay-to-detection process is simulated in detail. In the projection step of the reconstruction algorithm the projection volume is no longer restricted to a simple line but is extended to the full reconstruction volume in the worst case.

One thing still missing is a detailed mathematical model describing the complete scatter process in PET. In this chapter we will introduce a new analytical scatter model based on the work of Natterer and Wübbeling [NW04] that uses the stationary Boltzmann equation to model the photon movement. The resulting representation can be seen as a refinement of the classical line model for PET (1.7). Similar to the work of Markiewicz the scatter fraction of each source point for each line of response is computed leading to a complex projection volume.

This chapter is organized as follows. Section 2.1 gives a motivation for the use of the Boltzmann equation, while section 2.2 introduces the new scatter model.

## 2.1 The Stationary Boltzmann Equation

We start with a simple motivation for the use of the stationary Boltzmann equation. The Boltzmann equation is usually time dependent, therefore we will introduce the full equation and deduce the stationary state afterwards. We follow the lines of [Wü06] and [BGCC99]. Let  $u(x, \Theta, E, t)$  be the density of particles at  $x \in \mathbb{R}^3$  moving in direction  $\Theta \in S^2$  with energy  $E$  at a certain time  $t$ . If particles starting at  $t = 0$  continue their way in direction  $\Theta$  and there are neither sources nor do the particles interact with tissue, the density will not change along the path from  $x$  to  $x + t\Theta$ , and we have

$$u(x + t\Theta, \Theta, E, t) = u(x, \Theta, E, 0). \quad (2.1)$$

However, since particles in PET interact frequently with tissue we have to introduce some modifications to (2.1). Some particles may get lost on their path due to attenuation

$$u(x + t\Theta, \Theta, E, t) = u(x, \Theta, E, 0) - \int_0^t \mu(x + \tau\Theta, E) u(x + \tau\Theta, \Theta, E, \tau) d\tau,$$

while other particles may get scattered in direction  $\Theta$

$$\begin{aligned} u(x + t\Theta, \Theta, E, t) &= u(x, \Theta, E, 0) - \int_0^t \mu(x + \tau\Theta, E) u(x + \tau\Theta, \Theta, E, \tau) d\tau \\ &+ \int_0^t \int_{S^2} \int_E^{E_0} k(x + \tau\Theta, \Theta, \Theta', E, E') u(x + \tau\Theta, \Theta', E', \tau) dE' d\Theta' d\tau. \end{aligned}$$

Here  $\mu(x, E)$  denotes the energy dependent absorption coefficient and  $k(x, \Theta, \Theta', E, E')$  represents the probability that a particle arriving at  $x$  in direction  $\Theta'$  with energy  $E'$  continues its path in direction  $\Theta$  with energy  $E$ . Since the scattering process always leads to energy loss we only have to integrate from  $E$  to  $E_0 = 511$  keV.

From section 1.3 we know that absorption in PET can be identified with compton scatter. Hence we do not have to add another integral containing the particles that got lost due to scatter.

As mentioned above there may also be sources  $q(x, E, t)$  on the path from  $x$  to  $x + t\Theta$ . In PET the emitted particles always have the energy  $E_0$  leading to the following relationship between  $u(x, \Theta, E, 0)$  and  $u(x + t\Theta, \Theta, E, t)$

$$\begin{aligned} u(x + t\Theta, \Theta, E, t) &= u(x, \Theta, E, 0) - \int_0^t \mu(x + \tau\Theta, E) u(x + \tau\Theta, \Theta, E, \tau) d\tau \\ &+ \int_0^t \int_{S^2} \int_E^{E_0} k(x + \tau\Theta, \Theta, \Theta', E, E') u(x + \tau\Theta, \Theta', E', \tau) dE' d\Theta' d\tau \\ &+ \delta(E - E_0) \int_0^t q(x + \tau\Theta, \Theta, \tau) d\tau. \end{aligned}$$

The delta distribution  $\delta(E - E_0)$  is meaningful at this point because we will integrate over all possible energies  $E$  afterwards to model the measuring process. Taking the partial derivative with respect to  $t$  gives the time dependent Boltzmann equation:

$$\begin{aligned} \frac{\partial u}{\partial t}(x, \Theta, E, t) + \theta \cdot \nabla_x u(x, \Theta, E, t) &= -\mu(x, E) u(x, \Theta, E, t) + \delta(E - E_0) q(x, \Theta, t) \\ &+ \int_{S^2} \int_E^{E_0} k(x, \Theta, \Theta', E, E') u(x, \Theta', E, t) dE' d\Theta'. \end{aligned}$$

Due to the short transit time of photons crossing the body we assume  $u$  to be stationary for our model, i.e. there is no more dependency on  $t$ . There are some approaches that try to measure the time difference between arriving photons - in this case time dependency cannot be neglected anymore [Wat07], but we will focus on the stationary equation.

With  $\partial u / \partial t = 0$  we finally arrive at the stationary Boltzmann equation:

$$\begin{aligned} \theta \cdot \nabla_x u(x, \Theta, E) + \mu(x, E) u(x, \Theta, E) &= \int_{S^2} \int_E^{E_0} k(x, \Theta, \Theta', E, E') u(x, \Theta', E') dE' d\Theta' \\ &+ \delta(E - E_0) q(x, \Theta). \end{aligned} \quad (2.2)$$

Now we are able to track moving particles originating from the source  $\delta(E - E_0) q(x, \Theta)$  even if they interact with tissue by solving (2.2). For a unique solution we need to impose boundary conditions. Hence we restrict  $x$  to  $D \subset \mathbb{R}^3$  and postulate

$$u(x, \Theta, E) = 0, \quad \text{for } x \in \partial D, \quad \Theta \cdot \nu_x > 0, \quad (2.3)$$

whereas  $\nu_x$  is the inner normal on  $x \in \partial D$ . Following [DL93] and [BGCC99] we introduce for a fixed point  $x \in D$  and a fixed direction  $\Theta \in S^2$  the function

$$F(t) = u(x + t\Theta, \Theta, E) \quad (2.4)$$

and define  $t_0(x, \Theta) < 0$  as the value of  $t$ , such that  $x + t_0(x, \Theta)\Theta \in \partial D$ . From (2.2)-(2.4) we deduce the new boundary value problem

$$\begin{aligned} F'(t) &= \Theta \cdot \nabla_x u(x + t\Theta, \Theta, E) \\ &= \int_{S^2} \int_E^{E_0} k(x + t\Theta, \Theta, \Theta', E, E') u(x + t\Theta, \Theta', E') dE' d\Theta' \\ &\quad + \delta(E - E_0) q(x + t\Theta, \Theta) - \mu(x + t\Theta, E) F(t), \end{aligned} \quad (2.5)$$

$$F(t_0(x, \Theta)) = 0. \quad (2.6)$$

Starting with the ansatz

$$F(t) = c(t) e^{-\int_0^t \mu(x + \tau\Theta, E) d\tau}$$

we can easily deduce

$$\begin{aligned}
 F'(t) &= c'(t) e^{-\int_0^t \mu(x+\tau\Theta, E) d\tau} - \mu(x+t\Theta, E) c(t) e^{-\int_0^t \mu(x+\tau\Theta, E) d\tau} \\
 &= c'(t) e^{-\int_0^t \mu(x+\tau\Theta, E) d\tau} - \mu(x+t\Theta, E) F(t).
 \end{aligned} \tag{2.7}$$

From (2.5)-(2.7) we know

$$\begin{aligned}
 c'(t) &= \left( \int_{S^2} \int_E^{E_0} k(x+t\Theta, \Theta, \Theta', E, E') u(x+t\Theta, \Theta', E') dE' d\Theta' \right. \\
 &\quad \left. + \delta(E-E_0) q(x+t\Theta, \Theta) \right) e^{-\int_0^t \mu(x+\tau\Theta, E) d\tau} \\
 \Rightarrow c(t) &= \int_{t_0(x, \Theta)}^t \left( \int_{S^2} \int_E^{E_0} k(x+s\Theta, \Theta, \Theta', E, E') u(x+s\Theta, \Theta', E') dE' d\Theta' \right. \\
 &\quad \left. + \delta(E-E_0) q(x+s\Theta, \Theta) \right) e^{-\int_0^s \mu(x+\tau\Theta, E) d\tau} ds \\
 \Rightarrow F(t) &= \int_{t_0(x, \Theta)}^t \left( \int_{S^2} \int_E^{E_0} k(x+s\Theta, \Theta, \Theta', E, E') u(x+s\Theta, \Theta', E') dE' d\Theta' \right. \\
 &\quad \left. + \delta(E-E_0) q(x+s\Theta, \Theta) \right) e^{-\int_0^s \mu(x+\tau\Theta, E) d\tau} e^{-\int_0^t \mu(x+\tau\Theta, E) d\tau} ds.
 \end{aligned}$$

Finally we get a new representation for  $u(x, \Theta, E)$ , because

$$\begin{aligned}
 u(x, \Theta, E) &= F(0) \\
 &= \int_{t_0(x, \Theta)}^0 \left( \int_{S^2} \int_E^{E_0} k(x+s\Theta, \Theta, \Theta', E, E') u(x+s\Theta, \Theta', E') dE' d\Theta' \right. \\
 &\quad \left. + \delta(E-E_0) q(x+s\Theta, \Theta) \right) e^{-\int_0^s \mu(x+\tau\Theta, E) d\tau} ds \\
 &= \int_{t_0(x, \Theta)}^0 \left( \int_{S^2} \int_E^{E_0} k(x+s\Theta, \Theta, \Theta', E, E') u(x+s\Theta, \Theta', E') dE' d\Theta' \right. \\
 &\quad \left. + \delta(E-E_0) q(x+s\Theta, \Theta) \right) e^{-\int_s^0 \mu(x+\tau\Theta, E) d\tau} ds.
 \end{aligned} \tag{2.8}$$

If scattering is prohibited (i.e.  $k = 0$ ) or if scattered events can somehow be discriminated, the double integral on the right side containing the function  $u$  vanishes and we gain an explicit solution for  $u$ . In that case  $u$  is obviously obtained by integrating the source along the path from  $x$  to  $x + t_0(x, \Theta)\Theta$ , since only sources on this line may contribute to the measurement.

## 2.2 The Scatter Model

In this section we will introduce our new scatter model based on the Boltzmann equation. Therefore the model of Natterer and Wübbeling [NW04] is extended by the energy dependency of photons and the exact scatter kernel. We will show that in the absence of scatter the new model reduces to the classical line model of PET presented in chapter 1. In case where scattering occurs the model coincides with the scatter models proposed by Watson [Wat00] and Markiewicz [MTJ<sup>+</sup>07]. We emphasize that this new model is derived from a purely mathematical point of view while the other models are motivated by physical considerations.

We model the PET scanner as a cylinder  $C$  with radius  $R$  and boundary

$$\Gamma = \{x : x_1^2 + x_2^2 = R^2, x_3 \in [0, L]\}.$$

For a suitable boundary condition we assume that we have no incoming radiation from outside  $C$ . We write for each  $\theta \in S^2$

$$\Gamma_\theta = \{x \in \Gamma : \nu_x \cdot \theta \geq 0\},$$

with  $\nu_x$  being the inner normal vector on  $x \in \Gamma$ , and postulate

$$u(x, \Theta, E) = 0 \quad \text{for } x \in \Gamma_\theta. \quad (2.9)$$

In real world applications one can have radiation outside  $C$  because a human PET scanner usually covers only a small part of the patients body - in general the scanner has an axial field of view (FOV) of 15-25 cm. To reduce the effect of activity outside the ring an annular lead shielding is attached at the axial ends of the PET scanner. In head and body studies with and without additional side-shielding it has been shown [SMB<sup>+</sup>98] that the effect of scattered events from outside the FOV is not severe. This justifies not to track particles that move outside the scanner and are scattered back, eventhough we note that the model may be extended to include this special case if necessary. Nevertheless the extra shielding improves the statistical quality of the data by a smoother randoms distribution but it obviously decreases the port diameter of the PET scanner.

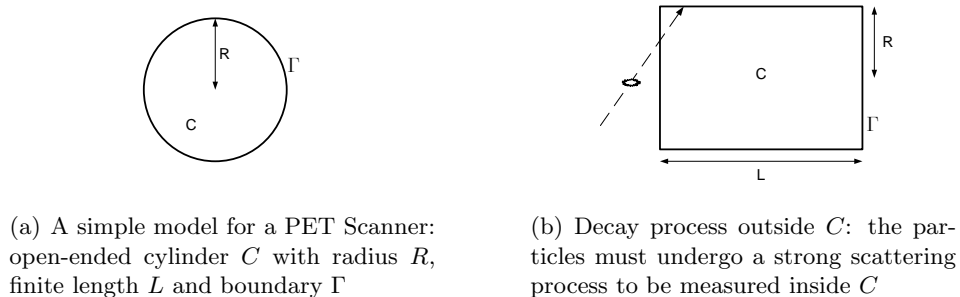


Figure 2.1: Activity outside the cylinder  $C$  is unlikely to contribute to real measurements but may introduce noise like random coincidences. Correction methods for random coincidences have been discussed in chapter 1.

The main idea of the new scatter model is to emit a pair of particles in each point of the FOV and in each direction and track them on their way to the detectors in order to estimate the number of coincidences for each detector pair.

From section 1.3.6 we know that the probability of photon scatter in  $x \in C$  is given by  $(1 - \exp(-\mu(x, E)))$ , while the Klein-Nishina cross-section (1.14) can be used for the angular distribution. Similar considerations can be found in [BGCC99]. In combination with the photon energy loss (1.12) we write  $\kappa(\Theta \cdot \Theta', E, E')$  for the probability that a photon flying in direction  $\Theta'$  with energy  $E'$  is scattered towards  $\Theta$  with a resulting energy  $E < E'$ . By merging these two components we obtain a more precise description for our scatter kernel  $k(x, \Theta, \Theta', E, E')$  introduced in section 2.1:

$$k(x, \Theta, \Theta', E, E') = (1 - \exp(-\mu(x, E))) \kappa(\Theta \cdot \Theta', E, E'). \quad (2.10)$$

Using the notation introduced above we now write analogous to (1.22) for the probability that two particles emitted in  $z \in C$  in opposite directions and measured by the two detectors  $d_i$  and  $d_j$  whereas one particle is scattered at  $x \in C$  before arriving at  $d_j$

$$P(d_i, z, x, d_j) = \Omega_{d_i} e^{-\int_{d_i}^x \mu(s, E_0) ds} k\left(x, \frac{d_j - x}{|d_j - x|}, \frac{x - d_i}{|x - d_i|}, E, E_0\right) e^{-\int_x^{d_j} \mu(s, E) ds} \Omega_{d_j}. \quad (2.11)$$

The extension to multiple scatter is obvious: we just have to track the emitted particle on its way to the detector and regard each possible scatter point on the path. The tracking of the corresponding opposite particle is of course much easier. We generalise (2.11) and write

$$P^{0,k}([d_i, E_i, \Theta_i], z, \pm\omega, [d_j, E_j, \Theta_j]) = v_{z,\omega}^0(d_i, E_i, \Theta_i) v_{z,-\omega}^k(d_j, E_j, \Theta_j), \quad (2.12)$$

where  $v^0$  is the path of the photon and therefore the probability that the photon emitted in  $z$  in direction  $\omega$  hits  $d_i$  from direction  $\Theta_i$  at the energy level  $E_i$  without any scattering while in  $v^k$  scattering is allowed. Analog computations can be performed if the scattering occurs in the opposite direction as well as in both directions or finally if both photons arrive at the detector unscattered. It is obvious, that each photon pair can only contribute to one if these four cases. Hence the probability that two particles emitted at  $z$  in opposite directions and measured by the two detectors is equal to the sum of these four

$$\begin{aligned} P([d_i, E_i, \Theta_i], z, \pm\omega, [d_j, E_j, \Theta_j]) &= v_{z,\omega}^0(d_i, E_i, \Theta_i) v_{z,-\omega}^k(d_j, E_j, \Theta_j) \\ &+ v_{z,\omega}^k(d_i, E_i, \Theta_i) v_{z,-\omega}^0(d_j, E_j, \Theta_j) \\ &+ v_{z,\omega}^k(d_i, E_i, \Theta_i) v_{z,-\omega}^k(d_j, E_j, \Theta_j) \\ &+ v_{z,\omega}^0(d_i, E_i, \Theta_i) v_{z,\omega}^0(d_j, E_j, \Theta_j). \end{aligned} \quad (2.13)$$

As the next step we use the Boltzmann equation to model (2.13). First we need to solve the boundary value problem (2.2), (2.9) for both emitted photons and separate the scattered and unscattered parts. Since we are interested in tracking single particles moving through the scanner, we choose a special source distribution

$$q(x, \Theta) = \delta(x - z) \delta(\Theta - \omega). \quad (2.14)$$

From (2.8) we know that the solution of this BVP is given by

$$\begin{aligned} u_{z,\omega}(x, \Theta, E) &= \int_{t_0(x, \Theta)}^0 \left( \int_{S^2} \int_E^{E_0} k(x + s\Theta, \Theta, \Theta', E, E') u_{z,\omega}(x + s\Theta, \Theta', E') dE' d\Theta' \right. \\ &\quad \left. + \delta(x + s\Theta - z) \delta(\Theta - \omega) \delta(E - E_0) \right) e^{-\int_s^0 \mu(x + s'\Theta, E) ds'} ds \end{aligned}$$

$$\begin{aligned}
 \Leftrightarrow u_{z,\omega}(x, \Theta, E) &= \underbrace{\int_{t_0(x,\Theta)}^0 \int_{S^2} \int_{E_{\min}}^{E_0} k(x+s\Theta, \Theta, \Theta', E, E') u_{z,\omega}(x+s\Theta, \Theta', E') dE' d\Theta'}_{=: u_{z,\omega}^k(x,\Theta,E)} \\
 &\quad \times \underbrace{e^{-\int_s^0 \mu(x+s'\Theta, E) ds'}}_{=: u_{z,\omega}^0(x,\Theta,E)} \\
 &+ \underbrace{\int_{t_0(x,\Theta)}^0 \delta(x+t\Theta-z) e^{-\int_t^0 \mu(x+s'\Theta, E) ds'} dt \delta(\Theta-\omega) \delta(E-E_0)}_{=: u_{z,\omega}^0(x,\Theta,E)} \\
 &= u_{z,\omega}^k(x, \Theta, E) + u_{z,\omega}^0(x, \Theta, E).
 \end{aligned}$$

This is of course not an explicit solution as  $u$  still appears on the right side, but at least a formal solution is given by a Neumann series whose convergence can be argued on physical grounds in this case following [BGCC99]. We omit a mathematical convergence analysis at this point and refer to [Bon98] for details.

The two components  $u_{z,\omega}^k$  and  $u_{z,\omega}^0$  represent the scattered and unscattered particle traces needed to model (2.13). Hence we write

$$P([d_i, E_i, \Theta_i], z, \pm\omega, [d_j, E_j, \Theta_j]) = u_{z,\omega}(d_i, E_i, \Theta_i) u_{z,-\omega}(d_j, E_j, \Theta_j), \quad (2.15)$$

with  $u_{z,\pm\omega}$  being the solutions of the BVP. For completeness one should add two factors including the detection efficiencies of the different detectors as well as the corresponding solid angles, but at the moment we will neglect them. Additionally, we do not model the detector width in order to use some well-known space estimates in the upcoming sections. We mention that Mair [Mai00] presented a theoretical framework that incorporates the effects of detector width (but neglects scatter) in 2D PET. For the implementation of our new model in chapter 4 we will include all these modifications.

Since we are not interested in the characterization of single emission / detection directions or energy levels we have to extend (2.15). Now we have an expression for the probability that two particles are emitted in opposite directions in  $z \in C$  and measured by  $d_i, d_j$  from any direction with any energy level using the Boltzmann equation

$$\begin{aligned}
 G_z(d_i, d_j) &= \int_{S^2} \int_{S^2} \int_{S^2} \int_{E_{\min}}^{E_0} \int_{E_{\min}}^{E_0} u_{z,\omega}(d_i, E_i, \Theta_i) u_{z,-\omega}(d_j, E_j, \Theta_j) dE_i dE_j d\Theta_i d\Theta_j d\omega, \\
 &= \underbrace{\int_{S^2} \int_{S^2} \int_{E_{\min}}^{E_0} u_{z,\omega}(d_i, E_i, \Theta_i) dE_i d\Theta_i}_{=: G_{z,\omega}(d_i)} \underbrace{\int_{S^2} \int_{E_{\min}}^{E_0} u_{z,-\omega}(d_j, E_j, \Theta_j) dE_j d\Theta_j}_{=: G_{z,-\omega}(d_j)} d\omega, \\
 &= \int_{S^2} G_{z,\omega}(d_i) G_{z,-\omega}(d_j) d\omega. \quad (2.16)
 \end{aligned}$$

Regarding the two energy integrals the lower limit is  $E_{\min}$  and not zero. As mentioned in the introduction, PET scanner usually have a certain lower energy threshold and dismiss

all particles that are measured with less energy. Of course  $E_{\min}$  may equally be defined as zero to increase the sensitivity of the scanner, but this choice would increase the number of scattered events in the measurements as well.

Finally for a continuous source distribution  $f$  we obtain the PET model, i.e. the expected number particles  $M_{i,j}$  emitted in any direction somewhere in  $f$  and measured by the two detectors  $d_i$  and  $d_j$  on the boundary of  $C$ :

$$M_{i,j} = \int_C G_z(d_i, d_j) f(z) dz. \quad (2.17)$$

On the right hand side we introduce the operator  $M$  acting on  $f$  as

$$M_{i,j} = Mf(d_i, d_j) = \int_C G_z(d_i, d_j) f(z) dz. \quad (2.18)$$

In the following sections we will give a detailed analysis of the structure of  $M$ , including the special cases of no scatter, single scatter and full scatter. The final goal is the derivation - if possible - of an inverse operator  $M^{-1}$  to reconstruct  $f$  from the measurements  $M_{i,j}$  which will be discussed in chapter 3.

Until this point we did not postulate any restrictions on  $f$  or  $\mu$ . We assume that they are suitable so that all integrals are well-defined and give an overview of the exact restrictions in chapter 3.

We like to mention the work of Gebennus [Geb09] who derived a similar but more stochastically motivated transport model for PET that also uses the Boltzmann equation.

### 2.2.1 The Case of No Scatter

The classical line model for PET (1.7), as presented in chapter 1, is reasonable only if scatter is neglected. Hence it is desirable that a new model reduces to the old one if  $k = 0$ . We will show that our model satisfies this demand. Although we know that we always have scatter as long as we have attenuation, it is useful to analyze this case for our further work. Throughout this chapter we assume that we only measure true and scatter events, i.e. random events are not part of our data. We will write  $M_{i,j} = T_{i,j} + S_{i,j}$ .

**Theorem 2.2.1** *Let  $k = 0$ . Then the operator  $M$  defined in (2.18) reduces to the established line model of PET, i.e. the X-ray transform, plus an additional scaling factor*

$$M_{i,j} = Mf(d_i, d_j) = \frac{e^{-\int_{d_j}^{d_i} \mu(s, E_0) ds}}{|d_i - d_j|^2} \int_{d_j}^{d_i} f ds. \quad (2.19)$$

Proof: If  $k = 0$  the scatter integral vanishes and the transport equation (2.2) is reduced to

$$\theta \cdot \nabla_x u(x, \theta, E) + \mu(x, E) u(x, \theta, E) = q(x, \theta) \delta(E - E_0). \quad (2.20)$$

The solution of (2.20) at  $d_i \in \Gamma$  with the boundary conditions (2.9) and the delta source (2.14), i.e. the measurement in detector  $d_i$  from direction  $\Theta$  on the boundary of the cylinder  $C$  if a particle in  $z$  is emitted in direction  $\omega$  is given by

$$G_{z,\omega}^0(d_i, \theta, E) = \int_{s_0(d_i, \Theta)}^0 \delta(d_i + s\theta - z) \delta(\Theta - \omega) \delta(E - E_0) e^{-\int_s^0 \mu(d_i + s'\theta, E) ds'} ds. \quad (2.21)$$

We write  $G_{z,\omega}^0(d_i, \Theta, E)$  instead of  $G_{z,\omega}(d_i, \Theta, E)$  to emphasize that  $k = 0$ . Integration over  $\Theta$  eliminates the detection direction dependency while integration over  $E$  is necessary to model the energy resolution and leads to

$$\begin{aligned} G_{z,\omega}^0(d_i) &= \int_{S^2} \int_{E_{\min}}^{E_0} \int_{s_0(d_i, \Theta)}^0 \delta(d_i + s\theta - z) \delta(\Theta - \omega) \delta(E - E_0) e^{-\int_s^0 \mu(d_i + s'\theta, E) ds'} ds dE d\Theta \\ &= \int_{s_0(d_i, \omega)}^0 \delta(d_i + s\omega - z) e^{-\int_s^0 \mu(d_i + s'\omega, E_0) ds'} ds. \end{aligned}$$

For a complete PET measurement we have to regard the measurements in a second detector  $d_j$ . From (2.16) we have

$$\begin{aligned} G_z^0(d_i, d_j) &= \int_{S^2} G_{z,\omega}^0(d_i) G_{z,-\omega}^0(d_j) d\omega \\ &= \int_{S^2} \int_{s_0(d_i, \omega)}^0 \delta(d_i + s\omega - z) e^{-\int_s^0 \mu(d_i + s'\omega, E_0) ds'} ds \\ &\quad \times \int_{t_0(d_j, -\omega)}^0 \delta(d_j - t\omega - z) e^{-\int_t^0 \mu(d_j - t'\omega, E_0) dt'} dt d\omega. \end{aligned}$$

Introducing the new coordinates  $p = s\omega$  we have  $\omega = -p/|p|$  and  $d\omega ds = dp/|p|^2$  leading to

$$\begin{aligned}
 G_z^0(d_i, d_j) &= \int_{S^2} \int_{s_0(d_i, \omega)}^0 \int_{t_0(d_j, -\omega)}^0 \delta(d_i + s\omega - z) \delta(d_j - t\omega - z) \\
 &\quad \times e^{-\int_s^0 \mu(d_i + s'\omega, E_0) ds'} e^{-\int_t^0 \mu(d_j - t'\omega, E_0) dt'} dt ds d\omega \\
 &= \int_{B_{|s_0(d_i, \omega)|}(0)} \int_{t_0(d_j, \frac{p}{|p|})}^0 \delta(d_i + p - z) \delta\left(d_j + t\frac{p}{|p|} - z\right) \\
 &\quad \times e^{-\int_{-|p|}^0 \mu\left(d_i - s'\frac{p}{|p|}, E_0\right) ds'} e^{-\int_t^0 \mu\left(d_j + t'\frac{p}{|p|}, E_0\right) dt'} \frac{dp}{|p|^2} dt \\
 &= \int_{t_0\left(d_j, \frac{z-d_i}{|z-d_i|}\right)}^0 \frac{\delta(P(z))}{|z-d_i|^2} e^{-\int_{-|z-d_i|}^0 \mu\left(d_i - s'\frac{z-d_i}{|z-d_i|}, E_0\right) ds'} \\
 &\quad \times e^{-\int_t^0 \mu\left(d_j + t'\frac{z-d_i}{|z-d_i|}, E_0\right) dt'} dt \\
 &= \int_{t_0\left(d_j, \frac{z-d_i}{|z-d_i|}\right)}^0 \frac{\delta(P(z))}{|z-d_i|^2} e^{-\int_{d_i}^z \mu(s, E_0) ds - \int_{d_j + t\frac{z-d_i}{|z-d_i|}^{d_j} \mu(s, E_0) ds} dt
 \end{aligned}$$

with a function  $P$  depending only on  $z$  defined by

$$P(z) = d_j + t \frac{z - d_i}{|z - d_i|} - z.$$

In order to analyze  $\delta(P(z))$  we have to find all  $z$  with  $P(z) = 0$ :

$$\begin{aligned}
 0 &= d_j + t \frac{z - d_i}{|z - d_i|} - z & (2.22) \\
 \Leftrightarrow z - \frac{tz}{|z - d_i|} &= d_j - \frac{td_i}{|z - d_i|} \\
 \Leftrightarrow z \left( \frac{|z - d_i| - t}{|z - d_i|} \right) &= \frac{d_j |z - d_i| - td_i}{|z - d_i|} \\
 \Leftrightarrow z &= \frac{d_j |z - d_i| - td_i}{|z - d_i| - t},
 \end{aligned}$$

i.e.  $z$  is on the straight line between the two detectors  $d_i$  and  $d_j$ , which is obvious because we cannot measure particles in this case, if  $z$  is not on the straight line between  $d_i$  and  $d_j$ .

Hence we can solve (2.22) for  $t$  and we have

$$\begin{aligned}
 0 &= d_j + t \frac{z - d_i}{|z - d_i|} - z \\
 \Leftrightarrow (z - d_j) |z - d_i| &= t (z - d_i) \\
 \Leftrightarrow (z - d_j) |z - d_i| &= -t |z - d_i| \frac{z - d_j}{|z - d_j|} \\
 \Leftrightarrow \frac{z - d_j}{-t} &= \frac{z - d_j}{|z - d_j|} \\
 \Rightarrow -t &= |z - d_j|,
 \end{aligned}$$

leading to  $|d_i - d_j| = |d_i - z| + |d_j - z| = |d_i - z| - t$ . Now we know that  $P(z) = 0$  if and only if

$$z = \frac{d_j (|d_i - d_j| + t) - t d_i}{|d_i - d_j|}.$$

Before we can apply

$$\int_{\mathbb{R}^n} \delta(\phi(x)) \psi(x) dx = \int_{\{x \in \mathbb{R}^n : \phi(x) = 0\}} \frac{\psi(x)}{\left| \det \left( \frac{\partial \phi}{\partial x} \right) \right|} d\sigma(x) \quad (2.23)$$

with the corresponding surface measure  $\sigma$  (see [Nat03], p .79), we have to derive  $\det \left( \frac{\partial P}{\partial z} \right)$ . We start with the derivatives of  $P$  with respect to  $z$  and deduce that the ensuing calculation of  $\det \left( \frac{\partial P}{\partial z} \right)$  is very simple because of the special structure of  $\frac{\partial P}{\partial z}$ .

$$\begin{aligned}
 \frac{\partial P}{\partial z} &= \left( \frac{t}{|z - d_i|} - 1 \right) I - \frac{t}{|z - d_i|^3} (z - d_i) (z - d_i)^T \\
 &= \left( \frac{t - |z - d_i|}{|z - d_i|} \right) I + \frac{|d_j - z|}{|z - d_i|^3} (z - d_i) (z - d_i)^T \\
 &= \left( \frac{-|d_i - d_j|}{|z - d_i|} \right) I + \frac{|d_j - z|}{|z - d_i|^3} (z - d_i) (z - d_i)^T \\
 &= \frac{-|d_i - d_j|}{|z - d_i|} \left( I - \frac{|d_j - z|}{|z - d_i|^2 |d_i - d_j|} (z - d_i) (z - d_i)^T \right) \\
 &= \frac{-|d_i - d_j|}{|z - d_i|} \left( I - \underbrace{\sqrt{\frac{|d_j - z|}{|z - d_i|^2 |d_i - d_j|}}}_{=: v} (z - d_i) \right. \\
 &\quad \left. \cdot \underbrace{\sqrt{\frac{|d_j - z|}{|z - d_i|^2 |d_i - d_j|}}}_{=: v^T} (z - d_i)^T \right) \\
 &= \frac{-|d_i - d_j|}{|z - d_i|} (I - vv^T). \quad (2.24)
 \end{aligned}$$

As an immediate consequence of (2.24) and the formula  $\det(I - vv^T) = 1 - |v|^2$ ,  $v \in \mathbb{R}^n$  (see [Nat86], p. 188), we have the following simple representation of  $\det\left(\frac{\partial P}{\partial z}\right)$ .

$$\begin{aligned}
 \left| \det\left(\frac{\partial P}{\partial z}\right) \right| &= \left| \left( \frac{-|d_i - d_j|}{|z - d_i|} \right)^3 \left( 1 - \left| \sqrt{\frac{|d_j - z|}{|z - d_i|^2 |d_i - d_j|}} (z - d_i) \right|^2 \right) \right| \\
 &= \left| \left( \frac{|d_i - d_j|}{|z - d_i|} \right)^3 \left( 1 - \frac{|d_j - z| |z - d_i|^2}{|z - d_i|^2 |d_i - d_j|} \right) \right| \\
 &= \left| \left( \frac{|d_i - d_j|}{|z - d_i|} \right)^3 \left( \frac{|d_i - d_j| - |d_j - z|}{|d_i - d_j|} \right) \right| \\
 &= \left| \left( \frac{|d_i - d_j|}{|z - d_i|} \right)^3 \left( \frac{|z - d_i|}{|d_i - d_j|} \right) \right| \\
 &= \left( \frac{|d_i - d_j|}{|z - d_i|} \right)^2.
 \end{aligned}$$

Collecting all terms and using (2.23) we obtain

$$\begin{aligned}
 M_{i,j} &= Mf(d_i, d_j) \\
 &= \int_C G_z^0(d_i, d_j) f(z) dz \\
 &= \int_C \int_{t_0\left(d_j, \frac{z-d_i}{|z-d_i|}\right)}^0 \frac{\delta(P(z))}{|z - d_i|^2} e^{-\int_{d_i}^z \mu(s, E_0) ds - \int_{d_j+t\frac{z-d_i}{|z-d_i|}}^{d_j} \mu(s, E_0) ds} f(z) dt dz \\
 &= \frac{e^{-\int_{d_j}^{d_i} \mu(s, E_0) ds}}{|d_i - d_j|^2} \int_{t_0\left(d_j, \frac{z-d_i}{|z-d_i|}\right)}^0 f\left(\frac{d_j(|d_i - d_j| + t) - td_i}{|d_i - d_j|}\right) dt \quad (2.25)
 \end{aligned}$$

Since we know that  $z$  is on the straight line between the two detectors we may write

$$\begin{aligned}
 \frac{d_j(|d_i - d_j| + t) - td_i}{|d_i - d_j|} &= d_j + t \frac{d_j - d_i}{|d_j - d_i|} \\
 &= d_j + t \frac{z - d_i}{|z - d_i|},
 \end{aligned}$$

which simplifies the integral in (2.25) to the integral between  $d_i$  and  $d_j$  because of the special choice of  $t_0$ . Finally we have

$$M_{i,j} = Mf(d_i, d_j) = \frac{e^{-\int_{d_j}^{d_i} \mu(s, E_0) ds}}{|d_i - d_j|^2} \int_{d_j}^{d_i} f dt, \quad (2.26)$$

which is the classical line model for PET scaled by the distance of the two detectors.  $\square$

### 2.2.2 The Case of Full Scatter

In this section we will no longer neglect scatter, and compute  $G_z(d_i, d_j)$  for the full model. Because scattering of particles is now allowed,  $G_z(d_i, d_j)$  maybe nonzero even if  $z$  is not on the straight line between  $d_i$  and  $d_j$ . As in the case without scatter we use  $q(x, \Theta) = \delta(x - z) \delta(\Theta - \omega)$  as source term. Hence the transport equation (2.2) reads

$$\begin{aligned} \theta \cdot \nabla_x u(x, \Theta, E) + \mu(x, E) u(x, \Theta, E) &= \int_{S^2} \int_E^{E_0} k(x, \Theta, \Theta', E, E') u(x, \Theta', E') dE' d\Theta' \\ &+ \delta(E - E_0) \delta(x - z) \delta(\Theta - \omega). \end{aligned} \quad (2.27)$$

From section 2.1 we know that the solution of (2.27) vanishing on  $\Gamma_\Theta$  for  $x = d_i$ , i.e. at the detector  $d_i$ , is given by

$$\begin{aligned} u_{z, \omega}(d_i, \Theta, E) &= \int_{s_0(d_i, \Theta)}^0 \left( \int_{S^2} \int_E^{E_0} k(d_i + s\Theta, \Theta, \Theta', E, E') u_{z, \omega}(d_i + s\Theta, \Theta', E') dE' d\Theta' \right. \\ &\quad \left. + \delta(d_i + s\Theta - z) \delta(\Theta - \omega) \delta(E - E_0) \right) e^{-\int_s^0 \mu(d_i + s'\Theta, E) ds'} ds \\ &= \int_{s_0(d_i, \Theta)}^0 \int_{S^2} \int_E^{E_0} k(d_i + s\Theta, \Theta, \Theta', E, E') u_{z, \omega}(d_i + s\Theta, \Theta', E') dE' d\Theta' \\ &\quad \times e^{-\int_s^0 \mu(d_i + s'\Theta, E) ds'} ds \\ &\quad + \underbrace{\int_{t_0(d_i, \Theta)}^0 \delta(d_i + t\Theta - z) e^{-\int_t^0 \mu(d_i + s'\Theta, E) ds'} dt \delta(\Theta - \omega) \delta(E - E_0)}_{= G_{z, \omega}^0(d_i, \Theta, E)} \\ &= \int_{s_0(d_i, \Theta)}^0 \int_{S^2} \int_E^{E_0} k(d_i + s\Theta, \Theta, \Theta', E, E') u_{z, \omega}(d_i + s\Theta, \Theta', E') dE' d\Theta' \\ &\quad \times e^{-\int_s^0 \mu(d_i + s'\Theta, E) ds'} ds + G_{z, \omega}^0(d_i, \Theta, E). \end{aligned} \quad (2.28)$$

Since there is still  $u_{z, \omega}$  on the right side and therefore not an explicit solution, (2.28) is just an integral representation of the transport equation. To simplify the notation, we introduce the scatter operator  $K$

$$Ku(x, \Theta, E) = \int_{S^2} \int_E^{E_0} k(x, \Theta, \Theta', E, E') u(x, \Theta', E') dE' d\Theta'.$$

Again we have to integrate over all possible detection directions  $\Theta$  and all energy levels  $E$  to model the detection process in detector  $d_i$

$$\begin{aligned}
 G_{z,\omega}(d_i) &= \int_{S^2} \int_{E_{\min}}^{E_0} u_{z,\omega}(d_i, \Theta, E) d\Theta dE \\
 &= \underbrace{\int_{S^2} \int_{E_{\min}}^{E_0} \int_{s_0(d_i, \Theta)}^0 K u_{z,\omega}(d_i + s\Theta, \Theta, E) e^{-\int_s^0 \mu(d_i + s'\Theta, E) ds'} ds dE d\Theta}_{=: G_{z,\omega}^S(d_i)} \\
 &\quad + \underbrace{\int_{S^2} \int_{E_{\min}}^{E_0} G_{z,\omega}^0(d_i, \Theta, E) dE d\Theta}_{=: G_{z,\omega}^0(d_i)} \\
 &= G_{z,\omega}^S(d_i) + G_{z,\omega}^0(d_i),
 \end{aligned}$$

where only  $G_{z,\omega}^S(d_i)$  contains information about scattered particles. Finally  $G_z(d_i, d_j)$  is given by

$$\begin{aligned}
 G_z(d_i, d_j) &= \int_{S^2} G_{z,\omega}(d_i) G_{z,-\omega}(d_j) d\omega \\
 &= \int_{S^2} (G_{z,\omega}^0(d_i) + G_{z,\omega}^S(d_i)) (G_{z,-\omega}^0(d_j) + G_{z,-\omega}^S(d_j)) d\omega \\
 &= \int_{S^2} G_{z,\omega}^0(d_i) G_{z,-\omega}^0(d_j) d\omega + \int_{S^2} G_{z,\omega}^0(d_i) G_{z,-\omega}^S(d_j) d\omega \\
 &\quad + \int_{S^2} G_{z,-\omega}^0(d_j) G_{z,\omega}^S(d_i) d\omega + \int_{S^2} G_{z,\omega}^S(d_i) G_{z,-\omega}^S(d_j) d\omega.
 \end{aligned}$$

Here we can clearly see the connection between the models of Watson (1.20), Markiewicz (1.23) and the new model. We mention that both authors usually regard only scatter of one photon, i.e. the second and the third term, while we prefer to work with scatter of both photons, too. Regarding (2.13) this representation of our PET model is not unexpected since it contains the four possible cases of particle movement described in the introduction of this section.

In section 2.2.1 we presented a detailed derivation of the first term containing the unscattered part. Now we will analyze the remaining terms to obtain a detailed description of  $G_z(d_i, d_j)$ . Due to symmetry the second and the third term have the same structure so we only deal with the second one.

We start with

$$\begin{aligned}
 \int_{S^2} G_{z,\omega}^0(d_i) G_{z,-\omega}^S(d_j) d\omega &= \int_{S^2} \int_{t_0(d_i,\omega)}^0 \delta(d_i + t\omega - z) e^{-\int_t^0 \mu(d_i + s'\omega, E_0) ds'} dt \\
 &\times \int_{S^2} \int_{E_{\min}}^{E_0} \int_{s_0(d_j,\Theta)}^0 K u_{z,-\omega}(d_j + s\Theta, \Theta, E) \\
 &\times e^{-\int_s^0 \mu(d_j + s'\Theta, E) ds'} ds dE d\Theta d\omega.
 \end{aligned}$$

Introducing the function  $V(p) = d_i + p - z$  and the new coordinate  $p = t\omega$  we have  $\omega = -p/|p|$  and  $d\omega dt = dp/|p|^2$  and therefore

$$\begin{aligned}
 \int_{S^2} G_{z,\omega}^0(d_i) G_{z,-\omega}^S(d_j) d\omega &= \int_{B_{|t_0(d_i,\omega)|}(0)} \frac{\delta(V(p)) e^{-\int_{-|p|}^0 \mu(d_i - s' \frac{p}{|p|}, E_0) ds'}}{|p|^2} \\
 &\times \int_{S^2} \int_{E_{\min}}^{E_0} \int_{s_0(d_j,\Theta)}^0 K u_{z, \frac{p}{|p|}}(d_j + s\Theta, \Theta, E) \\
 &\times e^{-\int_s^0 \mu(d_j + s'\Theta, E) ds'} ds dE d\Theta dp.
 \end{aligned}$$

For  $p = z - d_i$  we have  $V(p) = 0$  and can reduce the equation to

$$\begin{aligned}
 \int_{S^2} G_{z,\omega}^0(d_i) G_{z,-\omega}^S(d_j) d\omega &= \frac{e^{-\int_{-|z-d_i|}^0 \mu(d_i - s' \frac{z-d_i}{|z-d_i|}, E_0) ds'}}{|z-d_i|^2} \\
 &\times \int_{S^2} \int_{E_{\min}}^{E_0} \int_{s_0(d_j,\Theta)}^0 K u_{z, \frac{z-d_i}{|z-d_i|}}(d_j + s\Theta, \Theta, E) \\
 &\times e^{-\int_s^0 \mu(d_j + s'\Theta, E) ds'} ds dE d\Theta \\
 &= \int_{S^2} \int_{E_{\min}}^{E_0} \int_{s_0(d_j,\Theta)}^0 K u_{z, \frac{z-d_i}{|z-d_i|}}(d_j + s\Theta, \Theta, E) \\
 &\times \frac{e^{-\int_z^{d_i} \mu(t, E_0) dt} e^{-\int_s^0 \mu(d_j + s'\Theta, E) ds'}}{|z-d_i|^2} ds dE d\Theta.
 \end{aligned}$$

The fourth term containing scatter in both directions cannot be simplified and we have the following Theorem by combining all derived results.

**Theorem 2.2.2** *In the case of full scatter the new model containing the probability  $G_z(d_i, d_j)$  that two particles are emitted somewhere in  $C$  and detected by the two detectors  $d_i$  and  $d_j$  can be written as*

$$\begin{aligned}
 M_{i,j} &= Mf(d_i, d_j) = \int_C G_z(d_i, d_j) f(z) dz \\
 &= \frac{e^{-\int_{d_j}^{d_i} \mu(s, E_0) ds}}{|d_i - d_j|^2} \int_{d_j}^{d_i} f dt \\
 &\quad + \int_C \int_{S^2} \int_{E_{\min}}^{E_0} \int_{s_0(d_j, \Theta)}^0 K u_{z, \frac{z-d_i}{|z-d_i|}}(d_j + s\Theta, \Theta, E) \\
 &\quad \times \frac{e^{-\int_z^{d_i} \mu(t, E_0) dt} e^{-\int_s^0 \mu(d_j + s'\Theta, E) ds'}}{|z - d_i|^2} ds dE d\Theta f(z) dz \\
 &\quad + \int_C \int_{S^2} \int_{E_{\min}}^{E_0} \int_{s_0(d_i, \Theta)}^0 K u_{z, \frac{z-d_j}{|z-d_j|}}(d_i + s\Theta, \Theta, E) \\
 &\quad \times \frac{e^{-\int_z^{d_j} \mu(t, E_0) dt} e^{-\int_s^0 \mu(d_i + s'\Theta, E) ds'}}{|z - d_j|^2} ds dE d\Theta f(z) dz \\
 &\quad + \int_C \int_{S^2} G_{z, \omega}^S(d_i) G_{z, -\omega}^S(d_j) d\omega f(z) dz. \tag{2.29}
 \end{aligned}$$

In real world applications the case of full scatter can hardly be analyzed due to the high amount of necessary computations. As an example, we consider the Siemens Biograph Sensation 16 which will be used for numerical tests in chapter 4 as well. Imagine a grid of  $175 \times 175 \times 47$  and 384 detectors. Then we have to compute  $G_z(d_i, d_j)$  more than  $2 \cdot 10^{11}$  times whereas each computation relies on a complicated multiple integral. A simple approach to simplify the problem is presented in the next section where only single scatter is considered.

### 2.2.3 The Single Scatter Approximation

To reduce the complexity of the presented problem we introduce a simple approximation. The idea is to replace the unknown function  $u_{z,\omega}(x, \Theta, E)$  on the right hand side of (2.28) by the known function  $G_{z,\omega}^0(x, \Theta, E)$  to simplify the equation. Since  $G_{z,\omega}^0(x, \Theta, E)$  is the solution of the Boltzmann equation with  $k = 0$  a single particle may only be scattered once before it reaches the detector. This simplification is reasonable as it has been shown that single scatter is the dominating effect in degrading the image quality. To simplify notation we will write  $\omega_i$  instead of  $\frac{z-d_i}{|z-d_i|}$ . By inserting  $G_{z,\omega}^0(x, \Theta, E)$  we have

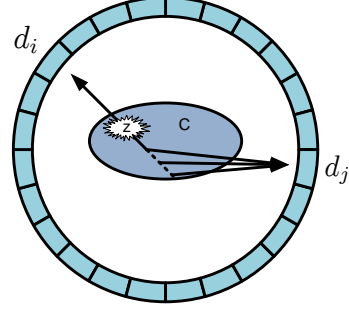


Figure 2.2: Two particles emitted in  $z \in C$ : one photon reaches  $d_i \in \Gamma$  unscattered whereas the other one is scattered in direction  $\frac{d_j - (z - t\omega_i)}{|d_j - (z - t\omega_i)|}$  before it arrives at  $d_j \in \Gamma$ .

$$\begin{aligned}
 & \int_{S^2} G_{z,\omega}^0(d_i) G_{z,-\omega}^S(d_j) d\omega \tag{2.30} \\
 = & \int_{S^2} \int_{E_{\min}}^{E_0} \int_{s_0(d_j, \Theta)}^0 K u_{z,\omega_i}(d_j + s\Theta, \Theta, E) \frac{e^{-\int_z^{d_i} \mu(t', E_0) dt'} e^{-\int_s^0 \mu(d_j + s'\Theta, E) ds'}}{|z - d_i|^2} ds dE d\Theta \\
 = & \int_{S^2} \int_{E_{\min}}^{E_0} \int_{s_0(d_j, \Theta)}^0 \int_{S^2} \int_E^{E_0} k(d_j + s\Theta, \Theta, \Theta', E, E') u_{z,\omega_i}(d_j + s\Theta, \Theta', E') dE' d\Theta' \\
 & \times \frac{e^{-\int_z^{d_i} \mu(t', E_0) dt'} e^{-\int_s^0 \mu(d_j + s'\Theta, E) ds'}}{|z - d_i|^2} ds dE d\Theta \\
 \stackrel{(2.21)}{=} & \int_{S^2} \int_{E_{\min}}^{E_0} \int_{s_0(d_j, \Theta)}^0 \int_{S^2} \int_E^{E_0} k(d_j + s\Theta, \Theta, \Theta', E, E') \int_{t_0(d_j + s\Theta, \Theta')}^0 \delta(d_j + s\Theta + t\Theta' - z) \\
 & \times \delta(E' - E_0) \delta(\Theta' - \omega_i) e^{-\int_t^0 \mu(d_j + s\Theta + s'\Theta', E') ds'} dt dE' d\Theta' \\
 & \times e^{-\int_s^0 \mu(d_j + s'\Theta, E) ds'} ds dE d\Theta \frac{e^{-\int_z^{d_i} \mu(t', E_0) dt'}}{|z - d_i|^2} \\
 = & \int_{S^2} \int_{E_{\min}}^{E_0} \int_{s_0(d_j, \Theta)}^0 k(d_j + s\Theta, \Theta, \omega_i, E, E_0) \int_{t_0(d_j + s\Theta, \omega_i)}^0 \delta(d_j + s\Theta + t\omega_i - z) \\
 & \times e^{-\int_t^0 \mu(d_j + s\Theta + s'\omega_i, E_0) ds'} dt e^{-\int_s^0 \mu(d_j + s'\Theta, E) ds'} ds dE d\Theta \frac{e^{-\int_z^{d_i} \mu(t', E_0) dt'}}{|z - d_i|^2}.
 \end{aligned}$$

Again we introduce the new coordinate  $p = s\Theta$  with  $\Theta = -p/|p|$  and a function  $V(p) = d_j + p + tw_i - z$  to evaluate  $\delta$  with respect to  $p$ . It is obvious that  $V(p)$  is zero if  $p = -d_j + z - tw_i$ . This leads to a simplified version of (2.30).

$$\begin{aligned}
 & \int_{S^2} G_{z,\omega}^0(d_i) G_{z,-\omega}^S(d_j) d\omega \\
 = & \int_{E_{\min}}^{E_0} \int_{t_0(d_j+p,\omega_i)}^0 \int_{B_{|s_0(d_j,-\frac{p}{|p|})|}^{(0)}} k\left(d_j + p, -\frac{p}{|p|}, w_i, E, E_0\right) \delta(V(p)) \\
 & \times \frac{e^{-\int_t^0 \mu(d_j+p+s'w_i, E_0) ds'} e^{-\int_{-|p|}^0 \mu(d_j-s'\frac{p}{|p|}, E) ds'} e^{-\int_z^{d_i} \mu(t', E_0) dt'}}{|p|^2 |z - d_i|^2} dp dt dE \\
 = & \int_{E_{\min}}^{E_0} \int_{t_0(z,\omega_i)}^0 k\left(z - tw_i, \frac{d_j - (z - tw_i)}{|d_j - (z - tw_i)|}, w_i, E, E_0\right) \\
 & \times \frac{e^{-\int_t^0 \mu(z-tw_i+s'w_i, E_0) ds'} e^{-\int_{-|d_j-z+tw_i|}^0 \mu\left(d_j+s'\frac{d_j-(z-tw_i)}{|d_j-(z-tw_i)|}, E\right) ds'}}{|d_j - (z - tw_i)|^2} dt dE \\
 & \times \frac{e^{-\int_z^{d_i} \mu(t', E_0) dt'}}{|z - d_i|^2} \\
 = & \int_{E_{\min}}^{E_0} \int_{t_0(z,\omega_i)}^0 k\left(z - tw_i, \frac{d_j - (z - tw_i)}{|d_j - (z - tw_i)|}, w_i, E, E_0\right) \\
 & \times \frac{e^{-\int_z^{d_i} \mu(t', E_0) dt'} e^{-\int_{z-tw_i}^z \mu(s', E_0) ds'} e^{-\int_{d_j}^{z-tw_i} \mu(s', E) ds'}}{|z - d_i|^2 |d_j - (z - tw_i)|^2} dt dE.
 \end{aligned}$$

Now we can easily interpret (2.30): At a fixed point  $z \in C$  two particles are emitted in directions  $\pm\omega_i$  at  $E_0 = 511$  keV. The particle travelling to  $d_i$  reaches the detector unscattered at 511 keV while the particle travelling in the opposite direction may undergo a scattering process. Starting at  $z$  we have to calculate for each point on  $z - tw_i$  the fraction that is scattered in direction of detector  $d_j$ . We also have to consider for the loss due to attenuation by tissue, which is included in the two exponentials. The new energy level  $E$  after the scatter process can be calculated using (1.12). Analog computations can of course be done for the case of single scatter in the opposite direction.

Using the same ideas as above we can also give a simpler representation for the fourth term. Starting with the definition of  $G_{z,\omega}^S(d_i)$  and replacing the unknown  $u_{z,\omega}$  by (2.21)

we have

$$\begin{aligned}
 G_{z,\omega}^S(d_i) &= \int_{S^2} \int_{E_{\min}}^{E_0} \int_{s_0(d_i,\Theta)}^0 K u_{z,\omega}(d_i + s\Theta, \Theta, E) e^{-\int_s^0 \mu(d_i + s'\Theta, E) ds'} ds dE d\Theta \\
 &= \int_{S^2} \int_{E_{\min}}^{E_0} \int_{s_0(d_i,\Theta)}^0 \int_{S^2} \int_E^{E_0} k(d_i + s\Theta, \Theta, \Theta', E, E') \\
 &\quad \times u_{z,\omega}(d_i + s\Theta, \Theta', E') dE' d\Theta' e^{-\int_s^0 \mu(d_i + s'\Theta, E) ds'} ds dE d\Theta \\
 &\stackrel{(2.21)}{=} \int_{S^2} \int_{E_{\min}}^{E_0} \int_{s_0(d_i,\Theta)}^0 \int_{S^2} \int_E^{E_0} k(d_i + s\Theta, \Theta, \Theta', E, E') \int_{t_0(d_i + s\Theta, \Theta')}^0 \delta(E' - E_0) \\
 &\quad \times \delta(d_i + s\Theta + t\Theta' - z) \delta(\Theta' - \omega) \\
 &\quad \times e^{-\int_t^0 \mu(d_i + s\Theta + t'\Theta', E') dt'} dt dE' d\Theta' e^{-\int_s^0 \mu(d_i + s'\Theta, E) ds'} ds dE d\Theta \\
 &= \int_{S^2} \int_{E_{\min}}^{E_0} \int_{s_0(d_i,\Theta)}^0 \int_{t_0(d_i + s\Theta, \Theta')}^0 k(d_i + s\Theta, \Theta, \omega, E, E_0) \delta(d_i + s\Theta + t\omega - z) \\
 &\quad \times e^{-\int_t^0 \mu(d_i + s\Theta + t'\omega, E_0) dt'} e^{-\int_s^0 \mu(d_i + s'\Theta, E) ds'} dt ds dE d\Theta.
 \end{aligned}$$

Finally we introduce the coordinates  $p = s\Theta$  with  $\Theta = -p/|p|$  and a function  $V(p) = d_i + p + t\omega - z$  leading to

$$\begin{aligned}
 G_{z,\omega}^S(d_i) &= \int_{E_{\min}}^{E_0} \int_{B_{|s_0(d_i,\Theta)|}(0)} \int_{t_0(d_i + p, \omega)}^0 k\left(d_i + p, -\frac{p}{|p|}, \omega, E, E_0\right) \delta(d_i + p + t\omega - z) \\
 &\quad \times \frac{e^{-\int_t^0 \mu(d_i + p + t'\omega, E_0) dt'} e^{-\int_{-|p|}^0 a(d_i - s'\frac{p}{|p|}, E) ds'}}{|p|^2} dt dp dE \\
 &= \int_{E_{\min}}^{E_0} \int_{B_{|s_0(d_i,\Theta)|}(0)} \int_{t_0(d_i + p, \omega)}^0 k\left(d_i + p, -\frac{p}{|p|}, \omega, E, E_0\right) \delta(V(p)) \\
 &\quad \times \frac{e^{-\int_{d_i + p + t\omega}^{d_i + p} \mu(t', E_0) dt'} e^{-\int_{d_i}^{d_i + p} \mu(s', E) ds'}}{|p|^2} dt dp dE \\
 &= \int_{E_{\min}}^{E_0} \int_{t_0(z, \omega)}^0 k\left(z - t\omega, \frac{d_i - z + t\omega}{|d_i - z + t\omega|}, \omega, E, E_0\right) \\
 &\quad \times \frac{e^{-\int_z^{z - t\omega} \mu(t', E_0) dt'} e^{-\int_{z - t\omega}^{d_i} \mu(t', E) dt'}}{|d_i - z + t\omega|^2} dt dE.
 \end{aligned}$$

Combining all results leads to the following theorem.

**Theorem 2.2.3** *In the case of single scatter the new model containing the probability  $G_z(d_i, d_j)$  that two particles are emitted somewhere in  $C$  and detected by the two detectors  $d_i$  and  $d_j$  can be written as*

$$\begin{aligned}
 M_{i,j} &= Mf(d_i, d_j) = \int_C G_z(d_i, d_j) f(z) dz \\
 &= \frac{e^{-\int_{d_j}^{d_i} \mu(s, E_0) ds}}{|d_i - d_j|^2} \int_{d_j}^{d_i} f dt \\
 &\quad + \int_C \int_{E_{\min}}^{E_0} \int_{t_0(z, \omega_i)}^0 k \left( z - t\omega_i, \frac{d_j - z + t\omega_i}{|d_j - z + t\omega_i|}, \omega_i, E, E_0 \right) \\
 &\quad \times \frac{e^{-\int_{d_i}^{z-t\omega_i} \mu(s', E_0) ds'} e^{-\int_{z-t\omega_i}^{d_j} \mu(s', E) ds'}}{|z - d_i|^2 |d_j - z + t\omega_i|^2} dt dE f(z) dz \\
 &\quad + \int_C \int_{E_{\min}}^{E_0} \int_{t_0(z, \omega_j)}^0 k \left( z - t\omega_j, \frac{d_i - z + t\omega_j}{|d_i - z + t\omega_j|}, \omega_j, E, E_0 \right) \\
 &\quad \times \frac{e^{-\int_{d_j}^{z-t\omega_j} \mu(s', E_0) ds'} e^{-\int_{z-t\omega_j}^{d_i} \mu(s', E) ds'}}{|z - d_j|^2 |d_i - z + t\omega_j|^2} dt dE f(z) dz \\
 &\quad + \int_C \int_{S^2} \int_{E_{\min}}^{E_0} \int_{t_0(z, \omega)}^0 k \left( z - t\omega, \frac{d_i - z + t\omega}{|d_i - z + t\omega|}, \omega, E, E_0 \right) \\
 &\quad \times \frac{e^{-\int_z^{z-t\omega} \mu(t', E_0) dt'} e^{-\int_{z-t\omega}^{d_i} \mu(t', E) dt'}}{|d_i - z + t\omega|^2} dt dE \\
 &\quad \times \int_{E_{\min}}^{E_0} \int_{t_0(z, -\omega)}^0 k \left( z + t\omega, \frac{d_j - z - t\omega}{|d_j - z - t\omega|}, -\omega, E, E_0 \right) \\
 &\quad \times \frac{e^{-\int_z^{z+t\omega} \mu(t', E_0) dt'} e^{-\int_{z+t\omega}^{d_j} \mu(t', E) dt'}}{|d_j - z - t\omega|^2} dt dE d\omega f(z) dz,
 \end{aligned} \tag{2.31}$$

where we denote  $\omega_i = (z - d_i) / |z - d_i|$  and  $\omega_j = (z - d_j) / |z - d_j|$ .

Once  $G_z(d_i, d_j)$  is calculated for all combinations of source points / detectors we can solve (2.31) for  $f$  using any linear solver. Depending on the granularity of the grid this model should nearly be as precise as full Monte Carlo simulations. However, this would also lead to a similar computation time.

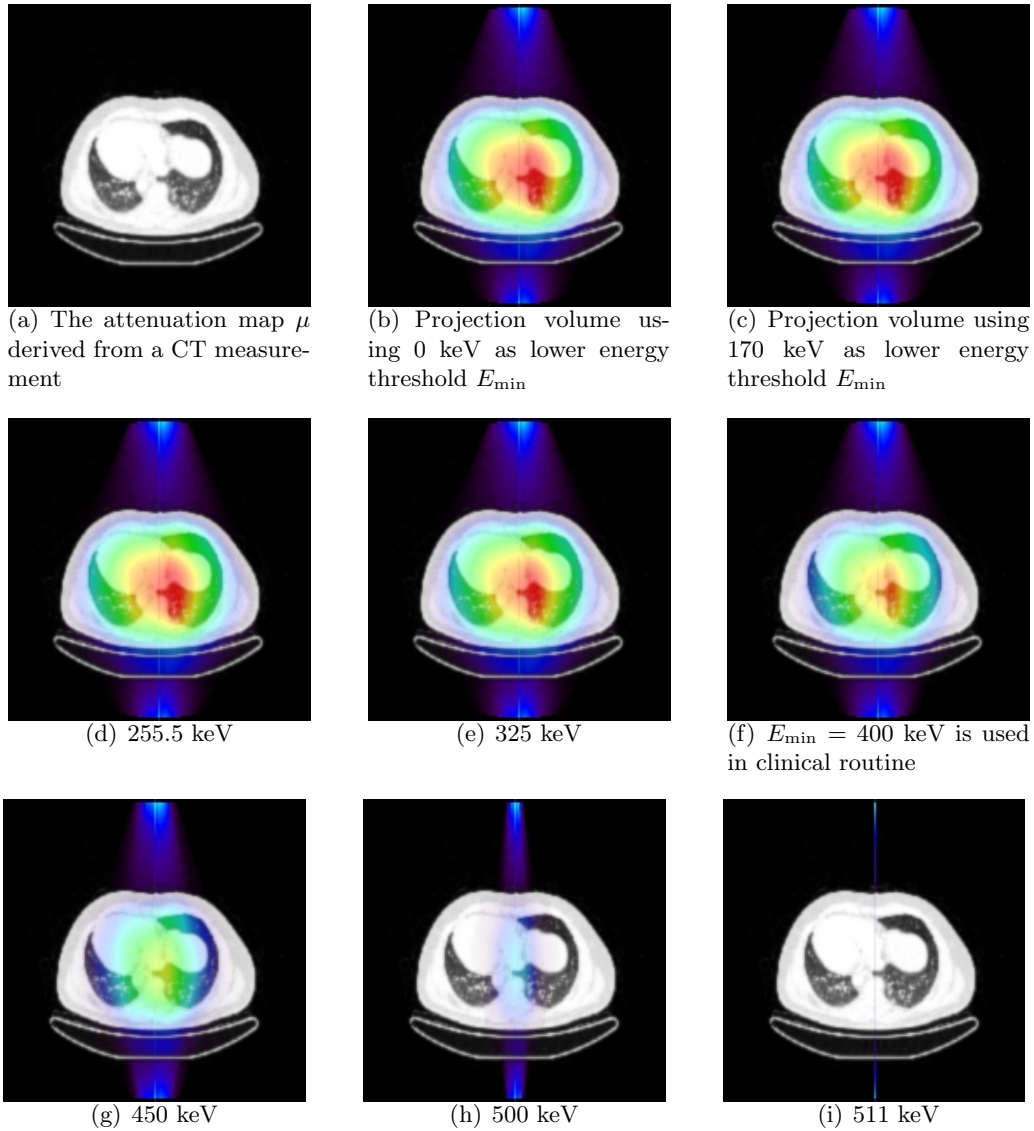


Figure 2.3: Example of the projection volume when using the new scatter model in case of single scatter for the Siemens Biograph Sensation 16. The attenuation coefficients were acquired at the Department of Nuclear Medicine, University Hospital of Münster. All volumes were calculated for the same LOR using different energy thresholds. There is no difference between 0 keV and 170 keV, since the minimum remaining energy after single scattering is equal to 170.3 keV (see figure 1.8). In case of  $E_{\min} = 255$  keV there is still no big difference. When increasing  $E_{\min}$  to larger values, the projection volume is more and more reduced to the scaled X-ray transform as can be seen in figure 2.3(i). We like to know how large the distortion can be, if we still want to treat the problem as a perturbation of the X-ray transform, i.e. is the X-ray transform generally the correct model for PET?

Instead of computing  $f$  at this point using (2.29) or (2.31) and a linear solver we like to further investigate the structure of  $M$ . On closer inspection  $M$  looks like the X-ray transform plus three additional operators: Is it possible to use the knowledge of the X-ray transform and its inverse operator to derive  $f$  analytically from the measurements? How large is the impact of the three other operators? In the next chapter we will treat  $M$  as a perturbation of the X-ray transform and try to compute  $f$  analytically from  $Mf$ .

## Chapter 3

# A Neumann Series Approach for Scatter Correction in PET

In chapter 2 we presented a detailed transport model for the full scattering process in PET based on the Boltzmann equation. As shown the resulting model consists of the X-ray transform and three additional operators containing information about scattered particles. We are now interested to learn how large the impact of these scatter operators is, i.e. can we treat our PET model more or less like the X-ray transform?

Recently, Bal and Tamasan [BT08] proposed a reconstruction algorithm based on a Neumann series approach for a similar transport problem in optical molecular imaging. The problem was analyzed as a perturbation of the attenuated Radon transform and it was shown that the resulting reconstruction algorithm converges if the scattering kernel is sufficiently small in an appropriate norm. By adopting this approach to our scatter model we show that the problem can be seen as a perturbation of the X-ray transform.

Hence, the main question of this chapter is: what are the necessary assumptions on the scattering kernel  $k$  to obtain a converging Neumann series and therefore a converging reconstruction algorithm? As we learned from chapter 1, attenuation in PET can be identified with Compton scatter and vice versa. Thus we might recast the question and search for the necessary assumptions on the attenuation map  $\mu$  in order to still reconstruct  $f$  using the inversion formula for the X-ray transform.

The second parameter to investigate is the minimum energy threshold  $E_{\min}$  that allows us to neglect particles with less energy during the measuring process. As mentioned before we might use  $E_{\min} = E_0$  and reject all particles with lower energy, but this would significantly reduce the statistics and furthermore we are not even able to set this threshold at 511 keV in real world applications due to the insufficient energy resolution of the system. Nevertheless we assume that we can define an arbitrary threshold and choose it according to the magnitude of  $\mu$ , i.e. we are searching for a combination  $(\mu, E_{\min})$  allowing us to measure as much particles as possible while regarding the necessary restrictions to use the Neumann series approach.

We give a detailed analysis of the single scatter case and deduce the case of multiple scatter afterwards.

At the end of this chapter we will see that we can find a threshold for all possible  $\mu$  to satisfy the smallness condition of the corresponding norm. Hence we conclude, that the X-ray transform is in general the correct model for PET.

### 3.1 Introducing the Neumann Series

From chapter 2 we know that the operator  $M$  describing the full decay-to-detection process for the sought-after activity distribution  $f$  on the cylinder  $C$  and a given dataset  $M_{i,j}$  has the following form

$$\begin{aligned}
 M_{i,j} &= Mf(d_i, d_j) \\
 &= \int_C G_z(d_i, d_j) f(z) dz \\
 &= \int_C \int_{S^2} G_{z,\omega}(d_i) G_{z,-\omega}(d_j) d\omega f(z) dz \\
 &= \int_C \int_{S^2} (G_{z,\omega}^0(d_i) + G_{z,\omega}^S(d_i)) (G_{z,-\omega}^0(d_j) + G_{z,-\omega}^S(d_j)) d\omega f(z) dz \\
 &= \int_C \int_{S^2} G_{z,\omega}^0(d_i) G_{z,-\omega}^0(d_j) d\omega f(z) dz \quad (\text{no scatter in both directions}) \\
 &\quad + \int_C \int_{S^2} G_{z,\omega}^0(d_i) G_{z,-\omega}^S(d_j) d\omega f(z) dz \quad (\text{scatter between } z \text{ and } d_j) \\
 &\quad + \int_C \int_{S^2} G_{z,-\omega}^0(d_j) G_{z,\omega}^S(d_i) d\omega f(z) dz \quad (\text{scatter between } z \text{ and } d_i) \\
 &\quad + \int_C \int_{S^2} G_{z,\omega}^S(d_i) G_{z,-\omega}^S(d_j) d\omega f(z) dz. \quad (\text{scatter in both directions})
 \end{aligned}$$

Again we assume that our data is already random corrected. Hence  $M_{i,j} = T_{i,j} + S_{i,j}$ . Considering (2.26) the unscattered part can be reduced to the X-ray transform  $P$  scaled by an attenuation coefficient and the distance of the two detectors  $d_i$  and  $d_j$

$$\int_C \int_{S^2} G_{z,\omega}^0(d_i) G_{z,-\omega}^0(d_j) d\omega f(z) dz = \underbrace{\frac{e^{-\int_{d_i}^{d_j} a(t, E_0) dt}}{|d_i - d_j|^2}}_{=: V(d_i, d_j)} \int_{d_i}^{d_j} f dt. \quad (3.1)$$

Inserting (3.1) into the equation above leads to

$$\begin{aligned}
 M_{i,j} &= V(d_i, d_j) \int_{d_i}^{d_j} f dt \\
 &\quad + \int_C \int_{S^2} G_{z,\omega}^0(d_i) G_{z,-\omega}^S(d_j) d\omega f(z) dz \\
 &\quad + \int_C \int_{S^2} G_{z,-\omega}^0(d_j) G_{z,\omega}^S(d_i) d\omega f(z) dz \\
 &\quad + \int_C \int_{S^2} G_{z,\omega}^S(d_i) G_{z,-\omega}^S(d_j) d\omega f(z) dz. \quad (3.2)
 \end{aligned}$$

We would like to see  $M$  as a perturbation of the X-ray transform  $P$ . In order to reconstruct  $f$  we will use a Neumann series approach. Provided the deviation of  $P$  is not too large, the series converges and can be used for the inversion. Our convergence analysis is based on the following lemma.

**Lemma 3.1.1** *Suppose that  $Q$  is a bounded operator on the normed space  $(X, \|\cdot\|)$  and*

$$\limsup_{m \rightarrow \infty} \|Q^m\|^{1/m} < 1,$$

(e.g.  $\|Q\| < 1$ ). Then  $(I - Q)$  is invertible, its inverse is continuous and equal to the series

$$(I - Q)^{-1} = \sum_{m=0}^{\infty} Q^m.$$

Proof: see, e.g. [Alt85].

Before we introduce the Neumann series we will study some properties of the X-ray transform  $P$ . For an infinitely differentiable function  $f$  with compact support  $P$  is defined as

$$Pf(\Theta, x) = \int_{\mathbb{R}^1} f(x + t\Theta) dt \quad (3.3)$$

on the tangent bundle

$$T = \left\{ (\Theta, x) : \theta \in S^{n-1}, x \in \Theta^\perp \right\}.$$

The restriction of  $x$  to  $\Theta^\perp$  and therefore the definition of  $P$  on  $T$  is obvious since  $Pf(\Theta, x)$  does not change if  $x$  is moved in direction  $\Theta$ . We still have the symmetry  $Pf(\Theta, x) = Pf(-\Theta, x)$ , but to simplify notation we nevertheless work with  $T$ .

Our approach is based on the assumption that we can reconstruct  $f$  from a perturbed version of  $Pf$ . Hence we first try to derive  $f$  from (3.3). Let  $g(\Theta, x) = Pf(\Theta, x)$  be the X-ray transform of  $f$  on  $T$ . We have the following explicit inversion formula for  $P$ .

**Theorem 3.1.2** *Let  $f \in C_0^\infty(\mathbb{R}^n)$ . Then we have for  $\alpha < n$*

$$f = \frac{1}{2\pi |S^{n-1}|} I^{-\alpha} P^* I^{\alpha-1} g, \quad (3.4)$$

with the Riesz potential  $I^\alpha$  defined as  $(I^\alpha \widehat{f})(\xi) = |\xi|^{-\alpha} \widehat{f}(\xi)$ . The adjoint operator  $P^*$  is given by

$$(P^*g)(x) = \int_{S^{n-1}} g(\Theta, E_\Theta x) d\Theta,$$

where  $E_\Theta x$  is the orthogonal projection of  $x$  on  $\Theta^\perp$ .

Proof: see, e.g. [Nat86].

We remark that  $I^{-\alpha}$  in (3.4) is the Riesz potential on  $\mathbb{R}^n$  while  $I^{\alpha-1}$  is the Riesz potential on  $T$  and therefore defined on the second variable only. A major drawback of (3.4) is the amount of data needed for the inversion. In the case  $n = 3$  and  $\alpha = 0$  the inversion formula reads

$$f = \frac{1}{(4\pi)^2} \int_{S^2} (I^{-1}g)(\Theta, E_\Theta x) d\Theta,$$

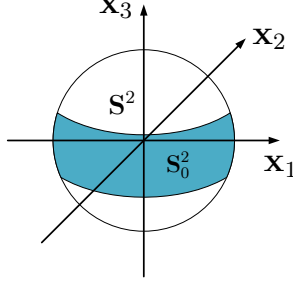


Figure 3.1: Example of a set  $S_0^2 \subset S^2$  satisfying Orlov's condition: Each equatorial circle has a non-empty intersection with  $S_0^2$ . Therefore measurements  $g(\Theta, x)$ ,  $x \in \Theta^\perp$ ,  $\Theta \in S_0^2$ , uniquely determine  $f$ .

i.e. we need  $g(\Theta, x)$  for all  $\Theta \in S^2$  and  $x \in \Theta^\perp$  to reconstruct  $f$ . Regarding our PET model of chapter 2 it is obvious that in case of  $n = 3$  this condition can never be satisfied by the measurements since we assume the scanner to be an open-ended cylinder. Thus we need a 3D inversion formula that uses less data but is still able to recover  $f$ . A possible solution might be to reduce the 3D problem into a set of 2D problems that can easily be solved with Theorem 3.4. Since we want to have a fully 3D reconstruction algorithm we will neglect this approach and study further properties of the X-Ray transform.

Following Orlov [Orl76] the sought-after function  $f$  is uniquely determined by the projections  $g(\Theta, x)$ ,  $\Theta \in S_0^2$ ,  $x \in \Theta^\perp$ , if the subset  $S_0^2 \subset S^2$  satisfies the following condition: *Any great circle on the unit sphere must have a non-empty intersection with the set  $S_0^2$ .* To clarify that we only use parts of the data we write  $T(S_0^2)$  instead of  $T$  for the tangent bundle. Orlov's condition is proved with the help of the *central section theorem* or *Fourier slice theorem*. It relates the Fourier transform of the projection  $Pf$  with the Fourier transform of  $f$ .

**Theorem 3.1.3** For  $f \in C_0^\infty(\mathbb{R}^n)$  we have

$$\widehat{Pf}(\Theta, \xi) = (2\pi)^{1/2} \widehat{f}(\xi), \quad \xi \in \Theta^\perp.$$

The Fourier transform on  $T$  is defined with respect to the second variable, i.e.

$$\widehat{h}(\Theta, \xi) = (2\pi)^{(1-n)/2} \int_{\Theta^\perp} e^{-ix \cdot \xi} h(\Theta, x) dx, \quad \xi \in \Theta^\perp.$$

Proof:

$$\begin{aligned} \widehat{Pf}(\Theta, \xi) &= (2\pi)^{(1-n)/2} \int_{\Theta^\perp} e^{-i\xi \cdot x} \int_{\mathbb{R}^1} f(x + t\Theta) dt dx \\ &= (2\pi)^{(1-n)/2} \int_{\mathbb{R}^n} e^{-i\xi \cdot y} f(y) dy \\ &= (2\pi)^{1/2} \widehat{f}(\xi). \end{aligned}$$

□

Now let  $Pf(\Theta, \cdot)$ ,  $\Theta \in S_0^2$ , be given and let  $S_0^2 \subset S^2$  satisfy Orlov's condition. Since  $S_0^2$  contains a great circle, it has at least two intersections with any plane through the

origin. Then for any frequency  $\xi \in \mathbb{R}^3$  we can find  $\Theta \in S_0^2$  such that  $\Theta \perp \xi$ . With help of Theorem 3.1.3  $\widehat{f}(\xi)$  is determined by  $\widehat{P}f(\Theta, \xi)$ .

Unfortunately we cannot derive  $f$  from the restricted data on  $S_0^2$  using Theorem 3.1.2; hence we need a new inversion formula. Let  $l(x, y)$  be the length of the intersection of  $S_0^2$  with the subspace spanned by  $x, y \in \mathbb{R}^3$ .

**Theorem 3.1.4** *Let  $f \in C_0^\infty(\mathbb{R}^n)$  and  $g(\Theta, x) = Pf(\Theta, x)$  for  $\Theta \in S_0^2$  and  $x \in \Theta^\perp$ . Then*

$$f(x) = \Delta \int_{S_0^2} h(\Theta, E_\Theta x) d\Theta,$$

where  $h$  is obtained from  $g$  by

$$h(\Theta, x) = -\frac{1}{4\pi^2} \int_{\Theta^\perp} \frac{g(\Theta, x-y)}{|y|l(\Theta, y)} dy.$$

Proof: see, e.g. [NW01].

If we now adapt the new notation to the modified scatter model, i.e. the definition of the measurements on  $T(S_0^2)$  instead of on  $\Gamma$ , we obtain for each detector pair  $(d_i, d_j)$  a corresponding pair  $(\Theta, x)$ ,  $\Theta \in S_0^2$ ,  $x \in \Theta^\perp$  and two coefficients  $\lambda^\pm$ , i.e.  $\lambda^\pm = \lambda^\pm(\Theta, x)$ , satisfying

$$\begin{aligned} d_i &= x - \lambda^- \Theta, \\ d_j &= x + \lambda^+ \Theta, \\ \Theta &= \frac{d_j - d_i}{|d_j - d_i|}. \end{aligned}$$

We assume that the unknown activity distribution is compactly supported inside a smaller cylinder  $C_0 \subset C$  with radius  $R_0 < R$ , i.e.  $\text{supp}(f) \subset C_0$ . This is not a restriction to our model because close to the detectors we neither have activity nor scatter and attenuation.

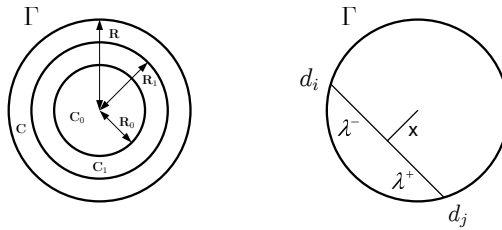


Figure 3.2: The new coordinates  $(\Theta, x)$  applied to the cylinder  $C$  and the detectors  $d_i$  and  $d_j$ : For each detector pair  $(d_i, d_j)$  on  $\Gamma$  we get a combination  $(\Theta, x)$  and two corresponding coefficients  $\lambda^\pm(\Theta, x)$  with  $d_i = x - \lambda^- \Theta$  and  $d_j = x + \lambda^+ \Theta$ .

When looking at a real scanner (see figure 3.3) we can see that the choice of a smaller domain for the activity is quite obvious since the crystals are usually “hidden” inside the chassis to protect them from being contaminated or damaged. Thus the actual available scanner radius is much smaller than the radius of the crystal arrays.

For a suitable choice of  $S_0^2$  the X-ray transform  $Pf(\Theta, x)$  is equal to zero for  $x \notin \text{supp}(f)$  so we restrict  $x$  to  $C_0$ . By the way, with this choice we avoid the case  $d_i$  close to  $d_j$  leading to  $\lambda^-, \lambda^+ > 0$  for all pairs  $(\Theta, x)$ . In addition we postulate  $\mu = 0$  outside another cylinders  $C_1$  with radius  $R_1$ ,  $R_0 < R_1 < R$ . The two different cylinder for activity and attenuation are meaningful because we assume that activity is only existent inside the patient.

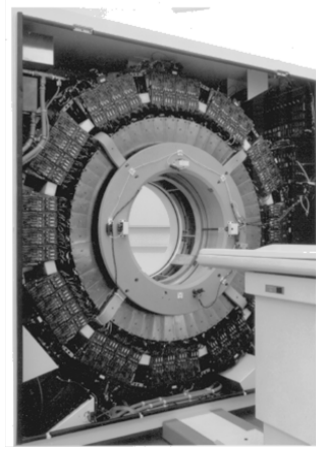


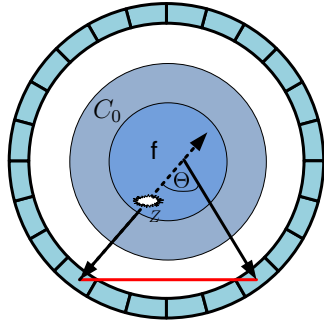
Figure 3.3: This image shows the standalone PET scanner installed at the University Hospital of Münster. After removing the cover we can look inside the device. In the front we have the patient bed that is moved into the ring during the measurement. It is easy to see that the actual useable bore radius is smaller than the radius of the crystal arrays.

Due to the fact that scatter only appears in combination with attenuation, the requirements on the attenuation coefficient  $\mu$  lead to  $k(x, \cdot, \cdot, \cdot, \cdot) = 0$  if  $x \notin C_1$ . Introducing the new notation to (3.2) we have

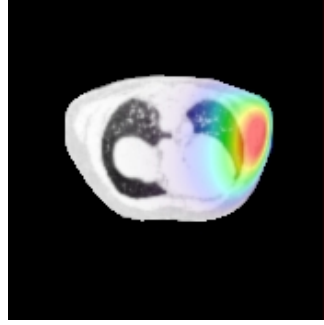
$$\begin{aligned}
 \underbrace{\frac{M_{x-\lambda^-\Theta, x+\lambda^+\Theta}}{V(x-\lambda^-\Theta, x+\lambda^+\Theta)}}_{=: g(\Theta, x)} &= \int_{x-\lambda^-\Theta}^{x+\lambda^+\Theta} f dt \\
 &+ \underbrace{\int_{C_0} \int_{S^2} \frac{G_{z, \omega}^0(x-\lambda^-\Theta) G_{z, -\omega}^S(x+\lambda^+\Theta)}{V(x-\lambda^-\Theta, x+\lambda^+\Theta)} d\omega f(z) dz}_{=: S^i f(\Theta, x)} \\
 &+ \underbrace{\int_{C_0} \int_{S^2} \frac{G_{z, -\omega}^0(x+\lambda^+\Theta) G_{z, \omega}^S(x-\lambda^-\Theta)}{V(x-\lambda^-\Theta, x+\lambda^+\Theta)} d\omega f(z) dz}_{=: S^j f(\Theta, x)} \\
 &+ \underbrace{\int_{C_0} \int_{S^2} \frac{G_{z, \omega}^S(x-\lambda^-\Theta) G_{z, -\omega}^S(x+\lambda^+\Theta)}{V(x-\lambda^-\Theta, x+\lambda^+\Theta)} d\omega f(z) dz}_{=: S^{ij} f(\Theta, x)},
 \end{aligned}$$

where  $S^i$  and  $S^j$  consider the case where only one particle is scattered and the other one reaches the detector unscattered, while  $S^{ij}$  considers the case of scattered particles in both directions.

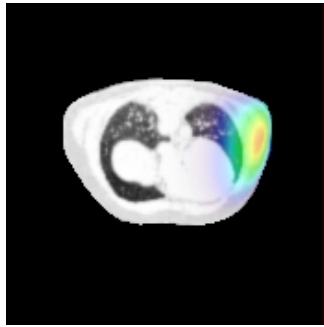
Regarding the restriction of  $x$  to  $C_0$  we define  $S^i f, S^j f, S^{ij} f = 0$  for  $x \notin C_0$ . For the estimates of the next sections it is convenient to have the scatter operators already zero for  $x \in C_0$  close to  $\partial C_0$ . At this point it becomes apparent why we introduced the energy dependency of photons. Particles have to undergo a strong scattering process in order to be measured on a line outside  $C_0$ . Thus we can find an energy threshold  $E_{\min}$  guaranteeing this restriction of the scatter operators. See figure 3.4 for a detailed description.



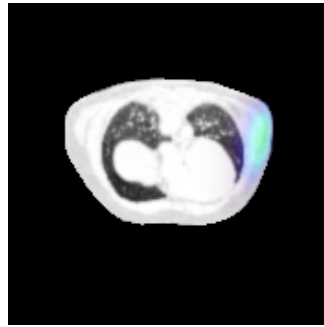
(a) Example of the scattering angle needed in order to measure particles on a line  $g(\Theta, x)$  with  $x \notin C_0$ .



(b) Scatter volume for  $S^i, S^j$  and  $S^{ij}$  using  $E_{\min} = 170$  keV



(c) Scatter volume for  $S^i, S^j$  and  $S^{ij}$  using  $E_{\min} = 325$  keV



(d) Scatter volume for  $S^i, S^j$  and  $S^{ij}$  using  $E_{\min} = 400$  keV

Figure 3.4: Particles that are measured on a line  $g(\Theta, x)$  with  $x$  outside  $C_0$  (red line) must have undergone a strong scattering process in order to reach the detectors, if we assume that only one of the two particles is scattered once, which is true in most applications. In case of the Siemens Biograph Sensation 16 that is installed in the University Hospital of Münster, the lower energy threshold is usually set to 400 keV. Regarding formula (1.12) from chapter 1, this leads to a maximum scattering angle of approximately  $\theta = 45^\circ$ . In examples b) - d) we show the projection volumes of all three scatter operators for detector combination (47, 145). As one can see the volumes are already very small (and can even be reduced by increasing  $E_{\min}$ ) although there are a lot of possible lora with a larger distance to the center of the FOV. Hence we can easily find a suitable threshold  $E_{\min}$  satisfying  $g(\Theta, x) = 0$  and therefore  $S^i f, S^j f, S^{ij} f = 0$  for  $x$  close to  $\partial C_0$ .

With the final definition of operator  $Q$  we arrive at the Neumann series.

$$\begin{aligned}
 g(\Theta, x) &= Pf(\Theta, x) + S^i f(\Theta, x) + S^j f(\Theta, x) + S^{ij} f(\Theta, x) \\
 \Leftrightarrow P^{-1}g(z) &= P^{-1}Pf(z) + P^{-1}S^i f(z) + P^{-1}S^j f(z) + P^{-1}S^{ij} f(z) \\
 \Leftrightarrow P^{-1}g(z) &= \left( I + \underbrace{P^{-1}S^i + P^{-1}S^j + P^{-1}S^{ij}}_{=: -Q} \right) f(z) \\
 \Leftrightarrow P^{-1}g(z) &= (I - Q) f(z).
 \end{aligned} \tag{3.5}$$

Before we can use Lemma 3.1.1 we have to assure that  $\|Q\| < 1$  is satisfied in an appropriate norm. If we can derive such a condition on  $\mu$  and  $E_{\min}$  we can reconstruct  $f$  iteratively from the measurements.

$$\begin{aligned}
 P^{-1}g(z) &= (I - Q) f(z) \\
 \Leftrightarrow (I - Q)^{-1} P^{-1}g(z) &= (I - Q)^{-1} (I - Q) f(z) \\
 \stackrel{\text{Lemma 3.1.1}}{\Leftrightarrow} \sum_{m=0}^{\infty} Q^m P^{-1}g(z) &= f(z).
 \end{aligned} \tag{3.6}$$

We still have to find a suitable function space for  $f$  (and as well as for  $\mu$ ) to analyze the norm of  $Q$ . For physical considerations it would be convenient to work with  $f \in L^1$  because in that case the norm of  $f$  denotes the number of particles in the system. In the next section we will take a closer look at the Sobolev space estimates for  $P$  and choose a suitable function space for activity distribution  $f$ .

### 3.2 A Suitable Function Space

Before we can derive the conditions on the attenuation map  $\mu$  and the energy threshold  $E_{\min}$  respectively, we have to choose an appropriate function space for  $f$ . Thus we will study some properties of the X-ray transform and its inverse operator. We start with the Sobolev space estimates for  $P$ . At this point it is necessary to work with the classical line model for PET and neglect the detector width (as mentioned in chapter 2) in order to use the well-known results for the X-ray transform.

**Theorem 3.2.1** *For each  $\alpha \in \mathbb{R}$  there exist positive constants  $c_1(\alpha, n)$  and  $c_2(\alpha, n)$  such that for  $f \in C_0^\infty(\Omega^n)$ ,  $\Omega^n \subset \mathbb{R}^n$*

$$c_1(\alpha, n) \cdot \|f\|_{H_0^\alpha(\Omega^n)} \leq \|Pf\|_{H^{\alpha+1/2}(T)} \leq c_2(\alpha, n) \cdot \|f\|_{H_0^\alpha(\Omega^n)}, \quad (3.7)$$

where the corresponding Sobolev spaces  $H^\alpha(T)$  are given by the norm

$$\|h\|_{H^\alpha(T)}^2 = \int_{S^{n-1}} \int_{\Theta^\perp} (1 + |\eta|^2)^\alpha |\widehat{h}(\Theta, \eta)|^2 d\eta d\Theta. \quad (3.8)$$

Proof: see [Nat86].

From (3.7) we know that  $P^{-1}$  is a continuous operator from  $H^{1/2}(T)$  into  $H_0^0(\Omega^n)$ , because for  $\alpha = 0$  we have with a certain constant  $c'_1(0, n)$

$$\begin{aligned} \|Pf\|_{H^{1/2}(T)} \geq c_1(0, n) \cdot \|f\|_{H_0^0(\Omega^n)} &= c_1(0, n) \cdot \|P^{-1}(Pf)\|_{H_0^0(\Omega^n)} \\ \Rightarrow \|P^{-1}g\|_{H_0^0(\Omega^n)} &\leq c'_1(0, n) \|g\|_{H^{1/2}(T)}, \end{aligned} \quad (3.9)$$

where we defined  $Pf = g$ . Hence a compactly supported  $f \in L^2(\Omega^n)$  seems to be a good choice for the sought-after activity distribution. We still have to check whether  $P$  is defined for such  $f$ . It is well-known that the X-ray transform which is usually defined for  $f \in C_0^\infty(\Omega^n)$  can be extended to  $L^1(\Omega^n)$  since

$$\int_{\Theta^\perp} |P_\Theta f(x)| dx = \int_{\Theta^\perp} \left| \int_{\mathbb{R}} f(x + t\Theta) dt \right| dx \leq \int_{\mathbb{R}^n} |f(x)| dx.$$

For a compactly supported  $f \in L^2(\Omega^n)$  we know that  $f \in L^1(\Omega^n)$ . Hence we can use  $P$  for this choice of  $f$ . For a detailed study of the X-ray transform on the spaces  $L^1(\mathbb{R}^n)$  and  $L^2(\mathbb{R}^n)$  we refer to Solmon [Sol76].

Regarding Theorem 3.2.1 and the considerations above we found a proper functional space for  $f$  in the 2D case. Again we have the problem in three dimensions that all estimates are performed on the complete tangent bundle  $T(S^2)$  but as we learned from the previous section we should work on  $T(S_0^2)$ . Following [DCT95] we will show that (3.9) is also valid on  $T(S_0^2)$  if  $S_0^2$  satisfies Orlov's condition.

Starting with a suitable  $f$  we have

$$\begin{aligned} \|Pf\|_{H^{1/2}(T(S_0^2))}^2 &= \int_{S_0^2} \int_{\Theta^\perp} \sqrt{1 + |\eta|^2} |\widehat{Pf}(\Theta, \eta)|^2 d\eta d\Theta \\ &\stackrel{\text{Theorem 3.1.3}}{=} \int_{S_0^2} \int_{\Theta^\perp} \sqrt{1 + |\eta|^2} |\widehat{f}(\eta)|^2 d\eta d\Theta. \end{aligned}$$

We introduce the  $\delta$ -distribution in order to integrate over the complete  $\mathbb{R}^3$ .

$$\begin{aligned}
 \|Pf\|_{H^{1/2}(T(S_0^2))}^2 &= \int_{S_0^2} \int_{\mathbb{R}^3} \sqrt{1+|\eta|^2} |\widehat{f}(\eta)|^2 \delta(\eta \cdot \Theta) d\eta d\Theta \\
 &= \int_{S_0^2} \int_{\mathbb{R}^3} \frac{\sqrt{1+|\eta|^2}}{|\eta|} |\widehat{f}(\eta)|^2 \delta\left(\frac{\eta}{|\eta|} \cdot \Theta\right) d\eta d\Theta \\
 &\geq \int_{S_0^2} \int_{\mathbb{R}^3} |\widehat{f}(\eta)|^2 \delta\left(\frac{\eta}{|\eta|} \cdot \Theta\right) d\eta d\Theta \\
 &\geq \int_{\mathbb{R}^3} |\widehat{f}(\eta)|^2 d\eta \cdot \underbrace{\left( \inf_{\Theta' \in S^2} \int_{S_0^2} \delta(\Theta' \cdot \Theta) d\Theta \right)}_{=: c} \\
 &= c \cdot \|f\|_{L^2(\Omega^3)}^2.
 \end{aligned}$$

If now the subset  $S_0^2 \subset S^2$  satisfies Orlov's condition the constant  $c$  is positive. We state this result in the following Theorem.

**Theorem 3.2.2** *If  $S_0^2 \subset S^2$  satisfies Orlov's condition there exists a positive constant  $c$  such that for a compact supported  $f \in L^2(\Omega^3)$ ,  $\Omega^3 \subset \mathbb{R}^3$*

$$\|Pf\|_{H^{1/2}(T(S_0^2))} \geq c \cdot \|f\|_{L^2(\Omega^3)}. \quad (3.10)$$

Using Orlov's inversion formula we know that  $P^{-1}$  is a continuous operator from the Sobolev space  $H^{1/2}(T(S_0^2))$  into  $L^2(\Omega^3)$ , or better  $L^2(C_0)$  if we step back to our cylinder  $C$  and its subset  $C_0$ . Regarding (3.5) we have to assure that the scatter operators  $S^i, S^j$  and  $S^{ij}$  are continuous operators from  $L^2(C_0)$  into  $H^\alpha(T(S_0^2))$ , while  $\alpha \geq 1/2$ . Although  $\alpha = 1/2$  is sufficient for our estimates we may also show  $\|Sf\|_{H^{1/2+\beta}} \leq c \cdot \|f\|_{L^2}$  for  $\beta \geq 0$ , since  $\|Sf\|_{H^{1/2}} \leq \|Sf\|_{H^{1/2+\beta}}$  regarding (3.8). Therefore we will give the corresponding estimates in  $H^1$  giving us the possibility to use the classical definition of a Sobolev space containing (distributional) derivatives of the function. The connection between the fractional order Sobolev space with  $\alpha = 1$  and the classical definition is given by

$$\begin{aligned}
 \|f\|_{H^1(T)}^2 &= \int_{S^2} \int_{\Theta^\perp} (1+|\eta|^2) |\widehat{f}(\Theta, \eta)|^2 d\eta d\Theta \\
 &= \int_{S^2} \left[ \int_{\Theta^\perp} |\widehat{f}(\Theta, \eta)|^2 d\eta + \int_{\Theta^\perp} |\eta|^2 |\widehat{f}(\Theta, \eta)|^2 d\eta \right] d\Theta.
 \end{aligned}$$

We have, using the definition of the Fourier transformation and integration by parts

$$\begin{aligned}
 \int_{\Theta^\perp} |\eta|^2 |\hat{f}(\Theta, \eta)|^2 d\eta &= \int_{\Theta^\perp} |\eta|^2 \hat{f}(\Theta, \eta) \bar{\hat{f}}(\Theta, \eta) d\eta \\
 &= \int_{\Theta^\perp} \left( \sum_{j=1}^n \eta_j^2 \right) \hat{f}(\Theta, \eta) \bar{\hat{f}}(\Theta, \eta) d\eta \\
 &= - \int_{\Theta^\perp} \left( \sum_{j=1}^n \frac{\partial}{\partial x_j^2} f \right) (\Theta, \eta) \bar{\hat{f}}(\Theta, \eta) d\eta \\
 &= - \int_{\Theta^\perp} (\Delta f) (\Theta, \eta) \bar{\hat{f}}(\Theta, \eta) d\eta \\
 &= - \int_{\Theta^\perp} \Delta f(\Theta, x) \bar{f}(\Theta, x) dx \\
 &= \int_{\Theta^\perp} \sum_{i=1}^n \left| \frac{\partial}{\partial x_i} f(\Theta, x) \right|^2 dx.
 \end{aligned}$$

Finally we arrive at the classical definition of the Sobolev space  $H^1(T)$ :

$$\begin{aligned}
 \|f\|_{H^1(T)}^2 &= \int_{S^{n-1}} \int_{\Theta^\perp} |\hat{f}(\Theta, \eta)|^2 d\eta + \int_{\Theta^\perp} \sum_{i=1}^n \left| \frac{\partial}{\partial x_i} f(\Theta, x) \right|^2 dx d\Theta \\
 &= \int_{S^{n-1}} \int_{\Theta^\perp} |f(\Theta, x)|^2 dx + \int_{\Theta^\perp} \sum_{i=1}^n \left| \frac{\partial}{\partial x_i} f(\Theta, x) \right|^2 dx d\Theta \\
 &= \int_{S^{n-1}} \int_{\Theta^\perp} |f(\Theta, x)|^2 + \sum_{i=1}^n \left| \frac{\partial}{\partial x_i} f(\Theta, x) \right|^2 dx d\Theta,
 \end{aligned}$$

or more precise if we are talking about  $n = 3$  and the restriction of  $\Theta$  to  $S_0^2 \subset S^2$

$$\|f\|_{H^1(T(S_0^2))}^2 = \int_{S_0^2} \int_{\Theta^\perp} |f(\Theta, x)|^2 + \sum_{i=1}^3 \left| \frac{\partial}{\partial x_i} f(\Theta, x) \right|^2 dx d\Theta. \quad (3.11)$$

Now that we have found a suitable function space for  $f$  we have to check whether  $S^i$ ,  $S^j$  and  $S^{ij}$  satisfy the required space estimates. Next to the investigation of a general existence of these estimates we have to choose  $E_{\min}$  according to the smallness requirements needed for the Neumann series approach.

The example given in figure 3.5 shows that scatter does not always has a huge impact on the reconstruction results. Assuming we have a measurement (performed with a pre-defined  $E_{\min}$ ) and a corresponding attenuation map  $\mu$ . Can we give a “measure” that allows us to forecast the need of an exact scatter correction prior to the reconstruction using the perturbation approach?

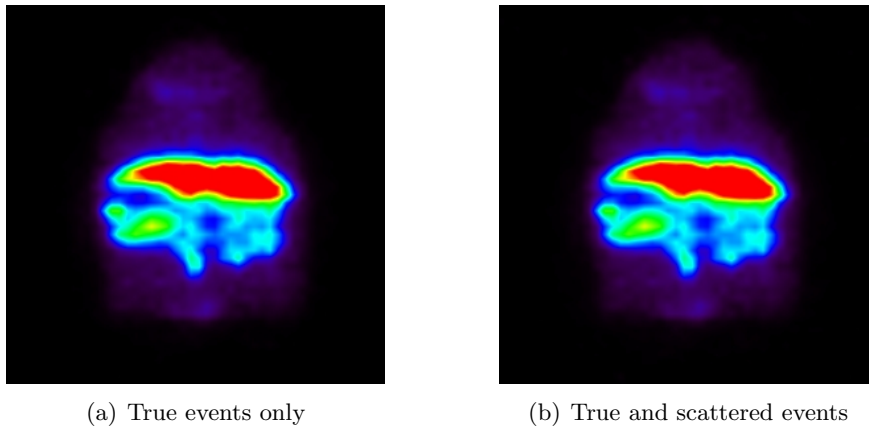


Figure 3.5: An example on the impact of scatter in small animals: The whole measuring process of an FDG study with the Siemens Inveon small animal PET scanner was simulated. The left image shows a reconstruction of true events only whereas the right image includes scattered events. The differences are negligible, i.e. no scatter correction has to be performed to quantify the reconstruction.

### 3.3 The Single Scatter Approximation

There are several investigations [WBD<sup>+</sup>02, AAWK04, MTJ<sup>+</sup>07] showing that single scatter is the most dominant image degrading factor in PET. Some particles may be scattered twice or even three times before they are measured, but the effort to correct for those effects is not justified in most applications. Thus we will start to analyze the scatter operators in the single scatter case starting with  $S^i$ . If we introduce the new notation  $(\Theta, x)$  and the necessary restrictions for the domains of  $f, k$  and  $\mu$  respectively to (??) we have

$$S^i f(\Theta, x) = \int_{C_0} \frac{(\lambda^- + \lambda^+)^2}{e^{-\int_{x-\lambda^-}^{x+\lambda^+} \mu(s, E_0) ds}} \int_{E_{\min}}^{E_0} \int_{\gamma} k\left(z', \frac{x + \lambda^+ \Theta - z'}{|x + \lambda^+ \Theta - z'|}, \frac{z - x + \lambda^- \Theta}{|z - x + \lambda^- \Theta|}, E, E_0\right) \\ \times \frac{e^{-\int_{x-\lambda^-}^{z'} \mu(s, E_0) ds} e^{-\int_{z'}^{x+\lambda^+} \mu(s, E) ds}}{|z - x + \lambda^- \Theta|^2 |x + \lambda^+ \Theta - z'|^2} dz' dE f(z) dz$$

or in a more compact representation

$$S^i f(\Theta, x) = \int_{C_0} B^i(\Theta, x, z) f(z) dz,$$

where we defined

$$B^i(\Theta, x, z) = \frac{(\lambda^- + \lambda^+)^2}{e^{-\int_{x-\lambda^-}^{x+\lambda^+} \mu(s, E_0) ds}} \int_{E_{\min}}^{E_0} \int_{\gamma} k\left(z', \frac{x + \lambda^+ \Theta - z'}{|x + \lambda^+ \Theta - z'|}, \frac{z - x + \lambda^- \Theta}{|z - x + \lambda^- \Theta|}, E, E_0\right) \\ \times \frac{e^{-\int_{x-\lambda^-}^{z'} \mu(s, E_0) ds} e^{-\int_{z'}^{x+\lambda^+} \mu(s, E) ds}}{|z - x + \lambda^- \Theta|^2 |x + \lambda^+ \Theta - z'|^2} dz' dE.$$

The curve  $\gamma$  is given by

$$\gamma : [t_0, 0] \rightarrow \mathbb{R}^3, \quad \gamma(t) = z - t \frac{z - x + \lambda^- \Theta}{|z - x + \lambda^- \Theta|}, \quad \|\dot{\gamma}(t)\|_2 = 1,$$

with  $t_0 < 0$  satisfying the condition

$$z - t_0 \frac{z - x + \lambda^- \Theta}{|z - x + \lambda^- \Theta|} \in \partial C_1.$$

There are lots of publications dealing with transport problems in several applications. The attenuation coefficient  $\mu$  always has a different meaning and therefore different characteristics. In some applications there is a dependence on the incident angle of particles as in [SU08], i.e.  $\mu = \mu(x, \Theta)$ , or as in our case dependency on the energy of photons, i.e.  $\mu = \mu(x, E)$ . Of course there are also applications [BT08] where the attenuation coefficient only depends on  $x$ , i.e.  $\mu = \mu(x)$ . In addition to the different meanings of  $\mu$  there are certainly different requirements on attenuation coefficient.

For our application we postulate  $\mu \in C^1(C_1 \times (0, E_0])$  and show that under this restriction the corresponding operator norms exist as well as we can find a suitable  $E_{\min}$  for each  $\mu$  in order to satisfy the smallness conditions needed for the Neumann series approach. Since we know (see figure 3.4) that the scatter operators are zero not only for  $x \in \Theta^\perp, x \notin C_0$ , but already for  $x \in C_0, x$  close to  $\partial C_0$ , (with a certain choice of  $E_{\min}$ ), we will restrict our analysis to this domain, i.e. we are using the following norm

$$\begin{aligned} \|S^i f\|_{H^1(T(S_0^2, C_0))} &= \int_{S_0^2} \int_{\substack{\Theta^\perp \\ x \in C_0}} |S^i f(\Theta, x)|^2 + \sum_{n=1}^3 \left| \frac{\partial}{\partial x_n} S^i f(\Theta, x) \right|^2 dx d\Theta \\ &= \underbrace{\int_{S_0^2} \int_{\substack{\Theta^\perp \\ x \in C_0}} |S^i f(\Theta, x)|^2 dx d\Theta}_a + \underbrace{\int_{S_0^2} \int_{\substack{\Theta^\perp \\ x \in C_0}} \sum_{n=1}^3 \left| \frac{\partial}{\partial x_n} S^i f(\Theta, x) \right|^2 dx d\Theta}_b. \end{aligned}$$

To begin with we take a closer look at part a) and therefore at  $B^i$ . We will give some estimates of the different components of  $B^i$  based on the geometrical properties of the scanner, in order to get an impression of the magnitude of scattering as well as on the impact of modifications of the scanner geometry.

The two distances in the denominator can easily be estimated since the detectors  $x - \lambda^- \Theta$  and  $x + \lambda^+ \Theta$  (or, when using the old notation  $d_i, d_j$ ) are on  $\Gamma \in \partial C$  while  $z, z'$  are restricted to smaller cylinder  $C_0$  and  $C_1$  respectively inside  $C$ , i.e.

$$\begin{aligned} |z - x + \lambda^- \Theta|^{-2} &\leq (R - R_0)^{-2}, \\ |x + \lambda^+ \Theta - z'|^{-2} &\leq (R - R_1)^{-2}. \end{aligned}$$

For a given scanner with radius  $R$  we may limit the largest radius  $R_0$  where activity is allowed as well as the largest radius  $R_1$  where attenuation is permitted while regarding the condition  $R_0 < R_1 < R$ . It is obvious that by decreasing the size of the scanned object (i.e.  $R_0$  and  $R_1$ ) we decrease the impact of scatter at the same time.

As introduced in chapter 2 the scatter kernel  $k$  that depends on the attenuation coefficient  $\mu$  can be written as

$$k(x, \Theta, \Theta', E, E') = \left(1 - e^{-\mu(x, E')}\right) \kappa(\Theta \cdot \Theta', E, E'),$$

where  $\kappa$  is the probability of scattering from  $\Theta'$  in direction  $\Theta$  given by the Klein-Nishina formula (1.14) presented in chapter 1. In order to assure that the probability of scattering in any direction is equal to one,  $\kappa$  can be normalized such that  $\int_{S^2} \kappa(\Theta \cdot \Theta', E, E') d\Theta' = 1$ . Thus  $k$  is surely bounded by 1 just like the two exponentials in the nominator, since  $\mu(x, E) \geq 0$  for all combinations of  $x$  and  $E$ .

The sum of  $\lambda^+$  and  $\lambda^-$  is limited by the largest possible distance between two detectors in the cylinder

$$(\lambda^- + \lambda^+)^2 \leq \left(\sqrt{(2R)^2 + L^2}\right)^2 = 4R^2 + L^2,$$

see figure 3.2. Finally the third exponential is bounded by the maximum of the attenuation coefficient times  $\sqrt{4R_1^2 + L_1^2}$ , since  $\mu = 0$  outside  $C_1$ , and we deduce

$$\frac{\int_{e^{x-\lambda-\Theta}}^{e^{x+\lambda+\Theta}} \mu(s, E_0) ds}{e^{x-\lambda-\Theta}} \leq e^{\sqrt{4R_1^2 + L_1^2} \max_z \mu(z, E_0)}.$$

Collecting all terms leads to the following simple approximation

$$|B^i(\Theta, x, z)| \leq \frac{\sqrt{4R_1^2 + L_1^2} (4R^2 + L^2) e^{\sqrt{4R_1^2 + L_1^2} \max_z \mu(z, E_0)}}{(R - R_0)^2 (R - R_1)^2} (E_0 - E_{\min}) =: b_a^i.$$

These estimates are of course quite rough, but we are interested if there are generally any meaningful estimates. Looking again at a) we are now allowed to use the Cauchy-Schwarz inequality and write

$$\begin{aligned} \int_{S_0^2} \int_{\substack{\Theta^\perp \\ x \in C_0}} |S^i f(\Theta, x)|^2 dx d\Theta &= \int_{S_0^2} \int_{\substack{\Theta^\perp \\ x \in C_0}} \left| \int_{C_0} B^i(\Theta, x, z) f(z) dz \right|^2 dx d\Theta \\ &\leq \int_{S_0^2} \int_{\substack{\Theta^\perp \\ x \in C_0}} \int_{C_0} |B^i(\Theta, x, z)|^2 dz \int_{C_0} |f(z)|^2 dz dx d\Theta \\ &= \|f\|_{L^2(C_0)} \cdot \int_{S_0^2} \int_{\substack{\Theta^\perp \\ x \in C_0}} \int_{C_0} \underbrace{|B^i(\Theta, x, z)|}_{\leq b_a^i} dz dx d\Theta \\ &\leq \|f\|_{L^2(C_0)} \cdot c_a^i([\mu, R_0, L_0, R_1, L_1], [L, R], [E_{\min}]). \end{aligned}$$

Based on our discussion we know that there are such constants  $b_a^i$  and  $c_a^i$  depending on the patients mumap  $\mu$  and the necessary restrictions  $R_0, L_0$  and  $R_1, L_1$ , the energy threshold  $E_{\min}$  as well as the parameters  $R$  and  $L$  describing the scanner geometry. In order to satisfy the smallness conditions on the operator norm we may tune all parameters to reduce  $c_a^i$ . In real world applications we may of course only adjust the energy threshold  $E_{\min}$ , since the scanner geometry and especially the patient are given and cannot be modified.

Before we look at part b) we like to study some properties of the attenuation coefficient  $\mu$ . At the beginning of this section we postulated  $\mu \in C^1(C_1 \times (0, E_0])$ . Now we will show that the attenuation coefficient is always - due to the definition of the energy dependency - continuously differentiable with respect to  $E$ . From chapter 1 we know that  $\mu$  can be written as

$$\mu(x, E) = \mu_{Compton}(x) \cdot \frac{\sigma(E/E_0)}{\sigma(1)}$$

with  $\sigma$  given by (1.15), which represents the total cross section for a certain energy level. In case of an unscattered photon  $E$  is equal to  $E_0$  and the coefficient is equal to one. Regarding the definition of  $\sigma$  and the restriction  $E_{\min} > 0$  we conclude that  $\mu$  always is continuously differentiable with respect to  $E$ . Thus we only have to postulate  $\mu \in C^1$  with respect to  $x$ .

Regarding part b) we now have to check the partial derivatives of  $S^i$  and  $B^i$  respectively to finish the analysis of the operator norm. We have

$$\begin{aligned}
 & \left| \frac{\partial}{\partial x_1} B^i(\Theta, x, z) \right| \\
 = & \left| \left[ \frac{\partial}{\partial x_1} \frac{(\lambda^- + \lambda^+)^2}{e^{-\int_{x-\lambda^-}^{x+\lambda^+} \mu(s, E_0) ds}} \right] \times \left[ \int_{E_{\min}}^{E_0} \int_{\gamma} k \left( z', \frac{x + \lambda^+ \Theta - z'}{|x + \lambda^+ \Theta - z'|}, \frac{z - x + \lambda^- \Theta}{|z - x + \lambda^- \Theta|}, E, E_0 \right) \right. \right. \\
 & \times \left. \left. \frac{e^{-\int_{x-\lambda^-}^{z'} \mu(s, E_0) ds} e^{-\int_{z'}^{x+\lambda^+} \mu(s, E) ds}}{|z - x + \lambda^- \Theta|^2 |x + \lambda^+ \Theta - z'|^2} dz' dE \right] + \left[ \frac{(\lambda^- + \lambda^+)^2}{e^{-\int_{x-\lambda^-}^{x+\lambda^+} \mu(s, E_0) ds}} \right] \right. \\
 & \times \left[ \frac{\partial}{\partial x_1} \int_{E_{\min}}^{E_0} \int_{\gamma} k \left( z', \frac{x + \lambda^+ \Theta - z'}{|x + \lambda^+ \Theta - z'|}, \frac{z - x + \lambda^- \Theta}{|z - x + \lambda^- \Theta|}, E, E_0 \right) \right. \\
 & \left. \left. \times \frac{e^{-\int_{x-\lambda^-}^{z'} \mu(s, E_0) ds} e^{-\int_{z'}^{x+\lambda^+} \mu(s, E) ds}}{|z - x + \lambda^- \Theta|^2 |x + \lambda^+ \Theta - z'|^2} dz' dE \right] \right|.
 \end{aligned}$$

Some parts have already been analyzed while studying a). Using this knowledge and the triangle inequality we proceed with our estimate. We have

$$\begin{aligned}
 & \left| \frac{\partial}{\partial x_1} B^i(\Theta, x, z) \right| \\
 \leq & \left| \frac{\partial}{\partial x_1} \frac{(\lambda^- + \lambda^+)^2}{e^{-\int_{x-\lambda^-}^{x+\lambda^+} \mu(s, E_0) ds}} \right| \times \frac{(E_0 - E_{\min}) \sqrt{4R^2 + L^2}}{(R - R_0)^2 (R - R_1)^2} \\
 & + \left| \frac{\partial}{\partial x_1} \int_{E_{\min}}^{E_0} \int_{\gamma} k \left( z', \frac{x + \lambda^+ \Theta - z'}{|x + \lambda^+ \Theta - z'|}, \frac{z - x + \lambda^- \Theta}{|z - x + \lambda^- \Theta|}, E, E_0 \right) \right. \\
 & \left. \times \frac{e^{-\int_{x-\lambda^-}^{z'} \mu(s, E_0) ds} e^{-\int_{z'}^{x+\lambda^+} \mu(s, E) ds}}{|z - x + \lambda^- \Theta|^2 |x + \lambda^+ \Theta - z'|^2} dz' dE \right| \times (4R^2 + L^2) e^{\sqrt{4R_1^2 + L_1^2} \max_z \mu(z, E_0)}.
 \end{aligned}$$

Remembering the definition of  $\lambda^\pm$  we have  $x \pm \lambda^\pm \Theta = y^\pm \in \Gamma$ , i.e.  $\lambda^\pm$  is nothing else but the length of the vector connecting  $x \in C_0$  with the boundary of the cylinder  $C$ . Because of the suitable definition of the different cylinder it is obvious that  $\lambda^\pm > 0$  for all combinations  $(\Theta, x)$ . Thus the derivative of  $(\lambda^- + \lambda^+)^2$  exists and is bounded by a constant.

To complete the estimate of the first component we need to analyze the derivative of the exponential in the denominator. Since it is more convenient for us not to have a

dependency on  $x$  in the integration limits of the attenuation integral, we introduce the curve  $\gamma$  as

$$\gamma : [0, 1] \rightarrow \mathbb{R}^3, \quad \gamma(t) = (x - \lambda^- \Theta) + t(\lambda^+ + \lambda^-) \Theta, \quad \|\dot{\gamma}(t)\|_2 = \lambda^+ + \lambda^-,$$

and are now allowed to write

$$\begin{aligned} \left| \frac{\partial}{\partial x_1} e^{\int_{x-\lambda^- \Theta}^{x+\lambda^+ \Theta} \mu(s, E_0) ds} \right| &= \left| \frac{\partial}{\partial x_1} \int_0^1 \mu(\gamma(t), E_0) (\lambda^+ + \lambda^-) dt \right| \\ &= \left| \frac{\partial}{\partial x_1} \int_0^1 \mu(\gamma(t), E_0) (\lambda^+ + \lambda^-) dt \right| \\ &= \left| \int_0^1 \mu(\gamma(t), E_0) (\lambda^+ + \lambda^-) dt \right| \\ &\quad \times \left| \frac{\partial}{\partial x_1} \int_0^1 \mu(\gamma(t), E_0) (\lambda^+ + \lambda^-) dt \right|. \end{aligned}$$

Since  $\mu$  as well as  $\lambda^\pm$  are at least in  $C^1$  the derivative exists and is bounded by a constant. Again we apply the triangle inequality to finish the estimate.

$$\begin{aligned} \left| \frac{\partial}{\partial x_1} \frac{(\lambda^- + \lambda^+)^2}{e^{-\int_{x-\lambda^- \Theta}^{x+\lambda^+ \Theta} \mu(s, E_0) ds}} \right| &= \left| (\lambda^- + \lambda^+)^2 \left[ \frac{\partial}{\partial x_1} e^{\int_{x-\lambda^- \Theta}^{x+\lambda^+ \Theta} \mu(s, E_0) ds} \right] \right. \\ &\quad \left. + e^{\int_{x-\lambda^- \Theta}^{x+\lambda^+ \Theta} \mu(s, E_0) ds} \left[ \frac{\partial}{\partial x_1} (\lambda^- + \lambda^+)^2 \right] \right| \\ &\leq (4R^2 + L^2) \left| \frac{\partial}{\partial x_1} e^{\int_{x-\lambda^- \Theta}^{x+\lambda^+ \Theta} \mu(s, E_0) ds} \right| \\ &\quad + e^{\sqrt{4R_1^2 + L_1^2} \max_z \mu(z, E_0)} \left| \frac{\partial}{\partial x_1} (\lambda^- + \lambda^+)^2 \right|. \end{aligned}$$

Based on our discussion we know that there are constants for both derivatives and hence we have an estimate for the first component. Before we start deriving the estimate for the last part containing the scatter kernel we like to take a closer look at the properties of  $k$ . As we know  $k$  can be written as

$$k(x, \Theta, \Theta', E, E') = \left(1 - e^{-\mu(x, E')}\right) \kappa(\Theta \cdot \Theta', E, E'),$$

where  $\kappa$  is defined in chapter 1. Regarding the properties of  $\mu$  discussed in this section and the definition of the Klein-Nishina formula  $\kappa$  we conclude that  $k$  also is continuously differentiable.

Hence we can easily proceed with our estimation of the operator norm.

$$\begin{aligned}
 & \left| \frac{\partial}{\partial x_1} \int_{E_{\min}}^{E_0} \int_{\gamma} k \left( z', \frac{x + \lambda^+ \Theta - z'}{|x + \lambda^+ \Theta - z'|}, \frac{z - x + \lambda^- \Theta}{|z - x + \lambda^- \Theta|}, E, E_0 \right) \right. \\
 & \quad \left. \times \frac{e^{-\int_{x-\lambda^- \Theta}^{z'} \mu(s, E_0) ds} e^{-\int_{z'}^{x+\lambda^+ \Theta} \mu(s, E) ds}}{|z - x + \lambda^- \Theta|^2 |x + \lambda^+ \Theta - z'|^2} dz' dE \right| \\
 &= \left| \int_{E_{\min}}^{E_0} \int_{\gamma_2} \frac{\partial}{\partial x_1} k \left( z', \frac{x + \lambda^+ \Theta - z'}{|x + \lambda^+ \Theta - z'|}, \frac{z - x + \lambda^- \Theta}{|z - x + \lambda^- \Theta|}, E, E_0 \right) \right. \\
 & \quad \left. \times \frac{e^{-\int_{x-\lambda^- \Theta}^{z'} \mu(s, E_0) ds} e^{-\int_{z'}^{x+\lambda^+ \Theta} \mu(s, E) ds}}{|z - x + \lambda^- \Theta|^2 |x + \lambda^+ \Theta - z'|^2} dz' dE \right| \\
 &\leq \int_{E_{\min}}^{E_0} \int_{\gamma_2} \left| \frac{\partial}{\partial x_1} k \left( z', \frac{x + \lambda^+ \Theta - z'}{|x + \lambda^+ \Theta - z'|}, \frac{z - x + \lambda^- \Theta}{|z - x + \lambda^- \Theta|}, E, E_0 \right) \right. \\
 & \quad \left. \times \frac{e^{-\int_{x-\lambda^- \Theta}^{z'} \mu(s, E_0) ds} e^{-\int_{z'}^{x+\lambda^+ \Theta} \mu(s, E) ds}}{|z - x + \lambda^- \Theta|^2 |x + \lambda^+ \Theta - z'|^2} dz' dE \right| \\
 &= \int_{E_{\min}}^{E_0} \int_{\gamma_2} \left| \left[ \frac{\partial}{\partial x_1} k \left( z', \frac{x + \lambda^+ \Theta - z'}{|x + \lambda^+ \Theta - z'|}, \frac{z - x + \lambda^- \Theta}{|z - x + \lambda^- \Theta|}, E, E_0 \right) \right] \right. \\
 & \quad \times \frac{e^{-\int_{x-\lambda^- \Theta}^{z'} \mu(s, E_0) ds} e^{-\int_{z'}^{x+\lambda^+ \Theta} \mu(s, E) ds}}{|z - x + \lambda^- \Theta|^2 |x + \lambda^+ \Theta - z'|^2} + k \left( z', \frac{x + \lambda^+ \Theta - z'}{|x + \lambda^+ \Theta - z'|}, \frac{z - x + \lambda^- \Theta}{|z - x + \lambda^- \Theta|}, E, E_0 \right) \\
 & \quad \left. \left[ \frac{\partial}{\partial x_1} \frac{e^{-\int_{x-\lambda^- \Theta}^{z'} \mu(s, E_0) ds} e^{-\int_{z'}^{x+\lambda^+ \Theta} \mu(s, E) ds}}{|z - x + \lambda^- \Theta|^2 |x + \lambda^+ \Theta - z'|^2} \right] \right| dz' dE.
 \end{aligned}$$

In order to change integration and differentiation we introduced a different curve  $\gamma_2$  that does not have any dependency on  $x$  in the integration limits. The new curve  $\gamma_2$  is given by the composition of the former curve  $\gamma$  and  $\phi$  defined as

$$\phi : [0, 1] \rightarrow [t_0, 0], \quad \phi(t) = (1-t)t_0, \quad \phi'(t) = -t_0 > 0,$$

with  $t_0 < 0$  still satisfying the condition

$$z - t_0 \frac{z - x + \lambda^- \Theta}{|z - x + \lambda^- \Theta|} \in \partial C_1.$$

Thus  $\gamma_2$  can be written as  $\gamma_2 = \gamma \circ \phi$  and

$$\gamma_2 : [0, 1] \rightarrow \mathbb{R}^3, \quad \gamma_2(t) = z - (1-t)t_0 \frac{z-x+\lambda^-\Theta}{|z-x+\lambda^-\Theta|}, \quad \|\dot{\gamma}_2(t)\|_2 = t_0.$$

Again we can use some results of a) and remain to give estimates for the two derivatives. As mentioned before, due to the definition of the scatter kernel, the corresponding derivative exists and is also bound by a constant. Along the lines of the estimate for the first derivative we analyzed, we may conclude that also the derivative of the quotient consisting of the two exponentials and the two distances exists and is again bounded. Thus we have estimates or at least proven that there exist estimates in order to satisfy the space estimates needed for the Neumann series approach. We have

$$\begin{aligned} \int_{S_0^2} \int_{\substack{\Theta^\perp \\ x \in C_0}} \left| \frac{\partial}{\partial x_n} S^i f(\Theta, x) \right|^2 dx d\Theta &= \int_{S_0^2} \int_{\substack{\Theta^\perp \\ x \in C_0}} \left| \frac{\partial}{\partial x_n} \int_{C_0} B^i(\Theta, x, z) f(z) dz \right|^2 dx d\Theta \\ &\leq \int_{S_0^2} \int_{\substack{\Theta^\perp \\ x \in C_0}} \int_{C_0} \left| \frac{\partial}{\partial x_n} B^i(\Theta, x, z) \right|^2 dz \int_{C_0} |f(z)|^2 dz dx d\Theta \\ &= \|f\|_{L^2(C_0)} \cdot \int_{S_0^2} \int_{\substack{\Theta^\perp \\ x \in C_0}} \int_{C_0} \underbrace{\left| \frac{\partial}{\partial x_n} B^i(\Theta, x, z) \right|}_{\leq b_b^i} dz dx d\Theta \\ &\leq \|f\|_{L^2(C_0)} \cdot c_b^i(\mu, R_0, L_0, R_1, L_1, [L, R], [E_{\min}]). \end{aligned}$$

Collecting all results we have the following Theorem.

**Theorem 3.3.1** *Let  $\mu \in C^1(C_1 \times (0, E_0])$ . Then we have two constants  $b_a^i$  and  $b_b^i$ , depending on the patients mumap  $\mu$ , the necessary restrictions  $R_0, L_0$  and  $R_1, L_1$ , the energy threshold  $E_{\min}$  as well as the parameters  $R$  and  $L$  describing the scanner geometry satisfying*

$$\begin{aligned} |B^i(\Theta, x, z)| &\leq b_a^i, \\ \left| \frac{\partial}{\partial x_1} B^i(\Theta, x, z) \right| &\leq b_b^i. \end{aligned}$$

*Thus, the  $H^1(T(S_0^2))$ -norm of  $S^i$  is bounded and therefore  $S^i$  is a continuous operator from  $L^2(C_0)$  into  $H^1(T(S_0^2))$ . Additionally, when increasing the energy threshold the norm can arbitrarily be reduced in order satisfy the small requirement needed to apply the Neumann series approach.*

Due to the symmetry of  $S^i$  and  $S^j$  the results of Theorem 3.3.1 can also be used for  $S^j$ . The main difference between  $S^i, S^j$  and  $S^{ij}$  is the fact, that in the latter case both particles are scattered instead of only one. When regarding the scatter model in case of single scatter (??) we can see, that this difference does not significantly change the structure of the operator. Hence we may use the same strategy to derive a simple estimate for  $S^{ij}$  which may also be scaled using a suitable  $E_{\min}$ .

### 3.4 Multiple Scatter

For some applications it might be useful even to correct for multiple scatter and of course we are interested to complete our mathematical model with this case. As already discussed in the introduction we are not able to set perfect energy thresholds. Hence we will study the case of multiple scatter using discrete energy bins following the lines of Barrett [BGCC99]. Starting with the scatter integral introduced in section 2.2.2 we replace

$$Ku(x, \Theta, E) = \int_{S^2} \int_E^{E_0} k(x, \Theta, \Theta', E, E') u(x, \Theta', E') dE' d\Theta'$$

with the discrete version

$$\begin{aligned} Ku(x, \Theta, E_m) &= \int_{S^2} \sum_{j=0}^{m-1} k(x, \Theta, \Theta', E_j, E_m) u(x, \Theta', E_j) d\Theta \\ &= \sum_{j=0}^{m-1} \underbrace{\int_{S^2} k(x, \Theta, \Theta', E_j, E_m) u(x, \Theta', E_j) d\Theta}_{K_{mj}u_j(x, \Theta)} \\ &= \sum_{j=0}^{m-1} K_{mj}u_j(x, \Theta). \end{aligned} \quad (3.12)$$

For a given bin size  $\Delta E$  the energy level  $E_m$  is defined as  $E_m = E_0 - m\Delta E$  whereas  $E_0$  is again 511 keV, i.e. the full energy of emitted particles. The upper summation index ends at  $m - 1$  because only particles with energy higher than  $E_m$  contribute to the number of photons at energy level  $m$ . By inserting (3.12) into (2.29) we obtain for the case that only one photon is scattered

$$\begin{aligned} S^{i*}(d_i, d_j) &= \int_{C_0} \int_{S^2} \sum_{m=E_{\min s_0}(d_i, \Theta)}^{E_0} \int_{j=0}^{m-1} \sum_{j=0}^{m-1} K_{mj}u_{j,z, \frac{z-d_j}{|z-d_j|}}(d_i + s\Theta, \Theta) \\ &\quad \times \frac{e^{-\int_z^{d_j} \mu(t, E_0) dt} e^{-\int_s^0 \mu(d_i + s'\Theta, m) ds'}}{|z - d_j|^2} ds d\Theta f(z) dz, \end{aligned}$$

where we are still using the old notation instead of the new  $(\Theta, x)$  notation. Additionally, we neglect the function  $V(d_i, d_j)$  that was introduced in (3.1) and write  $S^{i*}$  instead of  $S^i$  to clearly separate these two operators. If we take a closer look at the inner sum

$$\sum_{j=0}^{m-1} K_{mj}u_{j,z, \frac{z-d_j}{|z-d_j|}}(d_i + s\Theta, \Theta) \frac{e^{-\int_z^{d_j} \mu(t, E_0) dt} e^{-\int_s^0 \mu(d_i + s'\Theta, m) ds'}}{|z - d_j|^2} ds d\Theta$$

we can see that for  $m = 1$  we obtain again the case of single scatter as discussed before. For  $m = 2$  we obtain a second summand representing the case of double scatter. If we now introduce the  $(\Theta, x)$  notation in order to study the operator norm we can see that the only

difference between single and double scatter are some additional exponential functions and distances in the denominator that are strictly positive due to their definition, i.e. we are just summing up parts we already analyzed. The extension to multiple scatter is obvious. Hence the scatter operator in case of multiple scatter surely satisfies the conditions needed for the corresponding sobolev space estimate. Finally, we conclude that even in case of multiple scatter, PET can be interpreted as a perturbation of the X-ray transform.



## Chapter 4

# Numerical Results

In this chapter we will present some numerical experiments to demonstrate the impact of scatter. In section 4.1 we will confirm that PET can really be considered as a perturbation of the straight line model. In section 4.2 we will show that in some applications it is worthwhile to use the information contained in the scattered coincidences for the reconstruction.

### 4.1 PET in the case of weakly scattering media

As discussed in chapter 2 our scatter model does not include detector width so far because all classical results (i.e. sobolev space estimates and inversion formulas) are based on the assumption that lines of responses are given by  $g(\Theta, x)$ ,  $\Theta \in S^{n-1}$ ,  $x \in \Theta^\perp$ . In order to implement our new scatter model we have to account for the detector width, as in particular, the Klein-Nishina kernel denotes the probability that particles are scattered into a solid angle.

Let us consider a point  $z$  where scatter occurs and a detector  $D_j$  that measures the scattered photon. The solid angle  $\Omega_{z,D_j}$  needed for the scatter kernel can be approximated by

$$\Omega_{z,D_j} \approx \frac{D}{|z - d_j|^2},$$

where  $D$  is the area of the crystal face that is visible from the point  $z$ . The normal of  $D$  is given by  $(z - d_j)$ , where  $d_j$  is the center of  $D_j$ . Regarding our model from equation (2.29) we already have the corresponding denominator. Thus we only have to add  $D$ . Unfortunately this new interpretation of the denominator changes the space estimate derived in the previous chapter, since numerically we have to work with

$$\frac{D}{|d_i - d_j|^2} \int_{d_i}^{d_j} f ds,$$

instead of the classical X-ray transform

$$\int_{d_i}^{d_j} f ds = Pf.$$

Hence we cannot directly use the results of section 3.3 to check whether PET is a perturbation of the X-ray transform or not. Therefore we will compare reconstructions of simulated PET measurements in order to study the impact of scatter.

It is obvious that the amount of scatter depends on the density of the tissue as well as on the size of the object. Thus, although the density of a mouse is comparable to the density of a human body (on average  $\mu = 0.096\text{cm}^{-1}$ , which is the density of water), the magnitude of scatter is much higher in case of a human PET scan, since there is more tissue where scatter may occur. When assuming a constant attenuation coefficient for the object, the mean free path (MFP), i.e. the average distance a photon travels before it is scattered, is about  $1/\mu = 1/0.096 \approx 10$  cm. The size of a mouse suggests, prior to an exact analysis, that the amount of scattered events must be very small, if not negligible. Hence, PET should be nothing else but the simple line model, i.e. the X-ray transform or at least a perturbation of the X-ray transform, in some applications.

We will study simulations of small animal PET scans where the magnitude of scatter and attenuation is analyzed as a function of object size. Although we already know that the amount of scatter should be small for small objects, we want to understand how large the impact of scattered events is, when comparing reconstructions of scatter contaminated data with reconstructions using only true events.

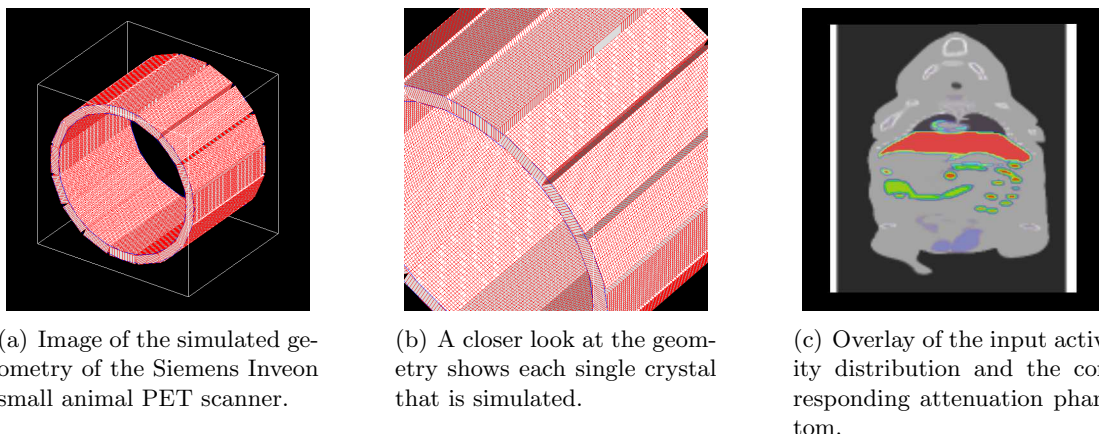


Figure 4.1: The Siemens Inveon PET scanner consisting of 80 rings with a total of 25600 crystals has been implemented in GATE to study the impact of scatter and attenuation respectively in small animal studies. As a realistic mouse model, the established MOBY phantom was used to create the activity distribution as well as the corresponding attenuation phantom.

Six different object sizes, i.e. sizes of the mouse ( $\approx 2.1\text{-}6.4$  cm diameters and  $3.5\text{-}8.7$  cm lengths), have been simulated using the GEANT4 [A<sup>+</sup>03] based GATE [JSS<sup>+</sup>04] simulation toolbox that provides the necessary framework to perform complete PET simulations starting from the beta<sup>+</sup> decay to the measuring process of the two photons. For this study the geometry of the Siemens Inveon preclinical small animal PET system [VDB<sup>+</sup>09, KHM<sup>+</sup>09] has been implemented (see figure 4.1). The mouse was modelled using the MOBY phantom [ST09] whereas the six different sizes are achieved by scaling the corresponding input image for the simulation. For each object size, simulations were performed, resulting in a set of sinograms containing  $\approx 20$  million events each. In order to analyze the degradation we performed four different reconstructions for each dataset

including:

- No correction
- Attenuation correction only
- Scatter correction only
- Attenuation and scatter correction

Hence we will discuss the impact of missing data (i.e. due to attenuation) as well as the impact of additional wrong information (i.e. due to scatter) as well as the combination of both distortions. Randoms coincidences have been neglected since they are not part of this investigation.

All reconstructions have been performed using a parallelized implementation of the well-known Expectation Maximization (EM) algorithm [SV82]. For attenuation correction the corresponding attenuation phantoms in combination with equation (1.11) were used. In those cases we assumed a perfect scatter correction and used only true events for reconstruction.

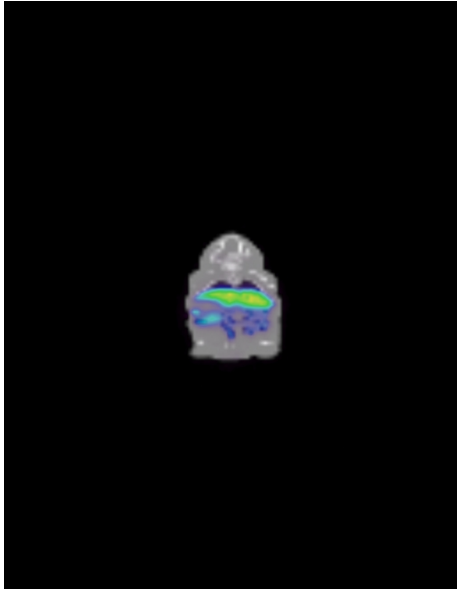
To assure convergence of the reconstruction algorithm a total of 20 iterations were applied to the data. The reconstruction for each dataset required about 1 minute per iteration on a 16 core Xeon machine, where the corresponding images had a size of  $128 \times 128 \times 159$ . Different reconstructions were made to study the impact of scatter by a visual comparison. For a detailed analysis of several regions of interests we refer to [Kon10].

Starting with the smallest phantom, we can hardly see any difference between the reconstructions with and without scatter correction. The images in the top row of figure 4.2 look identical to their corresponding scatter corrected versions. Although small details of the MOBY phantom are of a size close to the scanners resolution of the (about 1.3 mm) no details are lost due to scatter. We conclude that the impact of wrong information (scattered events) does not have big influence on the reconstruction results in case of small mice.

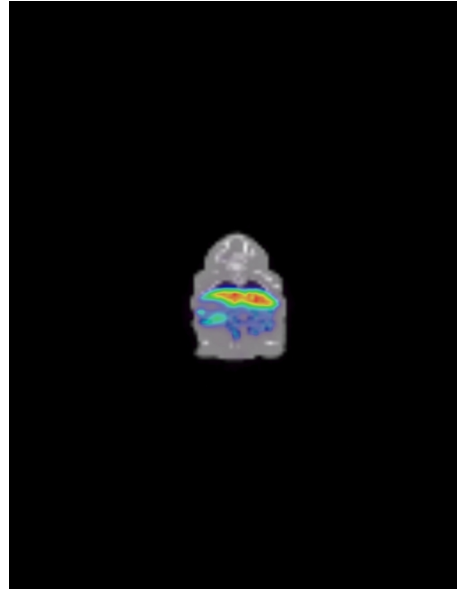
In contrast to this attenuation correction seems play a significant role even in this case. Comparing the two columns we clearly notice the increased activity level of the lungs after attenuation correction, i.e. the missing information has a huge impact on the reconstruction. Since this is the smallest mouse of this study we can at this point already assess that attenuation correction is needed for all PET reconstructions in order to obtain quantitative reconstructions.

As discussed in chapter 1, scatter and attenuation are more or less the same physical effect. Therefore one may wonder why scatter correction does not have the same impact on image quality as attenuation correction in this case. Let us consider a simple example to clarify the difference between both effects. If two photons on a certain line of response are attenuated, (i.e. scattered, since these effects are identical in PET) both are lost for measurements on the line. The probability that these two photons are scattered to the same line of response is nearly zero. Hence the information loss due to attenuation has a larger impact compared to the erroneous created information.

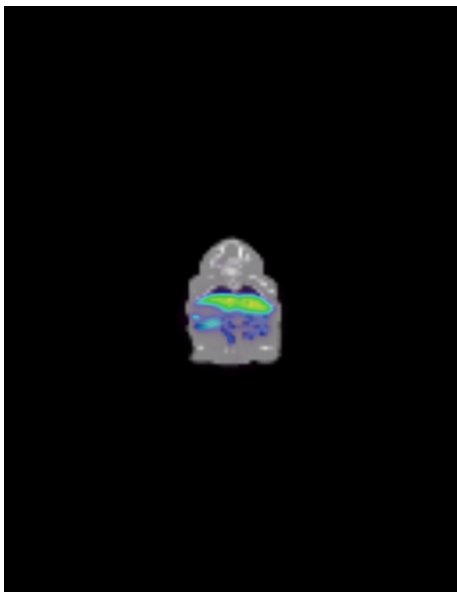
When increasing the objects size step by step we can see that the amount and hence the impact of scatter increases as well. In figure 4.5 the images in the bottom row show less noise outside the mouse in comparison to the images of the top row. We conclude that starting from this size of mice it is worthwhile to correct for scatter as well.



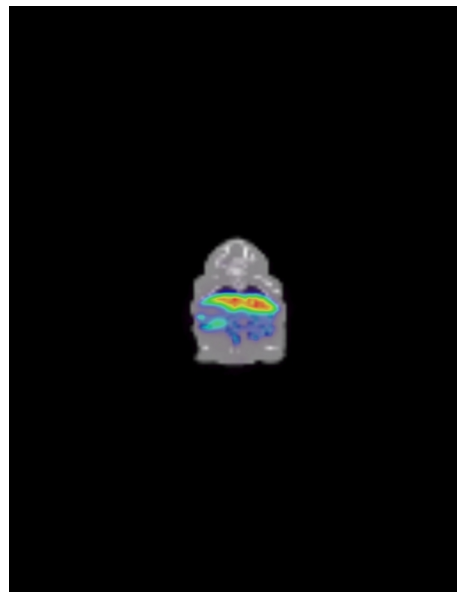
(a) Reconstruction without corrections



(b) Reconstruction with attenuation correction in sinogram space.

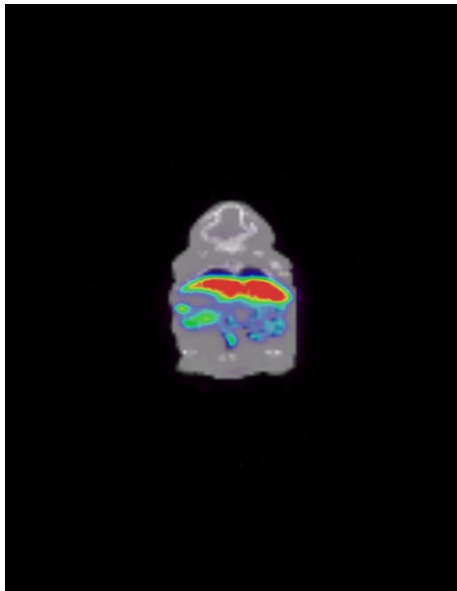


(c) Reconstruction with scatter correction in sinogram space.

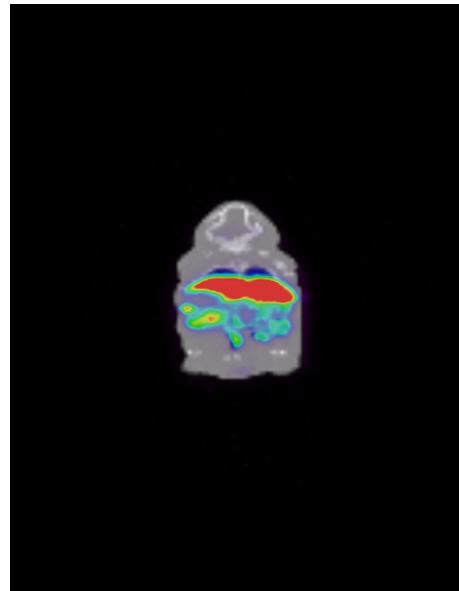


(d) Reconstruction with attenuation and scatter correction in sinogram space.

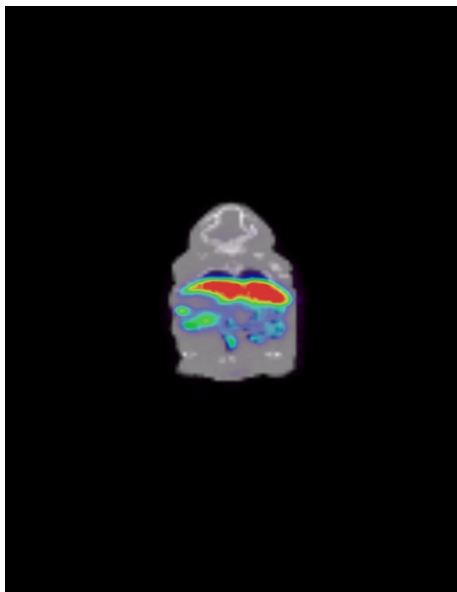
Figure 4.2: The smallest mouse phantom of this study has a diameter of 21mm and 35mm length. Due to these very small dimensions only 8% of the measured coincidences are scattered events. As we can see when comparing the top and bottom rows, scatter correction has almost no impact on the image quality. In contrast attenuation correction is obviously needed to achieve quantitative results.



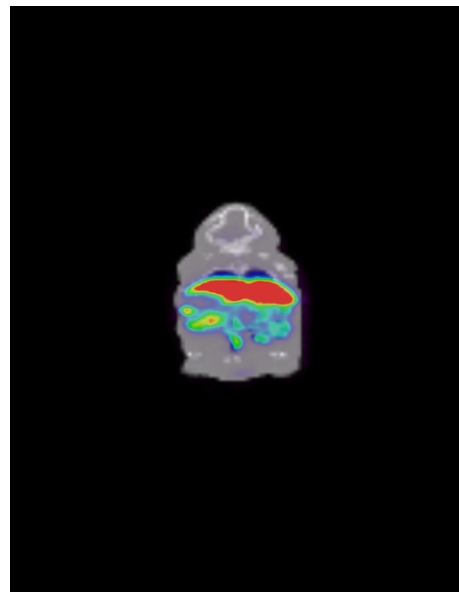
(a) Reconstruction without corrections



(b) Reconstruction with attenuation correction in sinogram space.

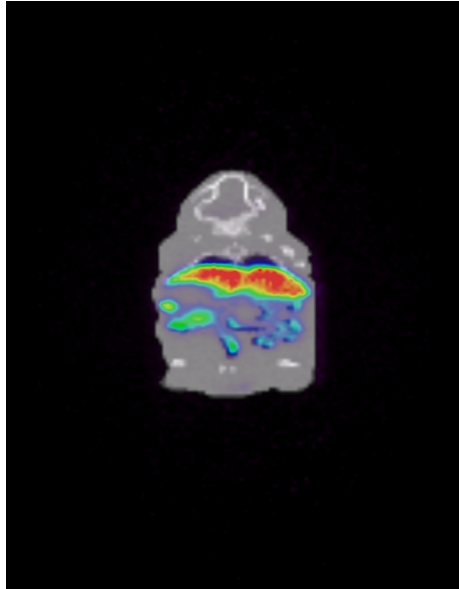


(c) Reconstruction with scatter correction in sinogram space.

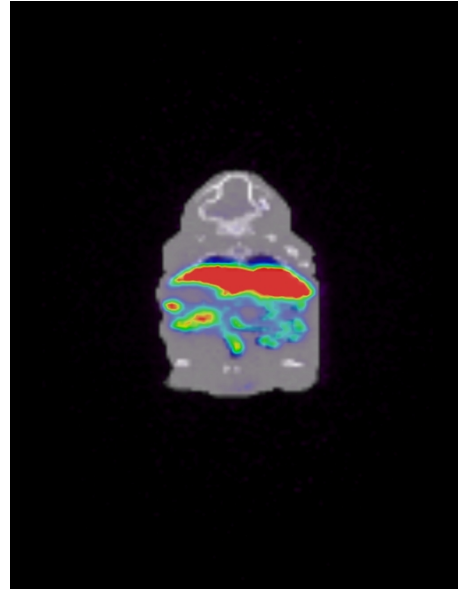


(d) Reconstruction with attenuation and scatter correction in sinogram space.

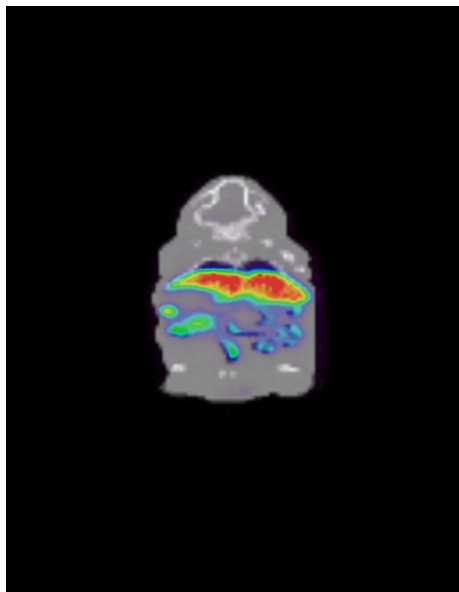
Figure 4.3: This mouse phantom has a diameter of 28mm and 40mm length leading to a scatter fraction of 11%. This impact of scatter and attenuation correction is comparable to the results of the smallest mouse phantom.



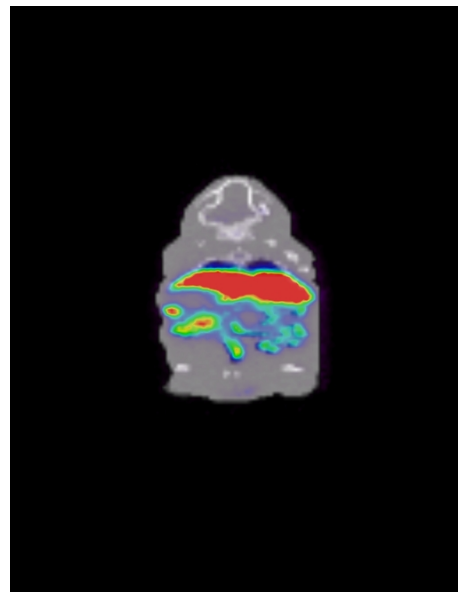
(a) Reconstruction without corrections



(b) Reconstruction with attenuation correction in sinogram space.

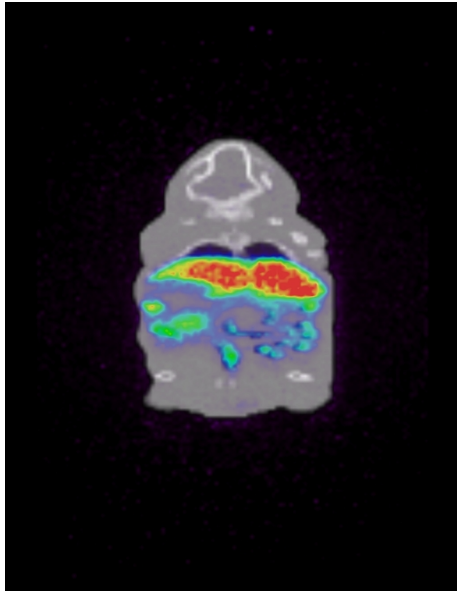


(c) Reconstruction with scatter correction in sinogram space.

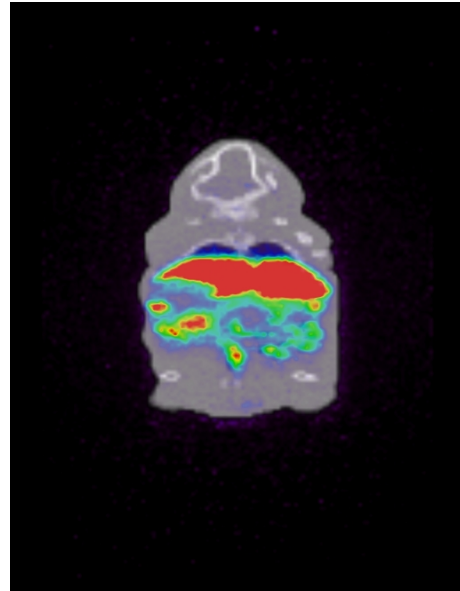


(d) Reconstruction with attenuation and scatter correction in sinogram space.

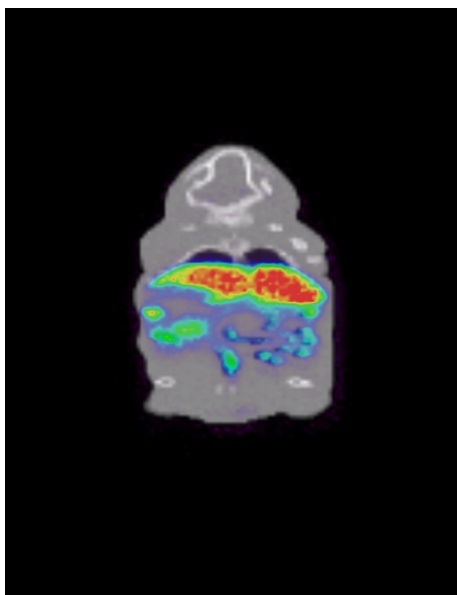
Figure 4.4: Although the scatter fraction reached 14% with this mouse phantom of 38mm diameter and 52mm length there is still no big improvement in image quality when using scatter correction. There is only a very small amount of noise in the images of the top row.



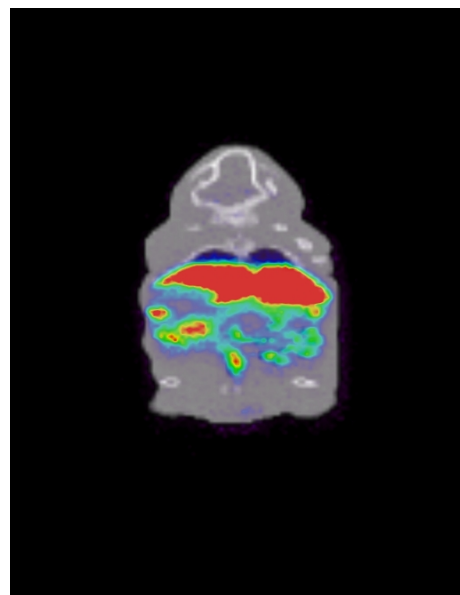
(a) Reconstruction without corrections



(b) Reconstruction with attenuation correction in sinogram space.

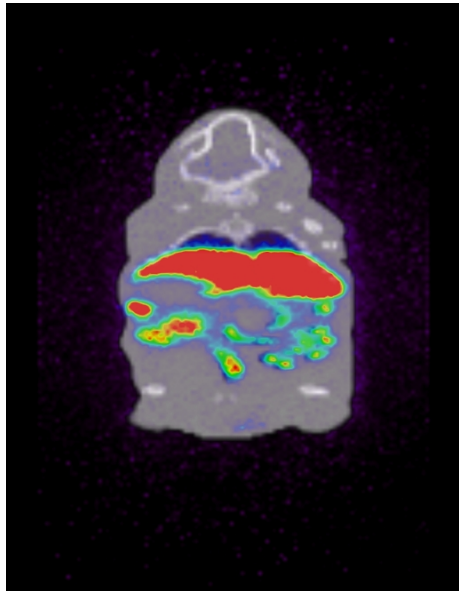


(c) Reconstruction with scatter correction in sinogram space.

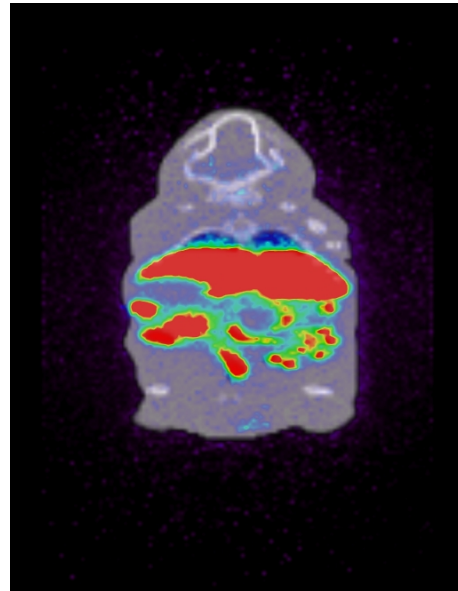


(d) Reconstruction with attenuation and scatter correction in sinogram space.

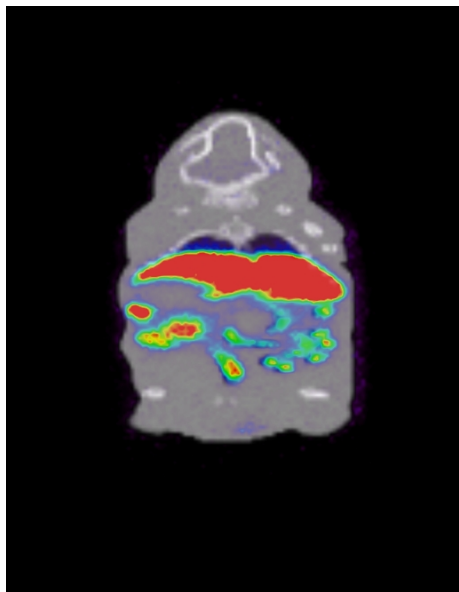
Figure 4.5: Finally, in this example with a scatter fraction of 17% we clearly see a difference between the two rows. In the top row there is some noise outside the mouse whereas in the bottom row this noise vanished due to scatter correction. The mouse phantom in this case has a diameter of 46mm and 63mm length. We conclude that scatter correction is necessary when examining mice of this size and larger.



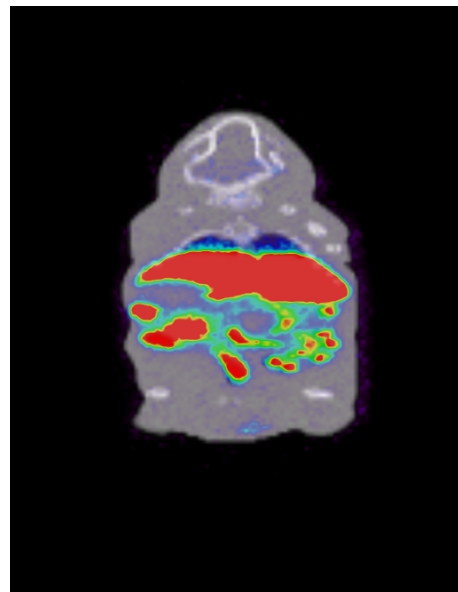
(a) Reconstruction without corrections



(b) Reconstruction with attenuation correction in sinogram space.

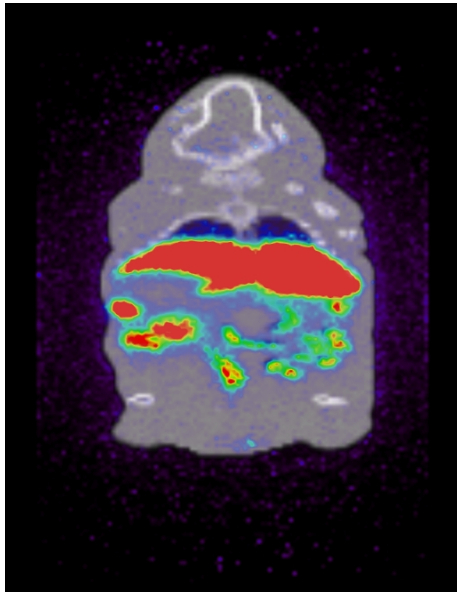


(c) Reconstruction with scatter correction in sinogram space.

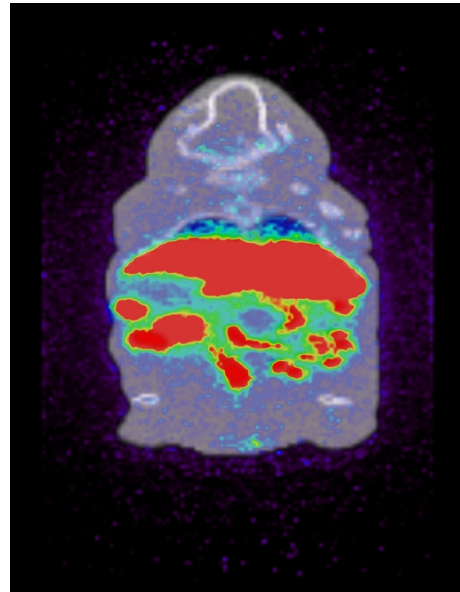


(d) Reconstruction with attenuation and scatter correction in sinogram space.

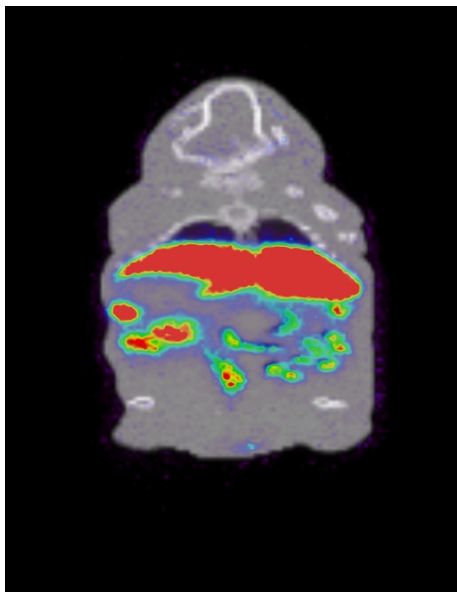
Figure 4.6: Compared to the mouse phantom from figure 4.5 we expect to have an even stronger impact of scatter for this phantom because of the diameter and length of 46mm and 63mm respectively. The scatter fraction is 20% in this case. The noise due to scatter outside the object can be seen clearly in the top row. After scatter correction this noise is almost completely gone.



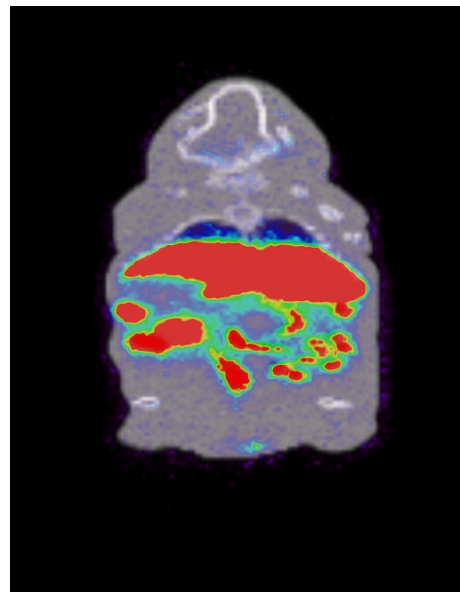
(a) Reconstruction without corrections



(b) Reconstruction with attenuation correction in sinogram space.



(c) Reconstruction with scatter correction in sinogram space.



(d) Reconstruction with attenuation and scatter correction in sinogram space.

Figure 4.7: The largest phantom of this study has a diameter of 62mm and 87mm length. Obviously both correction methods, attenuation and scatter correction, are needed to obtain quantitative results due to a scatter fraction of 23%. Even inside the mouse noise can be observed when neglecting scatter correction.

Our study shows that the X-ray transform is a good approximation to the exact PET model. In some cases, i.e. small objects, we do not even need scatter correction methods to achieve quantitative results. If the diameter and length of the object are smaller than 38mm and 52mm respectively scatter does not seem to have a serious impact on the image quality. At least in these cases PET can be seen as a perturbation of the X-ray transform. The more the size of the object increases the more image degradation due to scatter can be observed.

Apart from the impact of scatter correction attenuation correction turned out to have even more influence on the reconstruction results for all sizes of the object. Fortunately, attenuation correction is easy to perform - as long as we have a corresponding attenuation coefficient or at least a good approximation of  $\mu$ . In conclusion, the combination of scatter and attenuation correction leads us more and more to the aimed quantitative recon results.

## 4.2 Scatter Correction in PET using Projection Volumes

In chapter 1 we presented several scatter correction methods that were developed for PET. Although the single scatter simulation is the state of the art, the other methods are useful in some applications as well. The major drawback of all those methods is the degradation of data due to the subtraction of the scatter estimate.

We will show that it is useful in some applications to use the information still contained in the scattered events to improve the reconstruction. Therefore the reconstruction algorithm has to be modified in order to project over a volume instead of along a straight line. These projection volumes include information about the scatter distribution and thus have to be calculated separately for each dataset because different attenuation coefficients lead to different projection volumes.

For our study we restrict ourselves to the case of single scatter where the projection volumes are given by equation (2.31). As a proof of principle, we only performed 2D tests since the complexity of the approach leads to high computational costs.

### 4.2.1 Calculation of the projection volumes

During classical EM reconstruction, based on the simple line model, the system matrix is usually calculated on-the-fly since the corresponding algorithms are fast enough for this approach. In our case we have to solve (2.31) which includes the evaluation of the Boltzmann equation for several thousand times. Thus, we introduce a couple of preprocessing steps to speed up the calculation of the system matrix.

The geometry of the Siemens Biograph Sensation 16 [MBSZ06] has been implemented where we restrict ourselves to one of the 24 rings, but using all 384 detectors. A total of  $192 \times 192$  (i.e. number of parallel lines times number of different angles) projection volumes have to be calculated. The image size was chosen as  $175 \times 175$  where each pixel has an edge length of about 3.375 mm. These values are taken from the reference implementation of the scanner.

Since activity only appears inside the patients body, no voxel outside the patient can contribute to measurements. Hence we restricted the projection volumes to the domain of  $\mu$ . For all possible combinations of voxels and detectors the corresponding particle traces were calculated using the single scatter model from chapter 2.

Most of the line integrals of  $\mu$  are needed several times to evaluate the Boltzmann equation. Thus these values were precalculated in order to avoid redundant calculations. To evaluate the different line integrals we used the software components already written for the classic EM algorithm. A modified Siddon algorithm [Sid85] is used to calculate the intersections of lines and voxels. This step only takes a few minutes on a shared-memory system using 16 cores. With the help of this precalculated data all projection volumes were derived and stored. Depending on the energy-threshold  $E_{\min}$  (the smaller  $E_{\min}$ , the larger each single projection volume) these stored files required nearly 2 GB harddisk space. During the reconstruction the precalculated system matrix can be used leading to reasonable reconstruction times.

The calculation in two dimensions takes already about 40 minutes. Hence it is reasonable to work in 2D for this proof of principle. In order to apply this approach to real 3D data a new version of the current software that runs on a cluster must be written. In addition, the amount of data to be stored will increase significantly in case of 3D.

### 4.2.2 Simulation of phantom data

PET is a three-dimensional technique and obviously the underlying physics cannot be restricted to 2D. Hence our 2D study does not fully reflect the characteristics of a real PET scan, since photons do not only travel in a two-dimensional plane. Nevertheless we assume that 2D data is sufficient for a proof of principle.

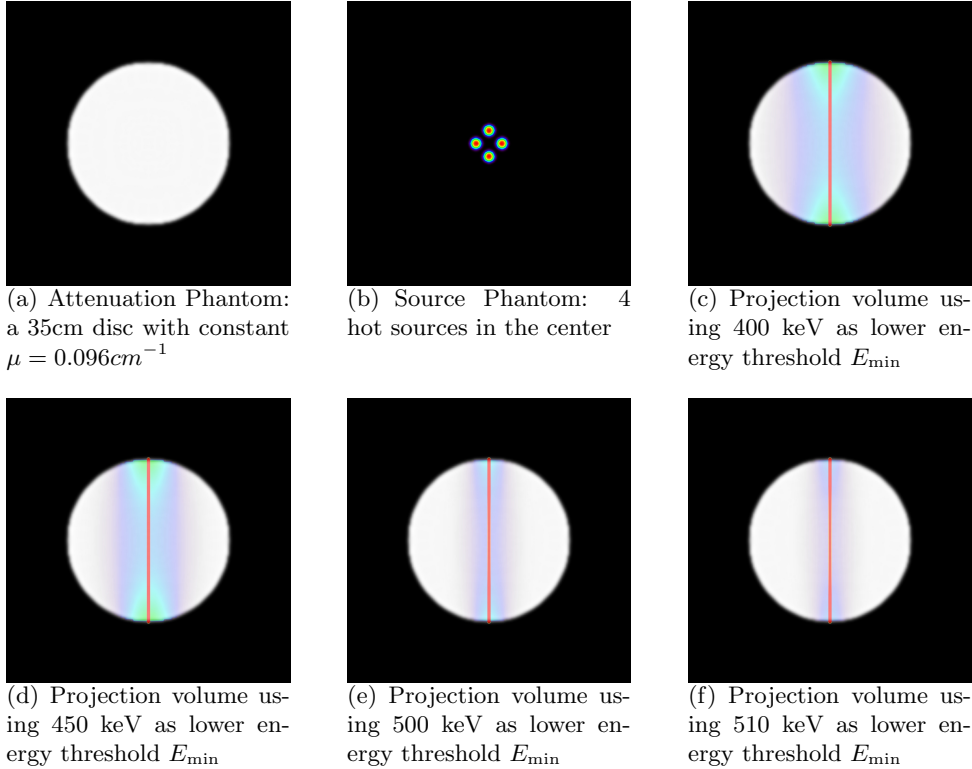
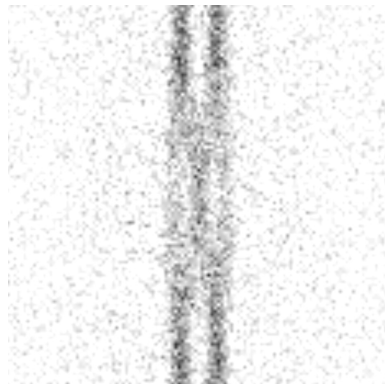


Figure 4.8: As already shown in chapter 2 and 3 we can modify the projection volumes with different choices of  $E_{\min}$ . In this study we are using a simple disc as attenuation phantom. The four sources in the center guarantee a high scatter fraction since all photons nearly have to traverse half of the disc.

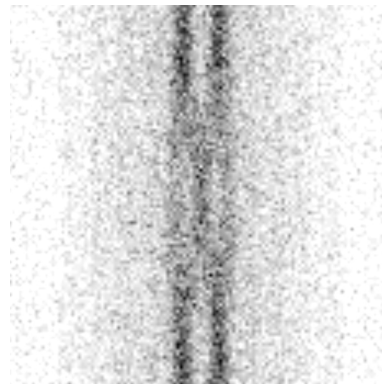
After calculating the corresponding projection volumes as discussed in the previous subsection with  $\mu$  given as in figure 4.8a), forward projections were performed in order to simulate effects up to single scatter. For a more realistic setting, Poisson noise was added. The scatter subtraction methods presented in chapter 1 work excellent in case of good statistics. In that case even after subtracting the scatter estimate, the statistics are sufficient to create a good image. Hence we focus on measurements with bad statistics and therefore with a high noise level. All calculations have been performed for several energy windows, i.e  $E_{\min} \in \{400, 450, 500, 510\}$ .

### 4.2.3 Comparison of both reconstruction techniques

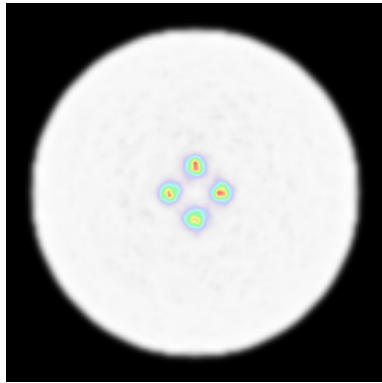
Before we take a look at the different reconstructions we like to consider what we have to expect. While increasing  $E_{\min}$ , the projection volume is more and more reduced to the X-ray transform. Hence, the advantage of having additional information due to scattered



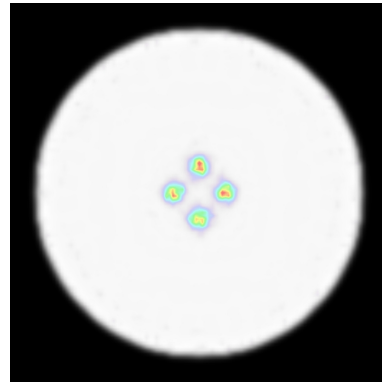
(a) Sinogram containing true events and noise



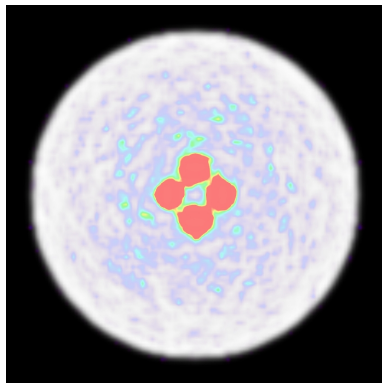
(b) Sinogram containing true events, scattered events and noise



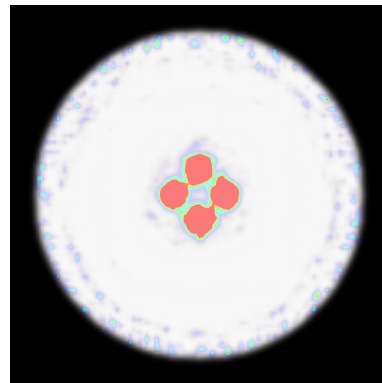
(c) EM reconstruction, 20 iterations



(d) EM reconstruction, 200 iterations



(e) EM reconstruction, 20 iterations

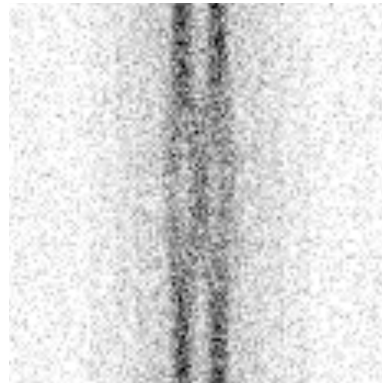


(f) EM reconstruction, 200 iterations

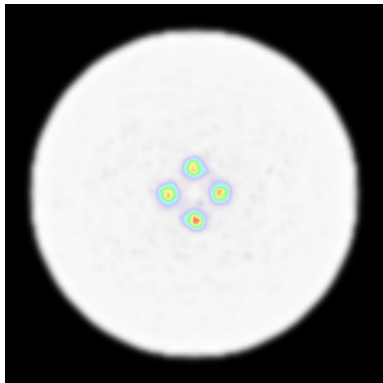
Figure 4.9: In case of  $E_{\min} = 400$  keV we can easily see the advantage of the new approach. Although the reconstructions looks similar in the middle row, a closer look at the background (bottom row) display the main difference. There is much more noise in the images on the left side. Nearly 45% of the photons are scattered in this example leading to a massive reduction in statistics. Hence, reconstruction using projection can be really effective in some applications.



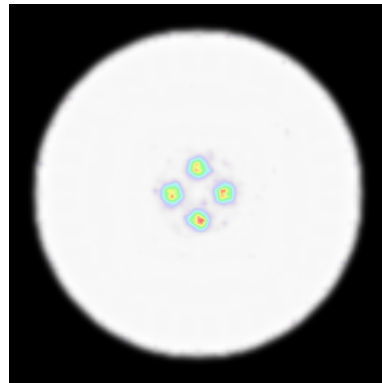
(a) Sinogram containing true events and noise



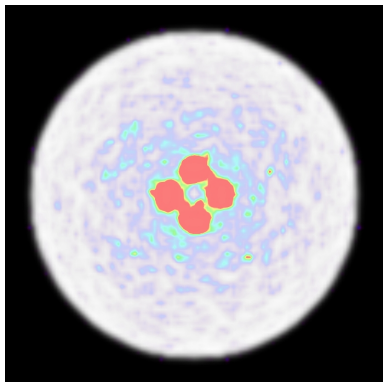
(b) Sinogram containing true events, scattered events and noise



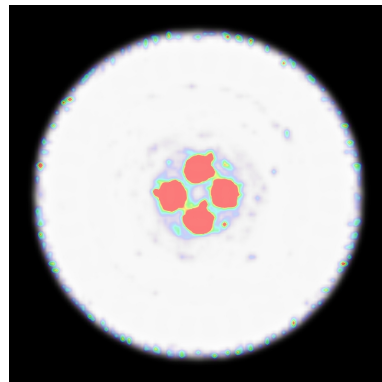
(c) EM reconstruction, 20 iterations



(d) EM reconstruction, 200 iterations

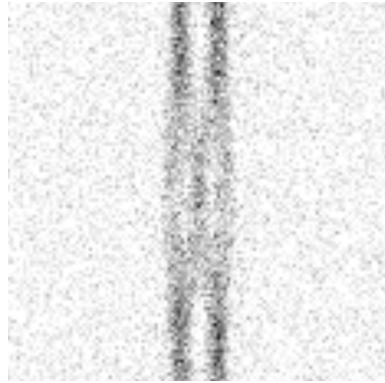


(e) EM reconstruction, 20 iterations

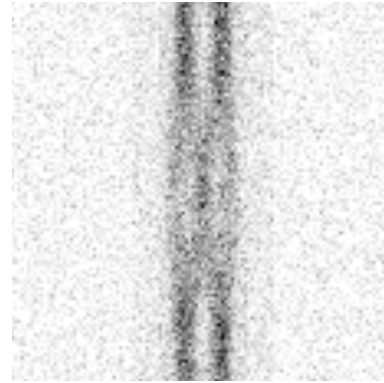


(f) EM reconstruction, 200 iterations

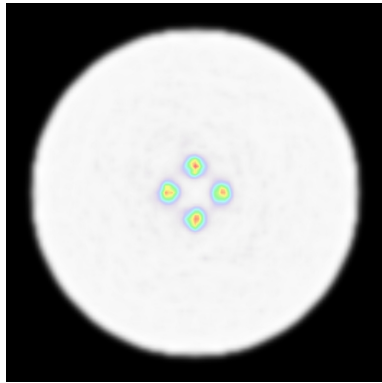
Figure 4.10: Regarding the two sinograms in case of  $E_{\min} = 450$  it is easy to see that there is lots of information left in the scattered events. The reconstruction using the new approach seems to look comparable to figure 4.9f). Using this higher energy threshold lowers the noise near the boundary of the ring whereas the noise between the four sources increases.



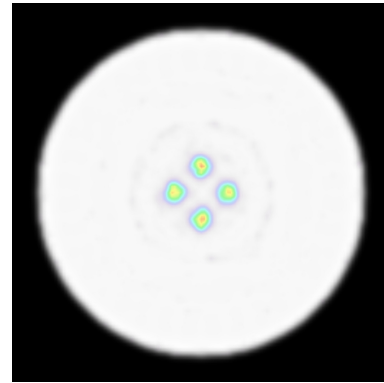
(a) Sinogram containing true events and noise



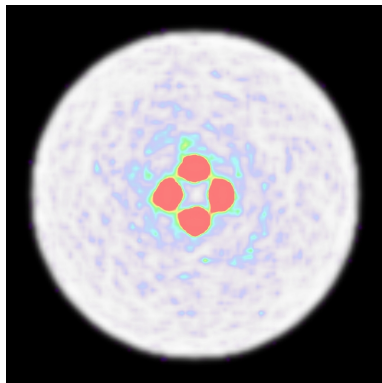
(b) Sinogram containing true events, scattered events and noise



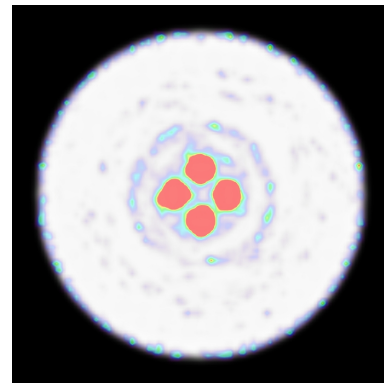
(c) EM reconstruction, 20 iterations



(d) EM reconstruction, 200 iterations

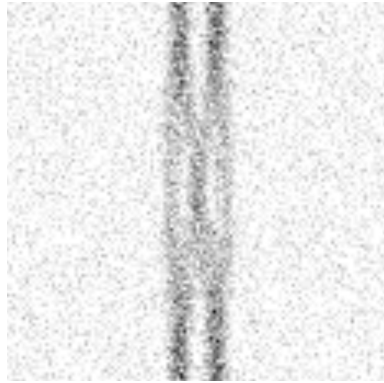


(e) EM reconstruction, 20 iterations

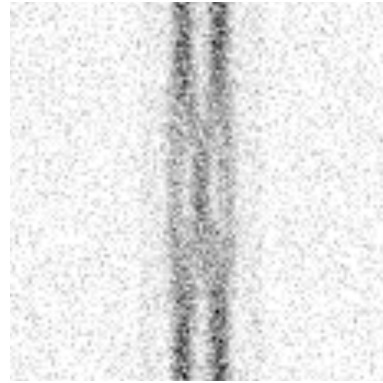


(f) EM reconstruction, 200 iterations

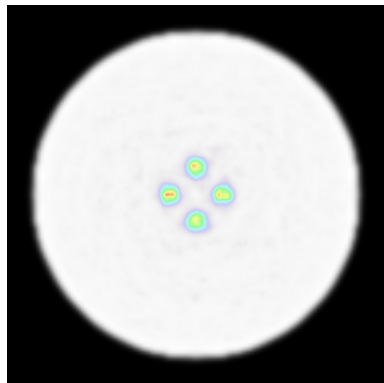
Figure 4.11: The observations of the last two examples can be proofed regarding the case of  $E_{\min} = 500$ . Since we are already close to the straight line model, the corresponding results of the bottom row are looking closer to each other than in the previous cases. Here we only have 20% of scattered events.



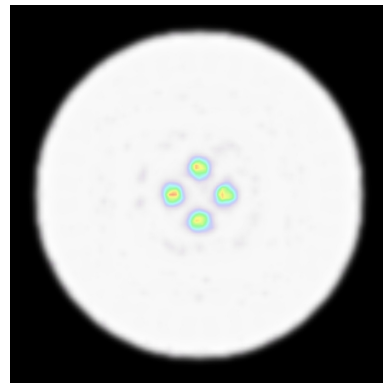
(a) Sinogram containing true events and noise



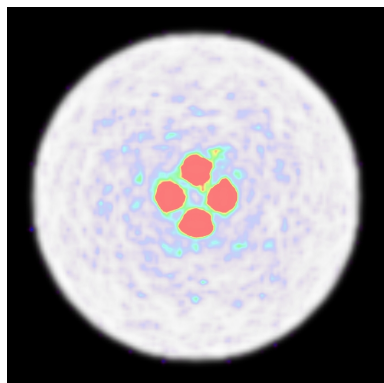
(b) Sinogram containing true events, scattered events and noise



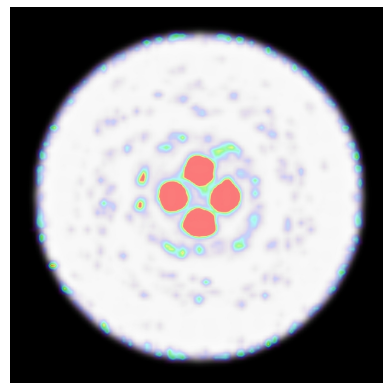
(c) EM reconstruction, 20 iterations



(d) EM reconstruction, 200 iterations



(e) EM reconstruction, 20 iterations



(f) EM reconstruction, 200 iterations

Figure 4.12: Regarding figure 4.8f) we can see that the projection volumes nearly degenerated to the X-ray transform. Hence the corresponding reconstructions look similar, i.e. a lot of noise can be observed around the four sources.

events is reduced step by step. Therefore we expect to have similar reconstruction results when comparing the straight line model with the new approach using  $E_{\min} = 510$  keV. We mention that next to the complex preprocessing steps, it also takes 10 times more iterations before the modified EM algorithm convergences.

A visual comparison of the different reconstructions shows the superiority of the new approach in case of  $E_{\min} = 400$  keV. In combination with bad statistics it seems to be worthwhile to perform complex reconstructions in order to recover as much information as possible. Scatter fractions of about 50% or more show how much information is lost when using the old correction methods. We choose  $E_{\min} = 400$  as the smallest threshold since this is used in daily routine. Since this threshold already covers scattering angles up to  $45^\circ$  we do not expect much better results with as smaller  $E_{\min}$ .

These results agree well with different publications dealing with the same topic like [VSB<sup>+</sup>06]. In this work the system matrix in a 2D setup was created using Monte Carlo simulations which is a very similar approach compared to our work. While we send particles into each directions once, the Monte Carlo approach randomly chooses the emitting angle of the photons. As in our case, a better contrast-noise performance was achieved. Additionally, this approach may compensate for degradation of resolution with radial distance. A more detailed analysis of our reconstructions is needed in order to look after this effect as well.

Similar publications for PET [RMD<sup>+</sup>03] and SPECT [BLB03, LBB<sup>+</sup>05] show the same benefits when using more information instead of the straight line model only. We conclude that our simple study already shows the opportunities that came along with this approach. Further studies in 3D and real patient data are needed to validate the results. This will be on focus in early future.



## Chapter 5

# Conclusion and Outlook

After introducing PET and its main degradation factors it became obvious that the simple X-ray transform is not the correct model for PET. The measured data has to be corrected for scattered events in order to be able to use the straight line model. This results in a loss of information. To overcome this problem, a new mathematical model was presented that includes scattered events in the reconstruction process as well. In addition to the derivation of the model it was shown that the unknown true activity can theoretically be fully recovered from scatter contaminated data. A perturbation approach allows the usage of the well known inversion formula for the X-ray transform, given a simple restriction on the attenuation coefficient. Thus, although the process of PET imaging is not exactly represented by the X-ray transform, PET can at least be seen as a perturbation of the X-ray transform in case of small objects. Further analytical studies of PET should include this new model as reference.

The perturbation result was also proven numerically. A software mouse phantom was used to simulate PET measurements of small objects. The phantom size was increased step by step to investigate the impact of scatter with reference to the object size. It turned out that up to a certain object size, PET can be identified with the X-ray transform.

Additionally, it was shown that information contained in scattered coincidences can still make a contribution to the quality of the reconstruction result. Therefore, the classic EM reconstruction was modified in order to project along volumes instead of lines. A simple software phantom study shows the superiority of this approach in case of bad statistics.

Future research in this field can be divided into two parts. Firstly, the theoretical model may be extended by time dependency which leads to time-of-flight PET. Obviously, this would increase the complexity again while the estimates of section 3 should also be applicable in that case. Secondly, the new reconstruction technique has to be extend to 3D data and applied to real patient data. This requires more computational power by means of a cluster implementation or an implementation on GPUs.



# Bibliography

- [A<sup>+</sup>03] S. Agostinelli et al. GEANT4: A simulation toolkit. *Nucl. Instrum. Meth.*, A506:250–303, 2003.
- [AAWK04] Roberto Accorsi, Lars-Eric Adam, Matthew E Werner, and Joel S Karp. Optimization of a fully 3d single scatter simulation algorithm for 3d pet. *Phys. Med. Biol.*, 49:2577–2598, 2004.
- [Alt85] Hans Wilhelm Alt. *Lineare Funktionalanalysis*. Springer, 1985.
- [BBF<sup>+</sup>00] R Buchert, KH Bohuslavizki, H Fricke, J Mester, and M Clausen. Performance evaluation of pet scanners: testing of geometric arc correction by off-centre uniformity measurement. *Eur J Nucle Med*, 27(1):83–90, 2000.
- [BGCC99] H H Barrett, B Gallas, E Clarkson, and A Clough. *Scattered radiation in nuclear medicine: A case study of the Boltzman transport equation*, volume 110 of *IMA Vol. Math. Appl.*, pages 71–100. Springer, New York, 1999.
- [BKL<sup>+</sup>05] David Brasse, Paul E. Kinahan, Carole Lartizien, Claude Comtat, Mike Casey, and Christian Michel. Correction methods for random coincidences in fully 3d whole-body pet: Impact on data and image quality. *Journal of Nuclear Medicine*, 46(5):859–867, 2005.
- [BLB03] I. Buvat, D. Lazaro, and V. Breton. Fully 3d monte carlo reconstruction in spect: proof of concept and is that worthwhile?'. *Conf. Proc. of the VIIIth International Meeting on Fully Three-dimensional Image Reconstruction in Radiology and Nuclear Medicine, 29 June-4 July 2003, Saint-Malo, France*, 2003.
- [BM94] Dale L Bailey and Steven R Meikle. A convolution-subtraction scatter correction method for 3d pet. *Physics in Medicine and Biology*, 39:411–424, 1994.
- [Bon98] Anatoly N. Bondarenko. The structure of the fundamental solution of the time-independent transport equation. *Journal of Mathematical Analysis and Applications*, 221, 1998.
- [BT08] Guillaume Bal and Alexandru Tamasan. Inverse source problems in transport equations. *SIAM Journal on Mathematical Analysis*, 39:57–76, 2008.
- [Cas08] Michael E. Casey. Improving pet with hd•pet + time of flight. Technical report, SIEMENS, 2008.

- [CH95] SR Cherry and SC Huang. Effects of scatter on model parameter estimates in 3d pet studies of the human brain. *IEEE Trans Nucl Sci*, 42:1174–1179, 1995.
- [CMH93] S Cherry, S Meikle, and E J Hoffman. Correction and characterization of scattered events in three-dimensional pet using scanners with retractable septa. *Journal of Nuclear Medicine*, 34:671–678, 1993.
- [DCT95] M Defrise, R Clack, and D W Townsend. Image reconstruction from truncated, two-dimensional, parallel projections. *Inverse Problems*, 11:287–313, 1995.
- [DL93] Robert Dautray and Jacques-Louis Lions. *Mathematical Analysis and Numerical Methods for Science and Technology*, volume 6 of *Evolution Problems II*. Springer-Verlag, 1993.
- [ETC<sup>+</sup>02] Kamel E, Hany TF, Burger C, Treyer V, Lonn AH, von Schulthess GK, and Buck A. Ct vs 68ge attenuation correction in a combined pet/ct system: evaluation of the effect of lowering the ct tube current. *Eur J Nucl Med Mol Imaging*, 29:346–350, 2002.
- [FT93] E. C. Frey and B. M. W. Tsui. A practical method for incorporating scatter in a projector-backprojector for accurate scatter compensation in spect. *IEEE Transactions on Nuclear Science*, 40(4):1107–1116, August 1993.
- [Geb09] Sebastian Gebennus. *Zur Modellierung und statistischen Auswertung von PET-Daten*. PhD thesis, University of Münster, 2009.
- [GN02] Daniel Gourion and Dominikus Noll. The inverse problem of emission tomography. *Inverse Problems*, 18:1435–1460, 2002.
- [GSS<sup>+</sup>96] S Grootenkyz, T J Spinksy, D Sashinx, N M Spyrouk, and T Jones. Correction for scatter in 3d brain pet using a dual energy window method. *Phys. Med. Biol.*, 41:2757–2774, 1996.
- [HL94] H. Malcolm Hudson and Richard S. Larkin. Accelerated image reconstruction using ordered subsets of projection data. *IEEE Transactions on Medical Imaging*, 1994.
- [JJGC85] Carey E. Floyd Jr., Ronald J. Jaszczak, Kim L. Greer, and R. Edward Coleman. Deconvolution of compton scatter in spect. *Journal of Nuclear Medicine*, 26:403–408, 1985.
- [JSS<sup>+</sup>04] S Jan, G Santin, D Strul, S Staelens, K Assié, D Autret, S Avner, R Barbier, M Bardiès, P M Bloomfield, D Brasse, V Breton, P Bruyndonckx, I Buvat, A F Chatzioannou, Y Choi, Y H Chung, C Comtat, D Donnarieix, L Ferrer, S J Glick, C J Groiselle, D Guez, P-F Honore, S Kerhoas-Cavata, A S Kirov, V Kohli, M Koole, M Krieguer, D J van der Laan, F Lamare, G Langeron, C Lartizien, D Lazaro, M C Maas, L Maigne, F Mayet, F Melot, C Merheb, E Pennacchio, J Perez, U Pietrzyk, F R Rannou, M Rey, D R Schaart, C R Schmidlein, L Simon, T Y Song, J-M Vieira, D Visvikis, R Van de Walle,

- E Wieërs, and C Morel. Gate: a simulation toolkit for pet and spect. *Phys. Med. Biol.*, 49:4543–4561, 2004.
- [Kat02] Alexander Katsevich. Theoretically exact fbp-type inversion algorithm for spiral ct. *SIAM Journal on Applied Mathematics*, 62:2012–2026, 2002.
- [Kat04] Alexander Katsevich. Image reconstruction for the circle and line trajectory. *Phys. Med. Biol.*, 49:5059–5072, 2004.
- [KHM<sup>+</sup>09] Brad J Kemp, Carrie B Hruska, Aaron R McFarland, Mark W Lenox, and Val J Lowe. Nema nu 2-2007 performance measurements of the siemens inveon<sup>TM</sup> preclinical small animal pet system. *Phys. Med. Biol.*, 54:2359–2376, 2009.
- [Kon10] Arda Konik. PhD thesis, Department of Physics and Astronomy, University of Iowa, 2010.
- [Kun01] Leonid A Kunyansky. A new spect reconstruction algorithm based on the novikov explicit inversion formula. *Inverse Problems*, 17:293–306, 2001.
- [Kö06] Thomas Kösters. Konvergenz iterativer verfahren in der emissionstomographie. Master’s thesis, University of Münster, 2006.
- [LBB<sup>+</sup>05] D Lazaro, Z El Bitar, V Breton, D Hill, and I Buvat. Fully 3d monte carlo reconstruction in spect: a feasibility study. *Phys. Med. Biol.*, 50:3739–3754, 2005.
- [LH99] C S Levin and E J Hoffman. Calculation of positron range and its effect on the fundamental limit of positron emission tomography system spatial resolution. *Phys. Med. Biol.*, 44:781–799, 1999.
- [LK04] Thomas Lewellen and Joel Karp. *PET Systems*, chapter 10, pages 179–194. Elsevier, 2004.
- [Mai00] B A Mair. A mathematical model incorporating the effects of detector width in 2d pet. *Inverse Problems*, 16:223–246, 2000.
- [MBSZ06] M.-J. Martínez, Y. Bercier, M. Schwaiger, and S. I. Ziegler. Pet/ct biograph tm sensation 16 - performance improvement using faster electronics. *Nuklearmedizin*, 45(3):126–133, 2006.
- [MDDH86] D J Macey, G L DeNardo, S J DeNardo, and H H Hines. Comparison of low- and medium-energy collimators for spect imaging with iodine-123-labeled antibodies. *Journal of Nuclear Medicine*, 27:1467–1474, 1986.
- [MMH<sup>+</sup>04] John Missimer, Zoltan Madi, Michael Honer, Claudia Keller, August Schubiger, and Simon-Mensah Ametamey. Performance evaluation of the 16-module quad-hidac small animal pet camera. *Phys. Med. Biol.*, 49:2069–2081, 2004.
- [MRH85] B M Mazoyer, M S Roos, and R H Huesman. Dead time correction and counting statistics for positron tomography. *Phys. Med. Biol.*, 30(5):385–399, 1985.

- 
- [MTJ<sup>+</sup>07] P J Markiewicz, M Tamal, P J Julyan, D L Hastings, and A J Reader. High accuracy multiple scatter modelling for 3d whole body pet. *Physics in Medicine and Biology*, 52:829–847, 2007.
- [Nat86] Frank Natterer. *The Mathematics of Computerized Tomography*. B.G. Teubner, 1986.
- [Nat00] Frank Natterer. Inversion of the attenuated radon transform. Technical report, Institut für Numerische und instrumentelle Mathematik, 2000.
- [Nat03] Frank Natterer. Inverse probleme, 2003.
- [Nov00] R G Novikov. An inversion formula for the attenuated x-ray transform. Technical report, Departement de Mathematique, Universite de Nantes, 2000.
- [Nov02] Roman G Novikov. An inversion formula for the attenuated x-ray transformation. *Ark. Math.*, 40:145–167, 2002.
- [NW01] Frank Natterer and Frank Wübbeling. *Mathematical Methods in Image Reconstruction*. SIAM, 2001.
- [NW04] Frank Natterer and Frank Wübbeling. Scatter correction in pet based on transport models. Technical report, Institut für Numerische und instrumentelle Mathematik, 2004.
- [Orl76] S. S. Orlov. Theory of three dimensional reconstruction ii: The recovery operator. *Soviet Phys. Crystallogr.*, 20:429–433, 1976.
- [Phe04] M E Phelps. *PET: Molecular Imaging and its Biological Applications*. Springer, 2004.
- [PSV09] X Pan, E Y Sidky, and M Vannier. Why do commercial ct scanners still employ traditional, filtered back-projection for image reconstruction? *Inverse Problems*, 25, 2009.
- [RA07] Niklas Rehfeld and Markus Alber. A parallelizable compression scheme for monte carlo scatter system matrices in pet image reconstruction. *Phys. Med. Biol.*, 52:3421–3437, 2007.
- [Rad17] J Radon. Über die bestimmung von funktionen durch ihre integralwerte längs gewisser mannigfaltigkeiten. *Berichte Sächsische Akademie der Wissenschaften, Leipzig, Mathematisch-Physikalische Klasse*, 69:262–277, 1917.
- [RMD<sup>+</sup>03] M Rafecas, B Mosler, M Dietz, M Pogl, A Stamatakis, D.P. McElroy, and S.I. Ziegler. Use of a monte carlo-based probability matrix for 3-d iterative reconstruction of madpet-ii data. *IEEE Transactions on Nuclear Science*, 51:2597–2605, 2003.
- [SFK94] Lingxiong Shao, R. Freifelder, and J.S. Karp. Triple energy window scatter correction technique in pet. *IEEE Trans. Med. Imaging*, 13:641–648, 1994.

- 
- [Sid85] RL Siddon. Fast calculation of the exact radiological path for a three-dimensional ct array. *Medical Physics*, 12(2):252–255, 1985.
- [SMB<sup>+</sup>98] T J Spinks, M P Miller, D L Bailey, P M Bloomfield, L Livieratos, and T Jones. The effect of activity outside the direct field of view in a 3d-only whole-body positron tomograph. *Phys. Med. Biol.*, 43:895–904, 1998.
- [Sol76] Donald C. Solmon. The x-ray transform. *Journal of Mathematical Analysis and Applications*, 56:61–83, 1976.
- [SP87] J A Sorensen and M E Phelps. *Physics in Nuclear Medicine*. Grune & Stratton Inc, 1987.
- [ST09] W.P. Segars and B.M.W. Tsui. *Handbook of Anatomical Models for Radiation Dosimetry*, chapter The MCAT, NCAT, XCAT, and MOBY Computational Human and Mouse Phantoms. Informa Healthcare, 1st edition, 2009.
- [SU08] Plamen Stefanov and Gunther Uhlmann. An inverse source problem in optical molecular imaging. *Analysis & PDE*, 1:115–126, 2008.
- [SV82] L A Shepp and Y Vardi. Maximum likelihood reconstruction for emission tomography. *IEEE Trans. Med. Imaging*, 1:113–122, 1982.
- [VDB<sup>+</sup>09] Eric P Visser, Jonathan A Disselhorst, Maarten Brom, Peter Laverman, Martin Gotthardt, Wim J G Oyen, and Otto C Boerman. Spatial resolution and sensitivity of the inveon small-animal pet scanner. *Journal of Nuclear Medicine*, 50(1):139–147, 2009.
- [vdHVR<sup>+</sup>09] F van der Have, B Vastenhouw, RM Ramakers, W Branderhorst, JO Krah, C Ji, SG Staelens, and FJ Beekman. U-spect-ii: An ultra-high-resolution device for molecular small-animal imaging. *J Nucl Med*, 50:599–605, 2009.
- [VSB<sup>+</sup>06] Stefaan Vandenberghe, Steven Staelens, Charles L Byrne, Edward J Soares, Ignace Lemahieu, and Stephen J Glick. Reconstruction of 2d pet data with monte carlo generated system matrix for generalized natural pixels. *Phys. Med. Biol.*, 51:3105–3125, 2006.
- [VSK85] Y. Vardi, L. A. Shepp, and L. Kaufman. A statistical model for positron emission tomography. *Journal of the American Statistical Association*, 80:8–20, 1985.
- [WA04] Miles N. Wernick and John N. Aarsvold. *Emission Tomography*. Elsevier, 2004.
- [Wat00] C. C. Watson. New, faster, image-based scatter correction for 3d pet. *IEEE Transactions on Nuclear Science*, 47(4):1587–1594, August 2000.
- [Wat07] C. C. Watson. Extension of single scatter simulation to scatter correction of time-of-flight pet. *IEEE Transactions on Nuclear Science*, 54(5):1679–1686, 2007.

- [Wat09] Charles C. Watson. A hybrid algorithm for randoms variance reduction. In *Proc. IEEE Nuclear Science Symposium and Medical Imaging Conference*, 2009.
- [WBD<sup>+</sup>02] Alexander Werling, Olaf Bublitz, Josef Doll, Lars-Eric Adam, and Gunnar Brix. Fast implementation of the single scatter simulation algorithm and its use in iterative image reconstruction of pet data. *Physics in Medicine and Biology*, 47:2947–2960, 2002.
- [WCNG97] A Welch, R Clack, F Natterer, and GT Gullberg. Toward accurate attenuation correction in spect without transmission measurements. *IEEE Trans. Med. Imaging*, 16(5):532–541, 1997.
- [Wer01] Andreas Werling. *Modellbasierte Korrektur der Streustrahlung in der Positronen-Emissions-Tomographie*. PhD thesis, Ruprecht-Karls-Universität, 2001.
- [Wü06] Frank Wübbeling. Quick derivation of the transport equation. Technical report, Institut für Numerische und instrumentelle Mathematik, 2006.
- [Zai00] Habib Zaidi. Comparative evaluation of scatter correction techniques in 3d positron emission tomography. *Eur J Nucle Med*, 27:1813–1826, 2000.





